2013

Propagation of nonlinear optical beams in finite liquid crystal cells

Luke W. Sciberras
University of Wollongong

Recommended Citation

Sciberras, Luke W., Propagation of nonlinear optical beams in finite liquid crystal cells, Doctor of Philosophy thesis, School of Mathematics and Applied Statistics, University of Wollongong, 2013. http://ro.uow.edu.au/theses/3902

Propagation of nonlinear optical beams in finite liquid crystal cells

School of Mathematics and Applied Statistics

Ph.D Thesis

Luke W. Sciberras

2013

Declaration

This thesis is an account of research undertaken between February 2010 and May 2013 at The School of Mathematics and Applied Statics, University of Wollongong, Australia.

Except where acknowledged in the customary manner, the material presented in this thesis is, to the best of my knowledge, original.

Luke W. Sciberras

May, 2013.

Abstract

A nonlinear medium that displays promise in all-optical communications is a nematic liquid crystal. A nematic liquid crystal exhibits a “huge” nonlinearity, so that nonlinear effects can be observed over millimetre distances for relative low powered input beams (milliwatt power). Spatial optical solitons, termed nematicons, are supported in nematic liquid crystals. A further property of nematic liquid crystals is that there optical response is nonlocal, in that the elastic response of the nematic extends beyond the optical perturbing beam. This nonlocal response allows two dimensional beams, such as nematicons and optical vortices, to be stable.

The equations governing nonlinear optical beam propagation in nematic liquid crystals form a non-integrable, coupled system of an nonlinear Schrödinger-type equation for the beam and a Poisson’s equation for the medium response. This system has no known, general solutions. In this thesis, an approximate variational technique, termed modulation theory, and numerical solutions will be used to analyse the evolution and propagation of ne-

maticons, both circular and elliptical in cross section, and optical vortices in a finite liquid crystal cell. Particular attention is paid to the effect of boundaries on the beam trajectory and stability. Modulation theory has the advantage that the coupled partial differential equations governing the beam are reduced to a finite dimensional dynamical system, which yields insights into the underlying physical mechanisms. In addition, modulation theory can be easily extended to account for the effect of the diffractive radiation shed as a beam evolves.

Two methods are used to solve the equation for the medium response, Fourier series and the method of images, with the latter found to give a much more efficient solution. It is found that the cell boundaries act as a repulsive force on a beam, so that a beam has a spiral path down a cell. It is also found that interaction with cell walls can destabilise an optical vortex. A linearised stability analysis is used to determine the minimum distance of approach to a cell boundary before instability sets in. This minimum distance is found to be in excellent agreement with numerical solutions. Finally, the propagation of an elliptic nematicon with orbital angular momentum in a finite-sized cell is analysed. It is found that the inclusion of angular momentum loss to radiation is vital for the accurate description of this beam. This loss is included for the first time.

To my parents

Acknowledgments

I would like to sincerely thank Professor Noel Smyth for his continued support and guidance throughout this quest. Noel's interest in sharing his wealth of knowledge, as well as his bottomless passion for the subject matter has been an inspiration. I have learnt a great deal and hope Noel's enthusiasm has become a part of me, in that I can offer the same experience to others. I am very grateful indeed! To Associate Professor Annette Worthy your encouragement has led me to overcome many obstacles, which have taken me out of my comfort zone. For your friendship I am most thankful. To Professor Tim Marchant you have always managed to be there, responding quickly to offer a helping hand and provide support no matter what the issue. Without your generosity I would not be at this point. To Professor Tim Minzoni you have shed light on new and fascinating areas of mathematics, offering patient explanations on numerous techniques and methods to help along the way. To Noel, Annette, Tim and Tim, I thank you all for making this adventure pleasant and achievable.

To my parents Judy and Tony Sciberras, thank you for the love and care you have provided, not only in the tough times, but also when things were going well. You both have some how managed to be there, always. Your continual support has been overwhelming, and is much appreciated. To my sister Alicia, thanks for offering numerous distractions along the way, helping me forget about the tasks at hand and letting off some steam. Most importantly, you are a constant inspiration and someone I will always seek.

Finally, to all those whom I have met along the way, each and everyone of you has helped and for this I am thankful.

Contents

List of Abbreviations

KdV – Korteweg de Vies equation

NLS – Nonlinear Schrödinger equation

NLC – Nematic liquid crystal

PDE – Partial differential equation

ODE – Ordinary differential equation

RK4 – Fourth-order Runge–Kutta

IVP – Initial value problem

BVP – Boundary value problem

MoI – Method of images

Chapter 1

Introduction

1.1 Solitary waves and the soliton: A brief history

Historically, the voyage of the soliton began with an observation of a novel nonlinear phenomenon by John Scott Russell in 1834 [1], which he called the "Wave of Translation," later to be known as a solitary wave in recognition of its single pulse structure [2]. Scott Russell's observation of an isolated water wave propagating with a constant velocity and amplitude over a large distance created great excitement in the scientific community. As an isolated wave was contrary to accepted water wave theory of the time, which consisted of periodic waves, this new type of was was naturally dismissed. Prominent scientists and mathematicians were eventually drawn by personal interest to this new found field. In 1876 Lord Rayleigh, for instance, was one of the first scientists to express a solitary wave in shallow water using a mathematical description, describing the profile in terms of the square of a hyperbolic secant [3]. Keeping in mind the aim of arriving at a governing equation that supports solitary wave solutions, let us digress to water waves in the ocean. Water waves form, peak and then break, with the underlying evolutionary factor being nonlinear. In fact, what is occurring is that the crest of the propagating wave is travelling faster than the remainder of the wave, resulting in an instability. The wave can no longer maintain its profile, and the wave breaks. Nonlinearity is then important for the description of water waves. The mathematicians Korteweg and de Vries [4] went beyond the usual linear water wave theory and use a weakly nonlinear long wave expansion to derive an equation supporting solitary wave solutions. The resulting Korteweg de Vries (KdV) equation governs the evolution of nonlinear long water waves, similar to those observed by Scott Russell. The key ingredient of the KdV equation is its balance between the effects of dispersion and nonlinearity.

After a long dormant period, interest in the KdV equation was revived by the numerical work of Fermi, Pasta and Ulam [5]. Using the first computers at Los Alamos they numerically studied the behaviour of a long chain of masses joined by nonlinear springs. They expected to see the system go to thermal equilibrium with all modes excited almost equally. However, they found that the system exhibited quasi-periodic behaviour with only a few modes excited. Zabusky and Kruskal [2] extended this numerical study by taking the continuous limit of the Fermi, Pasta, Ulam chain, which is the KdV equation. They found that an initial condition decomposed into a finite number of waves, solitary waves, which then interacted cleanly, that is they did not change form upon interaction. They coined the term “soliton” to describe this particle-like behaviour of the solitary waves. This created much new interest in the solitary wave. As a result of this numerical study a more mathematically precise definition of a soliton was developed using two prominent features of the propagation of nonlinear waves.

A soliton:

- has a profile which is asymptotically constant at infinity; and
- can interact with other solitons without changing its form or identity. The only effect of a collision may be a phase change.

Adding to the revival of the solitary wave was the development of the inverse scattering transform [6] which offered an exact solution to the KdV equation. The KdV equation is then one of a class of equations terms integrable [7]. Although now many equations are now known to govern different types of solitary waves, it was Miura *et al* [8] who first showed that the KdV equation, is related to a linear equation, the Schrödinger equations, which determines the soliton solutions for a given initial condition via the method of inverse scattering.

The theoretical developments of the 1960s sparked interest in finding physical examples of solitary waves in various media, including nonlinear optical media. The exploration of solitary waves in nonlinear optics began with initial experiments into optical second harmonic generation by Franken [9]. Next came advances in materials engineering, with the development of low loss glass, which spurred interest in potential applications in optical communications. The prediction by Hasegawa and Tappert [10, 11] that these low loss glass fibres could support the propagation of stable temporal solitary waves, and was soon confirmed experimentally by Mollenauer in 1980 [12].

It was found that solitary waves exist in two forms, temporal and spatial, each defined by a different nonlinear effect. Descriptions of the two types of solitary waves are as follows:

- Temporal solitary wave: occurs in a dispersive medium, such as silica-glass fibres [12], with a temporal broadening of the beam. The mechanism that drives dispersion is a phase velocity difference between the frequency components of the beam. As the pulse evolves the beam frequency broadens as different components have different phase velocities, resulting in the frequencies moving at differing speeds. Finally, the beam disperses.

- Spatial solitary wave: a broadening of the beam due to diffraction. The difference in the spatial phase velocity of the components causes the beam to diffract.

Both temporal and spatial solitary waves can only exist if a counterbalance to the dispersion/diffraction is produced by the propagation medium. The broadening of the beam in both cases is balanced by a localised change in the refractive index of the medium. The nonlinearity of the medium modifies the refractive index, leading to "light induced lensing" [13] or "self-focusing" [14]. The combination of self-focusing and beam broadening allows the propagation (or evolution) of temporal and spatial solitary waves in nonlinear media. A change in the refractive index of a medium by a beam is known as nonlinear self-focusing. When this occurs the beam has formed its own waveguide and is said to be self-trapped [13].

In this thesis spatial solitary waves will be considered based upon these observations:

- the large nonlinearities associated with media that support spatial solitary waves produce interesting physical effects;
- the equations that govern the evolution of spatial solitary waves are highly dependent on the properties of the propagation medium. As a result, there is an immense number of media which support spatial solitary waves and the number of governing equations are vast, leaving much room for many original research paths; and
- keen interest has been aroused through the proposed use of spatial solitary waves in technology, especially in communications.

Based on these reasons spatial solitary waves in nonlinear soft media, specifically nematic liquid crystals, where the nonlinear response of the media is deemed nonlocal, will be the focus of this thesis.

1.2 Liquid crystal: Medium of propagation

Although numerous other optical media allow the formation of solitary waves, such as lead glass [15, 16], thermal liquids [17], ion gases [18], photorefractive crystals [19, 20] and Bose-Einstein condensates [21, 22], liquid crystals possess a nonlinear refractive index, where by a response extends beyond the local change in the refractive index to include the surrounding area of the media, termed nonlocal. The nonlocal response can also be observed in lead glass [15, 16] and thermal liquids [17]. In recent times, liquid crystals have received profound amounts of attention owing to their unique physical and optical properties. Physically, the liquid crystal molecules can flow like a liquid, but also maintain some degree of crystalline structure. Apart from this, liquid crystals can integrate seamlessly with current opto-electronic devices (due to their chemical stability), allowing for an easy transition to its use in all-optical communications. The amazing advantage that liquid crystals have over other optical media is its large nonlinearity, which exists in all of its phases, that is, the transition from one physical state to another physical state.

Liquid crystal is a thermotropic medium, which means that the phase's of the liquid crystal are temperature dependent. There are three distinct phases, which vary from a highly ordered molecular state (cold temperature) to a highly disordered molecular state (hot temperature). The anisotropic, or smectic phase, is a highly structured phase for which the molecules maintain positional and directional ordering in layers, similar to crystal lattices. The next phase is the nematic phase, for which the medium develops the fluidity of a liquid and loses positional ordering within the crystal. However, directional ordering is maintained in the form of a preferred average direction. The final phase is the isotropic phase, for which all order within the crystal is lost [23, 24].

1.2.1 Nematic liquid crystal

A nematic liquid crystal (NLC) or the nematic phase of the liquid crystal is of interest in this thesis. The nematic molecules are described as rod-like structures [23, 24, 25] with no positional order, but a tendency to naturally align due to intermolecular forces, with the long axes of the molecules being close to parallel and in a common direction. These nematic molecules are able to flow and are randomly positioned as if in a liquid, yet a long-ranged directional ordering is preserved in space. Further, the orientational order of the molecules, that is, a preferred average direction and a degree of angular/rotational ordering make NLC an attractive and flexible propagation medium.

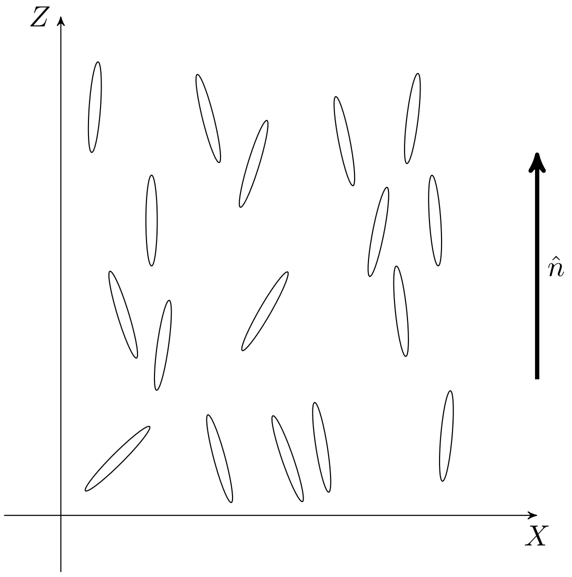

Figure 1.1: The molecular organisation of the nematic phase of a liquid crystal, indicating the preferred directional ordering in terms of the molecular director $\hat{n}$.

This preferred average direction is denoted by a unit vector called the molecular director, $\hat{n}$. Figure 1.1 shows the preferred average direction of the nematic molecules, plus their lack of positional order within NLC. The rod-like nature of nematic molecules means that the refractive indices for light polarised parallel and perpendicular to $\hat{n}$ are different. The refractive indices of the NLC orthogonal and parallel to $\hat{n}$ are defined in terms of the dielectric tensor ϵ of the nematic. That is, $n^2 = n_\perp^2 - n_\parallel^2$ where $n_\perp = \sqrt{\epsilon_\perp/\epsilon_0}$ and $n_\parallel = \sqrt{\epsilon_\parallel/\epsilon_0}$, and ϵ_0 is the vacuum dielectric permeability [25, 26].

Let us consider an ideal NLC, for which the molecules align to a common direction locally described by the director field $\hat{n}$. The organisation of the molecules becomes deformed due to interactions with confining boundaries (of interest in this thesis, see Chapters 3, 4 and 5) and/or applied electric or magnetic fields [27]. These deformations produce a change in the directional ordering of the molecules.

There are three specific macroscopic deformations that alter the molecular director. They are splay, twist and bend and are shown in figure 1.2. These deformations occur on a scale that is much larger than the molecular size, and can therefore be taken as constant everywhere and as elastic continuum theory applies. Elastic continuum theory states that a deformation can be modelled neglecting the medium structure at the molecular scale by associating an energy contribution to specific macroscopic deformations [23, 25].

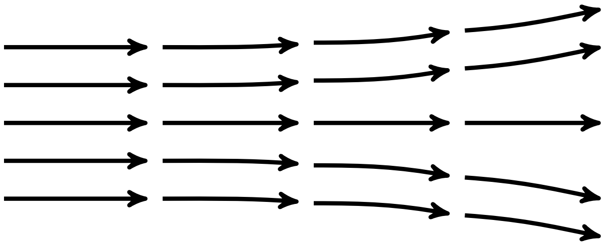

(a) Splay

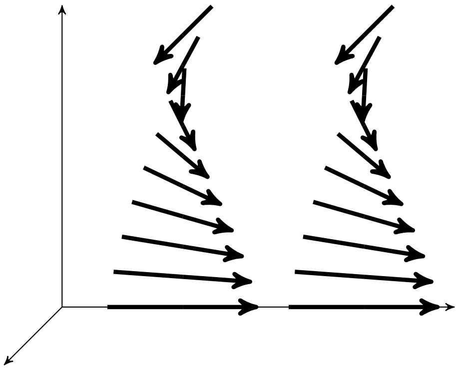

(b) Twist

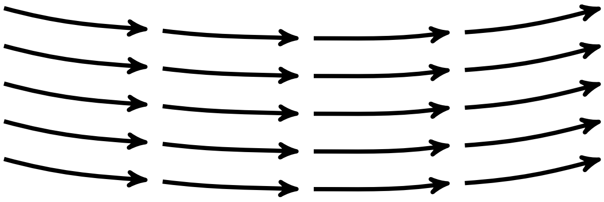

(c) Bend

Figure 1.2: Macroscopic deformations of NLC, splay, twist and bend.

The director distribution is also determined by the interaction of the NLC with confining surfaces, at which the nematic molecules can be anchored in a specific orientation. This interaction is normally a reactionary/restoring force. This force tends the restore the average direction of the molecular director whenever a perturbation occurs as a results of electric, magnetic and/or optical excitations [27]. When an electric field acts on NLC, a molecular dipole moment is induced, which aligns the molecule towards the field polarisation direction. Hence, a strong electric field increases the alignment between the director axis and the field polarisation direction.

In optical terms, the rotation of the nematic molecules via the induced dipole moment changes the refractive index of the NLC, which produces a nonlinear self-focusing response in the medium [23, 24]. Further, optically induced distortions in NLC are opposed by the elastic nature of the nematic which seeks to distribute the internal stresses within the NLC, resulting in a smoothing relaxation away from the point of maximum intensity [28]. This smoothing behaviour of the NLC is known as a nonlocal effect, whereby the nematic molecules beyond the optical waist of the beam are also distorted by the dipole moments, but to a lesser extent as the position moves farther from the centre of the optical beam.

1.2.2 Nematicon: A solitary wave in NLC

The properties of NLC allow the formation of a solitary wave, termed a nematicon [29]. Before we look at the formation of a nematicon, let us go back to NLC and find out what happens when a coherent optical beam, such as a laser, enters the medium.

As with any light source when it enters a more optically dense medium, the optical beam linearly diffracts, as shown in figure 1.3(a). At the other extreme, the optical beam can induce a local change in the refractive index of the NLC, which results in a self-focusing of the optical beam to a point. Figure 1.3(b) depicts pure self-focusing of an optical beam. Both the pure linear diffraction and pure self-focusing responses, respectively, have an on-axis phase shift, denoted by Δ_D and Δ_F respectively, due to the curved wavefronts of the optical beam, clearly shown in figure 1.3.

A nematicon is formed due to a balance between these two optical effects, linear diffraction and self-focusing. Imposing the nonlinear compensation of diffraction results in $\Delta_D + \Delta_F = 0$. This balance results in a self-trapped beam or nematicon, as shown in figure 1.4.

Collapse and nonlocality

The stability of a nematicon is due to the nonlocality of the NLC. This can be demonstrated by looking at a local medium such as a Kerr medium. Nonlinear beam propagation in local Kerr media is governed by the nonlinear

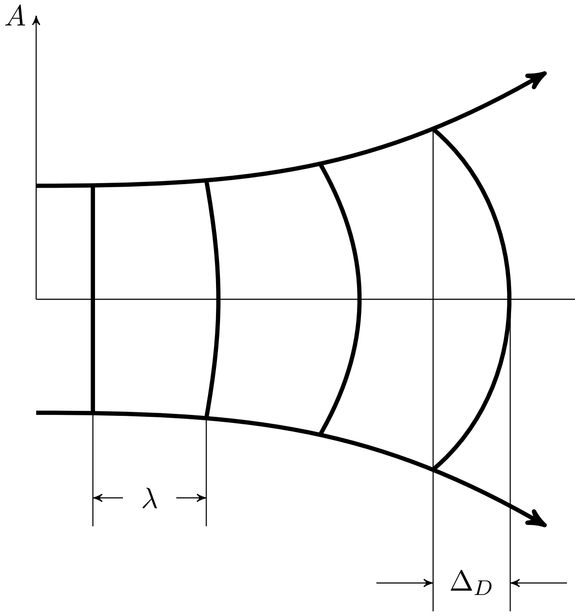

(a) Pure linear diffraction of an optical beam.

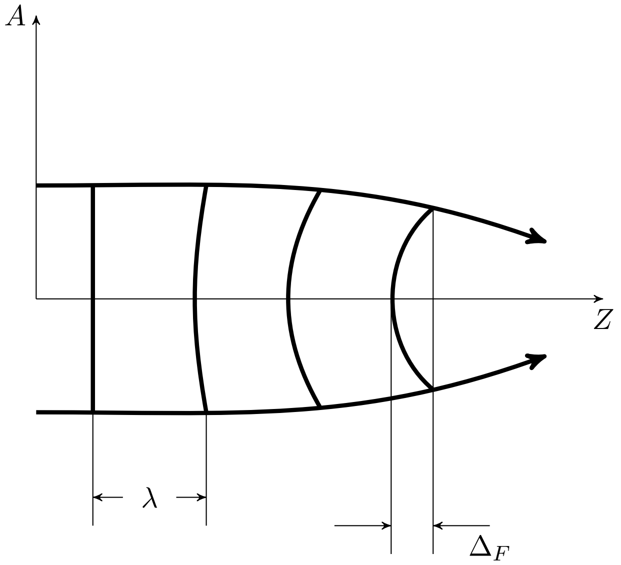

(b) Pure self-focusing of an optical beam.

Figure 1.3: Pure linear diffraction and pure self-focusing, where λ is the wavelength of the optical beam, Δ_D is the diffractive on axis phase shift and Δ_F is the self-focusing on axis phase shift.

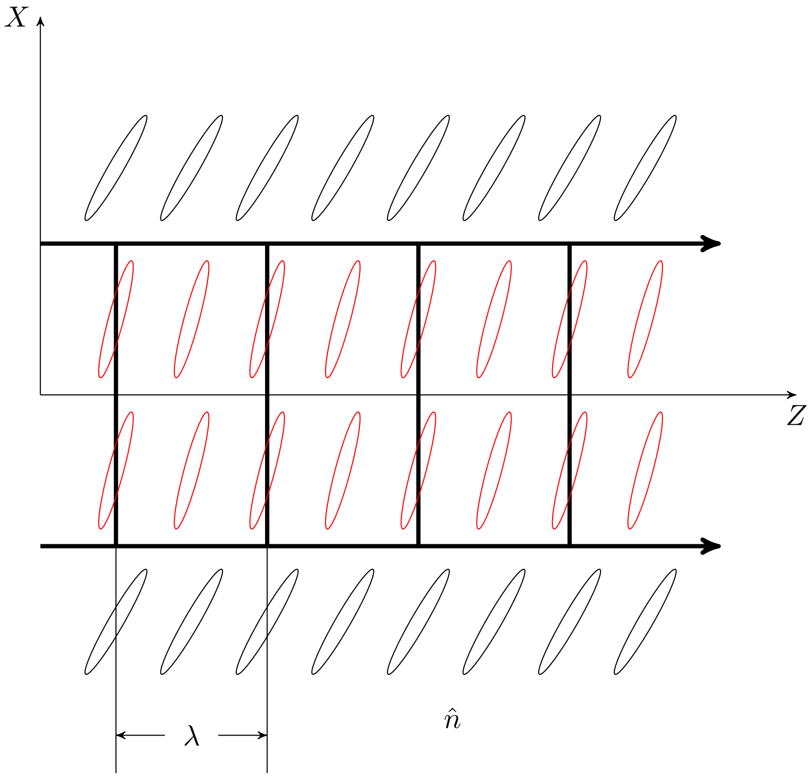

Figure 1.4: A self-trapped optical beam, indicted by the larger rotation angle formed with the Z axis (red nematic molecules) and a lesser rotation due to the nonlocality outside the confines of the optical beam. λ is the wavelength of the optical beam and $\hat{n}$ is the average director direction.

Schrödinger (NLS) equation

$$i\frac{\partial u}{\partial z} + \frac{1}{2}\nabla^2 u + |u|^2 u = 0. \tag{1.1}$$

In one space dimension, $\nabla^2 u = u_{xx}$, the NLS equation is exactly integrable [7] and solitary wave solutions are stable. However, in two space dimensions, $\nabla^2 u = u_{xx} + u_{yy}$, solitary wave solutions of the NLS equation show catastrophic collapse, that is they become of infinite amplitude and zero width in finite z. In contrast to this, in NLC the medium response is nonlocal, that is the nematic response extends beyond the optical beam due to elastic forces. As a result the refractive index perturbation is wider than the actual beam, affecting the nematic molecules outside of the optical beam [30]. This stabilises the a nematicon [25]. Further, an increase in the power of the nematicon creates a weakening in the self-focusing ability of the beam, thus preventing the usual collapse associated with solitary waves in 2D local media and so sustaining the nematicon.

Freéedericksz threshold

To enable the self-focusing of an optical beam in NLC and thus obtain a nematicon, a minimum power level is required to induce a change in the refractive index (molecular rotation) of the NLC which will result in the self-focusing of the optical beam, hence a threshold exists. Initially, the nematic molecules are perpendicular to the polarisation direction and the threshold is at a maximum. This minimum power level is known as the

Freédericksz threshold [25, 28]. Originally, when NLC was first [31] being considered as a propagation medium, difficulties in obtaining a self-focusing response were encountered. The use of large optical beam powers $O(1 \text{ Watt})$ met the threshold limit and induced a change in the refractive index, but at the same time introduced thermal effects due to localised heating of the NLC [31]. External cooling of the NLC was attempted to counteract the localised heating [31], but was cumbersome. Introducing a dye into the NLC, reduced the power level of the optical beam needed to obtain self-focusing, and an increase in the nonlinear response was observed [32]. However, thermal effects were still present which altered the properties of the nematic. An idea emerged to use the pre-existing properties of the NLC to an advantage, which allowed for smaller optical beam powers to be used $O(1 \text{ mW})$ and so negated thermal effects. The self-focusing of the optical beam requires the nematic molecules to rotate. Hence, by applying a low-frequency static external electric field to the NLC in the direction perpendicular to the optical beam's propagation direction (optical beams polarisation direction), that is, the X direction, the nematic molecules could be pre-tilted [29]. Thus, the self-focusing of the optical beam is aided as it no longer requires such a large optical beam power to excite molecular rotation. A combination of an applied external static electric field and the optical beam's electric field can also meet the minimum power requirements to induce molecular rotation of the nematic molecules. Hence, the balance required to self-trap/form a nematicon is struck at low optical powers. Further, the ideal molecular pre-tilt angle was found to be $\pi/4$ with the Z axis, as this reduced the Freédericksz threshold to zero [33]. Experimentally, the pre-tilt angle is set to be less then $\pi/4$, but close to this angle [25, 29].

1.3 Nematicons and experimental observations in NLC

Let us consider a NLC cell sandwiched between two glass plates, with the nematic molecules in a planar configuration in the $X - Z$ plane, as shown in figure 1.5 with the director parallel to the Z axis. Indium-tin-oxide film electrodes are deposited on the inside of the glass plates containing the NLC to allow a low-frequency voltage to be applied across the NLC thickness. Polymer films are also applied to the inner sides of the glass plates [23] and manually rubbed to excite the planar anchoring of the nematic molecules at the boundaries. A third glass plate seals the NLC-air interface to stop a meniscus forming, which could alter the polarisation and phase distribution of the input optical beam [29, 34, 35, 36]. This experimental setup is shown in figure 1.5.

An optical beam is launched into the NLC cell along the Z direction, and is polarised in the X direction. The beam's polarisation direction causes the nematic molecules to try to directionally align themselves with the beam's

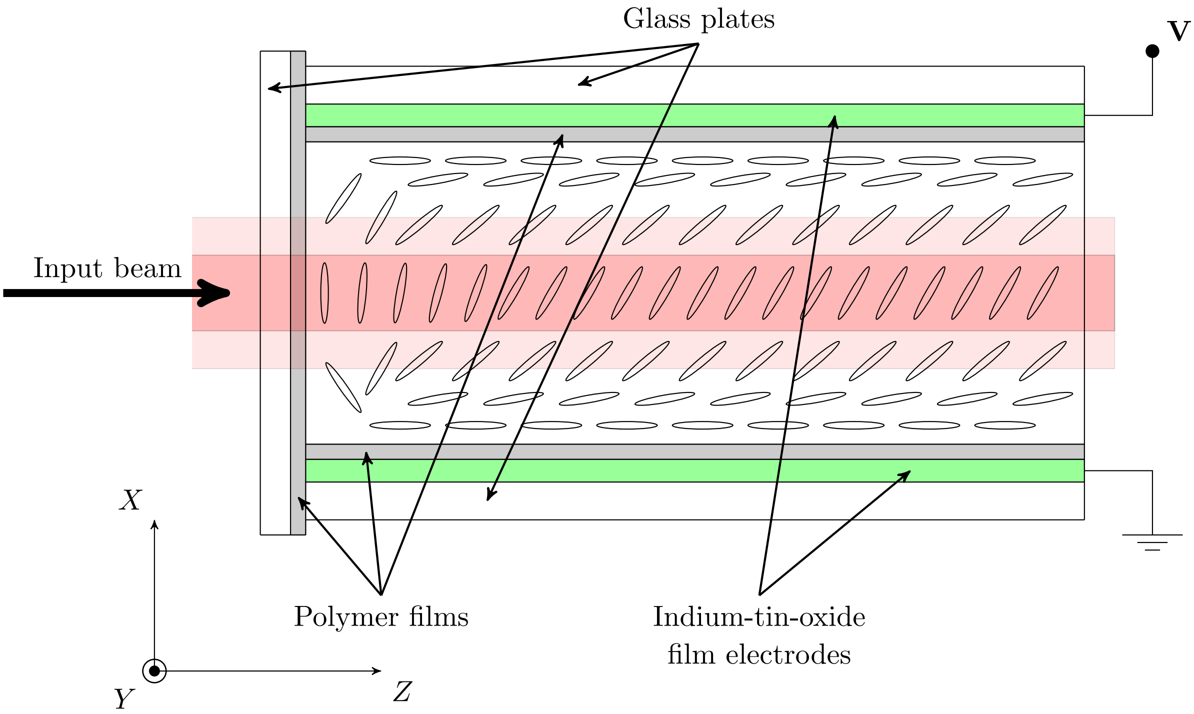

Figure 1.5: The experimental setup showing a cross section of the NLC cell. The diagram indicates how the nematic molecules are affected by the optical beam. Note, that the nematic molecules on the boundaries are anchored at an angle of zero.

polarisation, thus rotating the nematic molecules in the $X - Z$ plane. As explained in the above section, the molecular rotation induces beam self-focusing, which is balanced by the linear diffraction of the beam to form a self-trapped waveguide (nematicon) within the NLC cell. This nematicon was first observed using an initial pre-tilt (avoiding the Freédericksz transition) of the nematic molecules via an external bias applied in the X direction [35].

The waveguide nature of a nematicon lead to the question, could a weaker linear beam be co-launched with the initial beam, and what will the outcome be? That is, can a nematicon act as a waveguide? This procedure is called “probing” and takes two beams with the same polarisation and propagates them together [36]. It was found that the nematicon would trap the probing beam. Thus, the probe could be launched using a beam with a different wavelength and/or an alternative initial angle and each time the nematicon would confine the beam. Further, the nematicon could steer the probe by altering its own path [14, 37, 38].

The optical properties of the nematic is governed by a refractive index which is a determined by a tensor response. For a uniaxial crystal, such as a nematic liquid crystal, this tensor gives two eigendirections, termed ordinary and extraordinary waves [39] (section 12.8). The ordinary waves are non-dispersive, and so do not form solitary waves. However, at large power levels the optical beam can self-focus and be balanced by higher order nonlinear contributions to dispersion. This area has not been experimentally or theorectically explored. The extraordinary waves are dispersive and so can form solitary waves. A nematicon is then formed from the extraordinary response of the NLC. The extraordinary waves have a group velocity which is at an angle to the wavevector of the input beam. Hence a nematicon propagates at an angle to the input beam, which is termed walk-off [40, 41]. The mathematical models presented throughout this thesis have factored out the (constant) walk-off angle by using a phase shift, details of which can be found in reference [42].

In early experiments on the formation and steering of nematicons, the NLC cell was considered to be infinitely thick for simplicity. The effects of the cell walls were assumed negligible and that they did not impose on the propagation dynamics of the nematicon. This was assumed a good approximation for a nematicon propagating in the centre of a cell with a typical cell width being 24 times the width of a nematicon [36]. However, an experimental study [43] found a power dependent relationship between the boundary and a nematicon's trajectory. The boundaries were found to repel the nematicons based on beam power, with larger beam intensities corresponding to stronger repulsion. The underlying mechanism responsible for the stronger repulsion for higher beam power was the nonlocality of the nematic, as more nematic molecules were affected by the presence of the beam [43, 44]. A continuation of the investigation of the effect of cell boundaries on the trajectories of optical beams in finite-sized NLC cells [30, 43, 44, 45, 46] will be theoretically studied in Chapters 3, 4 and 5.

Alternative beam structures have been of interest in the study of optical phenomena, with the optical vortex [47, 48, 49] being an example. An optical vortex when viewed along its axis resembles a ring, with a phase singularity present at its centre. This phase singularity causes the instability of an optical vortex in local media [50, 51]. However, the nonlocality of NLC smooths the nematic's response at the centre of the optical vortex, and hence, stabilises it [52, 53]. The effects of the NLC cell boundaries on the stability of an optical vortex will be examined, as well as on its trajectory, in Chapter 4.

Applying orbital angular momentum to an optical beam has sparked interest in the potential use of optical beams as manipulative tools [54], giving experimentalists the ability to control, trap (using an optical vortex), and move individual small particles within a medium. Examples of these are the optical spanner [55] and optical rotating turbines [56]. An elliptically shaped optical beam with orbital angular momentum is also a possible manipulation tool. Such a beam is studied in Chapter 5.

In summary, NLC has a huge nonlinearity, so that nonlinear optical effects can be observed over millimetre distances [57]. The nonlinearity is saturable [58], aiding the stability of propagating solitary waves. However, the nonlinear response time of NLC ($\sim$ 0.1 s) [29] is too slow for many applications, as seen by the "ghosting" of liquid crystal televisions during fast motion. Further, experiments conducted on optical interconnects give a reaction time of seconds [14] for NLC, while current electrical interconnects respond within microseconds. There is currently work being conducted on NLC to improve the reaction time to enable more applications of NLC to optical devices.

1.4 Aims of thesis

The research presented in this thesis aims to fill the gap in the current understanding of boundary interactions between a finite-sized NLC cell and different optical beam structures, specifically a nematicon (circular), an optical vortex solitary wave and an elliptically shaped optical beam. In Chapters 3, 4 and 5 variational (modulation) theory will be employed to derive semi-analytical solutions of the equations governing optical beams in NLC for these three beam types. The equations governing nonlinear optical beam propagation in NLC form a coupled system of a NLS-type equation for the optical response and a Poisson's equation for the mediums response. The highly nonlinear, coupled nature of the equations means that there are no exact solutions. Hence approximate and numerical solutions are the only possible methods to analyse solutions of these equations. These solutions will be compared with full numerical solutions of the governing equations to determine the variational solutions accuracy and utility.

The derivation of the equations that govern an optical beam in NLC will be derived in Chapter 2. The semi-analytical method used to analyse solutions of these equations will be introduced through a simple example of a nematicon in a $(2 + 1)$ dimensional (D) infinitely thick NLC cell. A description of full numerical scheme used to solve the equations of this thesis will conclude the chapter.

Chapter 3 will study the propagation of a nematicon in a $(2+1)$D finite-sized NLC cell. Particular attention will be placed on the effect of the boundaries on a nematicon. The novel solution technique of the method of images will be introduced to solve the equation governing the director perturbation.

Chapter 4 will explore the propagation of a stable optical vortex in a bounded NLC cell. A linearised stability analysis will provide an analytical expression for the minimum distance an optical vortex can approach a boundary before instability sets in.

Chapter 5 studies elliptically shaped optical beams with orbital angular momentum in a finite-sized NLC cell. In the process, two different variational methods will be compared and contrasted with each other and their accuracy determined by comparison with full numerical solutions of the governing equations. It will be shown that angular momentum is shed by the optical beam and an accounting of this is required to gain a reasonable comparison with full numerical solutions.

The concluding Chapter 6 will summarise the findings for the different optical beam structures in finite-sized NLC cells and briefly explore future research avenues in NLC and other optical media.

Chapter 2

Equations and methodology

2.1 Introduction

This chapter gives an overview and description of the fundamental set of equations used to model the propagation of coherent light through a medium of soft matter. In particular, this medium will be nematic liquid crystal (NLC). These equations are two coupled partial differential equations (PDEs) which describe the electric field envelope of a light beam and the behaviour of the NLC when this light beam propagates through it. Since this system of equations does not have exact solutions, this chapter will describe the general asymptotic approach used to obtain a semi-analytical solution for nonlinear light beam propagation in NLC. Using a $(2+1)$D example, it will be shown how solitary waves (known as nematicons in NLC) are formed and how diffractive radiation loss has to be considered if the analytic solution is to compare favourably with numerical solutions. It should be noted that the term solitary wave and soliton will be used when discussing general applications to a range of media, whereas, nematicon is specific to solitary waves in NLC.

2.2 The governing equations

Maxwell's equations describe the general evolution of electromagnetic waves. These equations can be solved using numerical techniques, but this loses the deep insight into how waves evolve and propagate through time and space. For example, numerical studies of a light beam propagating through a NLC (or nematic) misses the molecular-electric field interaction between the nonlocal response of the nematic and the electric field of the light beam [59], as well as other effects such as low frequency dispersive radiation [60].

As they stand, Maxwell's equations are far too complicated to be solved analytically. However, using a narrow-beam asymptotic analysis under the paraxial approximation, which is a more general approach of geometric optics [28, 39], Maxwell equations can be reduced to a single nonlinear PDE which is strongly coupled to another PDE describing the nonlinear response of the medium. For instance, McLaughlin *et al* [28] showed that for a light beam propagating in an NLC, Maxwell's equations could be reduced to a Helmholtz equation coupled with a Poisson equation. This system was used for an exploration of the self-focusing effect of optical beams. Further analysis showed that the Helmholtz equation could be transformed to a nonlinear Schrödinger (NLS)-like equation, while still maintaining the coupling to the Poisson equation [28, 35]. The equations governing the propagation of a coherent polarised optical beam in NLC in the presence of an external static electric field [29, 38, 61] are given by

$$i2k\frac{\partial u}{\partial Z} + \nabla^2_{XY}u + k_0^2\epsilon_a\left(\sin^2\phi - \sin^2\hat{\theta}\right)u = 0 \tag{2.1}$$

$$4K\nabla^2_{XY}\phi + 2\Delta\epsilon_{RF}u_S^2\sin(2\phi) + \epsilon_0\epsilon_a\sin(2\phi)\,|u|^2 = 0, \tag{2.2}$$

where u is the complex envelope of the beam's electric field, Z is the propagation direction of the beam, X is the polarisation direction of the light beam and is orthogonal to Z, while Y is orthogonal to both X and Z. Induced by the combination of the external static electric field and the electric field of the propagating light beam, the total reorientation of the director field can be written as

$$\phi = \hat{\theta} + \theta, \tag{2.3}$$

where $\hat{\theta}$ is the pre-tilt angle for the molecular reorientation induced by the external static electric field applied in the X direction, so that molecular rotation occurs in the $X-Z$ plane, while θ is the optically induced rotation of the director due to the electric field of the light beam. For the usual milliwatt optical beam powers, $\theta \ll \hat{\theta}$. Furthermore, k is the propagation constant (wavenumber) of the beam and $k_0 = 2\pi/\lambda_0$ is the initial wavenumber of the beam with λ_0 being the input wavelength. The constants $\epsilon_a = n_\parallel^2 - n_\perp^2$ and ϵ_0

are the optical birefringence and the permittivity of free space respectively, $n_\parallel$ and $n_\perp$ being the refractive indices for an optical beam parallel and orthogonal to the director alignment [25, 38]. u_S is the strength of the applied external static electric field and $\Delta\epsilon_{RF}$ is the static anisotropy. K is the Frank constant which measures the elasticity of the medium and is taken equal for splay, twist and bend deformations of the nematic molecules, as shown in figure 1.2.

Poisson's equation (2.2) for the optical axis ϕ is derived from the free energy of the nematic, which is a combination of the electric field-molecular dipole interaction and the energy due to a perturbation of the director field which is the addition of the elastic responses to splay, twist and bend [23, 25, 38]. Hence, Poisson's equation governs the total reorientation of the nematic molecules.

Let us non-dimensionalise the nematic equations by

$$X = \alpha x, \quad Y = \alpha y, \quad Z = \beta z \quad \text{and} \quad u = AEe^{i\gamma z}. \tag{2.4}$$

Equation (2.1) then becomes

$$i\frac{\partial E}{\partial z} + \frac{1}{2}\nabla_{xy}^2 E - \cos(2\phi)\, E = 0, \tag{2.5}$$

where the non-dimensionalising parameters in (2.4) are

$$\alpha = 2/k_0\sqrt{\epsilon_a}, \quad \beta = 4k/k_0^2\epsilon_a \quad \text{and} \quad \gamma = \beta k_0^2\epsilon_a \cos(2\hat{\theta})/4k. \tag{2.6}$$

Equation (2.5) is now in the form of the well known Foch–Leontovich equation [62].

Equation (2.2) can also be non-dimensionalised using the same change of variables given by (2.4). Equation (2.2) becomes

$$\nu \nabla_{xy}^2 \phi + p \sin(2\phi) + 2\sin(2\phi)\,|E|^2 = 0, \tag{2.7}$$

where

$$\nu = 8K/\epsilon_0\epsilon_a \quad \text{and} \quad p = 4\Delta_{\epsilon RF} E_S^2/\epsilon_0\epsilon_a. \tag{2.8}$$

The Laplacian (∇_{xy}^2) in equations (2.5) and (2.7) in the $x - y$ plane. For convenience, the subscript that appears in both equations (2.5) and (2.7) will be dropped. The Laplacian will be assumed to act in the $x - y$ plane unless otherwise stated. Also, non-dimensional variables will used, except where it is vital for clarity. The parameter ν in equation (2.7) quantifies the inter-molecular elastic links between the nematic molecules and is a measure of the nonlocality of the nematic. Small values of ν correspond to the local limit and are associated with the formation and propagation of Townes solitons [63], while large values of ν correspond to the nonlocal limit. The parameter p is related to the strength of the external static electric field used to pre-tilt the nematic molecules. It is assumed that at the cell boundaries the director angle is fixed, that is, $\phi = \phi_0$. Using (2.3), equation (2.7) expands to become

$$\begin{aligned} &\nu\nabla^2\hat{\theta} + \nu\nabla^2\theta + p\sin(2\hat{\theta})\cos(2\theta) + p\cos(2\hat{\theta})\sin(2\theta) \\ &+ 2\sin(2\hat{\theta})\cos(2\theta)|E|^2 + 2\cos(2\hat{\theta})\sin(2\theta)|E|^2 = 0. \end{aligned} \tag{2.9}$$

By adjusting the pre-tilt angle so that $\hat{\theta} \geq \pi/4$ in the centre of the $x - y$ plane of the NLC cell, the molecular rotation, which enables self-focusing of the light beam, will permit the optical intensity to be above the Freédericksz threshold. To maximise the effect of the external electric field and minimise the optical beam power, the pre-tilt angle $\hat{\theta}$ is also set to be greater than $\pi/4$, but close to it as the Freédericksz threshold is zero when $\theta = \pi/2$ also, the NLC has a saturation limit which is reached when $\phi = \pi/2$, this angle being the maximum angle of rotation of the molecules in the $x - z$ plane.

The pre-tilt angle is determined by the director equation (2.9) when $E = 0$. Hence, the director angle satisfies equation

$$\nu\nabla^2\hat{\theta} + p\sin(2\hat{\theta}) = 0, \tag{2.10}$$

with the angle at the boundaries anchored at $\hat{\theta} = 0$. Note that the pre-tilt angle $\hat{\theta}$ is solely due to the static external electric field, p. Equation (2.9) can be simplified further by substituting equation (2.10) and using the small angle approximation for θ, $|\theta| \ll \hat{\theta}$, so that the last term in (2.9) is of lower order

$$\nu\nabla^2\theta + p\sin(2\theta)\cos(2\hat{\theta}) + 2|E|^2\cos(2\theta)\sin(2\hat{\theta}) = 0. \tag{2.11}$$

The slowly varying functions $\cos(2\hat{\theta})$ and $\sin(2\hat{\theta})$ can be replaced with typical values found at the cell's centre in the $x - y$ plane, where the nematicon propagates. Also, recall that the external field is chosen to result in $\hat{\theta} > \pi/4$, but close to $\pi/4$ in the centre of the cell. Then $\sin(2\hat{\theta}) \sim 1$ and $\cos(2\hat{\theta}) <$

0. Hence, rescaling of the director equation (2.11) results in the further simplification

$$\nu\nabla^2\theta + q\sin(2\theta) + 2|E|^2\cos(2\theta) = 0, \tag{2.12}$$

where the parameter q is the rescaling of the low frequency external electric field.

Applying an argument similar to that for the director equation above, the Foch–Leontovich equation (2.5) can be simplified to the form

$$i\frac{\partial E}{\partial z} + \frac{1}{2}\nabla^2 E + \sin(2\theta)\,E = 0. \tag{2.13}$$

Using the small angle deviation limit for θ, the governing equations (2.12) and (2.13) for the propagation of a nematicon with an applied external static electric field can be simplified as:

$$i\frac{\partial E}{\partial z} + \frac{1}{2}\nabla^2 E + 2\theta E = 0, \tag{2.14}$$

$$\nu\nabla^2\theta + 2q\theta + 2|E|^2 = 0. \tag{2.15}$$

In recent years an alternative pre-tilt technique for NLC has been developed, whereby the glass plates which contain the nematic are “rubbed” [30, 44]. A static charge is induced in the rubbed cell walls which excites a dipole moment in the adjacent nematic molecules, thus causing the nematic molecules to rotate. This induced static charge in the form of a molecular rotation is now passed to the neighbouring nematic molecules via the elastic inter-molecular forces (nonlocality). Hence, the pre-tilt angle $\hat{\theta}$ is uniformly distributed (approximately) throughout the NLC cell. The static external electric field is no longer needed to pre-tilt the nematic molecules and the term describing the external field's strength is zero as $q = 0$. Hence, the director equation (2.15) is then simplified to

$$\nu \nabla^2 \theta + 2|E|^2 = 0. \tag{2.16}$$

Thus, equations (2.14) and (2.16) are the basic system of coupled PDEs that govern nonlinear optical beam propagation in NLC when rubbing is used to pre-tilt the nematic molecules, from the weakly nonlocal limit Townes solitons ($\nu \to 0$) and to highly nonlocal limit accessible solitons ($\nu \to \infty$). Nevertheless, these equations are universal and appear as the governing equations for other nonlinear optics problems, such as thermal media [16, 64, 65] and certain photorefractive crystals [66, 67].

2.3 Approximate methods

In order to mathematically model the evolution of a light beam as it propagates through a NLC, a semi-analytical approach is adopted here as there are no exact solitary wave solutions of the governing equations, this semi-analytical approach has major benefits over a purely numerical studies of the governing equations (2.14) and (2.16) as it yields insights into the underlying mechanisms and the features which control the evolution.

Reviewing the governing equation (2.14), we can see that this equation closely resembles the 1D NLS which has known solitary wave solutions. With this in mind, the semi-analytical approach is based on a trial function for the light beam that is similar to the soliton solution of the 1D NLS. The trial function has various parameters such as width, amplitude, position and shelf height that vary with the propagation variable z, which acts as a time-like variable in the equations. These parameters will govern the beam formation and its evolution.

Due to the simplifications, the approximate method imposes conditions on the beam profile, which means that key features of its evolution may be removed or restricted. To avoid the shortcomings of this method, a careful choice of trial function is required. Hence, the chosen trial functions for both the light beam's envelope and the nematic's response to the light beam such that they give a reasonable approximation to the actual solution profiles. It will be shown later that these trial functions compare favourably with the full numerical solution which is then ultimate justification. This successful choice of trial function will lead to insights into the underlying physics and mechanics of the beam formation, propagation and dynamical behaviour that is not obtainable from numerical techniques.

2.3.1 Trial function

As discussed in this chapter, a trial function is used as an approximation for the light beam's envelope as exact solutions for the governing equations

(2.14) and (2.15) are unknown. Apart from assuming a 1D NLS type solution for the form of the trial function, the best choice for a trial function is one that has the correct asymptotic behaviour as $x \to \pm\infty$ and is a good match to the full numerical solutions. Generally, there are no real mathematical constructs or rules which dictate the choice of trial function. However, Malomed [59] mentioned some points to consider when choosing the trial function:

- Necessity to perform analytic integration;
- Need for a balance between a simplistic and complicated trial function; and
- Steady state solutions for the dynamical system have no direct link to the trial function.

As stated above, the electric field envelope is governed by the NLS-like equation (2.14). The (1+1)D NLS equation, whose solution can be determined using inverse scattering, is used as an initial launch pad to develop a trial function which best fits the profile of the light beam. Now, the trial function must incorporate parameters which capture the behaviour of certain features of the light beam, such as amplitude, width, position and phase.

Anderson [68] was the first to successfully realise the potential of variational theory and apply the idea of a trial function to the problem of a solitary wave in a nonlinear fibre optic cable, which was governed by the

NLS equation. Further, Anderson used a version of the trial function incorporating "chirp", which is due to the addition of quadratic corrections in the phase. This initial work led the way for the use of variational techniques in conjunction with dynamical systems and has since been tried and tested for many nonlinear optical problems [59, 68]. Beyond these initial applications, the method has been adapted for use in many different optical scenarios, such as Bose–Einstein condensates [69] and Kerr media [50].

Typically, the trial function takes the form of a basic beam profile

$$E = f(h_1(z), h_2(z), \ldots, h_N(z)) \tag{2.17}$$

where the parameters are given by $h_i(z)$, $i = 1, \ldots, N$, and N is the total number of parameters. Note that the parameters in the trial function (2.17) vary with respect to the propagation distance z.

To obtain a dynamical system governing the evolution of an optical beam based on this trial function, the trial function (2.17) is substituted into the Lagrangian formulation of the governing equations. This Lagrangian is then averaged [39] by integrating in the spatial variables x and y, so that the averaged Lagrangian depends on the propagation coordinate z only. In the original formulation of modulation theory by Whitham [39], the wave envelope was assumed to be slowly varying, so that this averaging process integrated out the fast phase dependence. Whitham then showed that modulation theory is equivalent to the standard asymptotic technique of the method of averaging, or multiple scales.

A set of variational equations, known as modulation equations, arise from the averaged Lagrangian $\mathcal{L}$ for each of the parameters $h_i(z)$ by way of the Euler–Lagrange equation, are

$$\frac{d}{dz}\frac{\partial \mathcal{L}}{\partial (h_i')} - \frac{\partial \mathcal{L}}{\partial h_i} = 0. \tag{2.18}$$

Equation (2.18) forms a system of first-order nonlinear ordinary differential equations (ODEs), a dynamical system. These can be solved using a simple numerical scheme, such as the standard fourth-order Runge–Kutta.

Writing the system in terms of Lagrangian actions and modulation equations allows the application of Nöther's theorem. This theorem permits the determination of conserved quantities from symmetries of the underlying Lagrangian. Nöther's theorem relates the lack of explicit dependence of the Lagrangian on the time-like variable z to the conservation of energy. Any Lagrangian L has a translational symmetry in z [70]

$$\frac{\partial (h_i')}{dz}\frac{d}{dz}\frac{\partial \mathcal{L}}{\partial (h_i')} - L = 0, \tag{2.19}$$

where the summation convention has been used. The variational method and the principle of stationary action are closely linked to the infinite number of conservation equations found in integrable systems. In fact, each of the variational equations given by the Euler–Lagrange equation (2.18) can be obtained by calculating the conserved quantities associated with the governing equations (2.14) and (2.15) [39].

2.3.2 Extension of the trial function

Solutions of the modulation equations as derived above will not evolve to a steady state. This is because the effect of the diffractive radiation shed by a solitary wave as it evolves has not been included. This shed radiation acts as a damping, allowing the wave to evolve to a steady state. However, a study by Kath and Smyth [60] proposed an extension to the trial function and variational theory. A (1+1)D soliton in an optical fibre governed by the 1D NLS equation was analysed. It was shown that over short propagation distances (small z), the existing approximate theory and trial function were adequate at describing the evolution of the light beam, but was unable to provide good comparisons over large distances. This was due to the variational theory being unable to capture the damping of the amplitude oscillations to a steady state experienced by the soliton, which was present in full numerical solutions. The break-through by Kath and Smyth [60] occurred when they linked the evolution to a steady state to radiation loss by the soliton. The observed damping was shown to be the effect of mass loss in the form of dispersive radiation shedding. This was the key to matching the variational approximations to the actual behaviour of the physical system.

As a consequence, a modification was made to the initial trial function to include radiation. The mass loss was also included in the modulation equations. This had the effect of damping parameter evolution to a steady state solitary wave. Hence, this modification produced excellent agreement with full numerical solutions of the NLS equation. Not only did the addition of the radiation loss allow for a valid approximation over large propagation distances, it extended the variational method to a wider range of optical soliton regimes, even non-integrable systems [60, 71].

This modified variational method will form the basis of the analysis throughout this thesis. Any details that differ from the approximate method presented here will be highlighted at the appropriate place.

2.3.3 A nematicon in the nonlocal limit: An illustrative example

To demonstrate the theory presented in Sections 2.2 and 2.3 and to outline the extended variational technique of Kath and Smyth [60], a simple example of a $(2+1)$D nematicon in the nonlocal limit (ν large) will be reviewed [72]. In this example, the x and y boundaries of the NLC cell are considered to be infinite. The nematic molecules will be pre-tilted by an external static electric field applied in the x direction.

Equations (2.14) and (2.15) in radially symmetric polar form, are

$$i\frac{\partial E}{\partial z}+\frac{1}{2r}\frac{\partial}{\partial r}\left(r\frac{\partial E}{\partial r}\right)+2\theta E=0 \tag{2.20}$$

$$\nu\frac{\partial^2\theta}{\partial r^2}-2q\theta+2|E|^2=0, \tag{2.21}$$

where $r^2=x^2+y^2$. Here, E as described above, is the complex valued envelope of the electric field of the optical beam, θ is the perturbation of the director from the pre-tilt angle in the $x-z$ plane, ν is the elastic response of the nematic molecules and is related to the nonlocality of the medium and q is the non-dimensional value of the static electric field externally applied to the nematic in order to pre-tilt the molecules.

The analysis begins by writing the governing equations (2.20) and (2.21) in the form of a Lagrangian

$$L = ir\left(E^* E_z - E E_z^*\right) - r|E_r|^2 + 4r\theta|E|^2 - \nu r\theta_r^2 - 2qr\theta^2, \tag{2.22}$$

where $*$ represents the complex conjugate.

An appropriate trial function or ansatz is now chosen whose parameters vary independently with z (the propagation direction). In Section 2.3, the (1+1)D soliton solution of the NLS equation was suggested as an appropriate initial starting point for a trial function. This solution is given by the sech profile

$$E = a\,\mathrm{sech}(ax)e^{ia^2 z/2}. \tag{2.23}$$

A similar profile will be used as the trial function for E and θ in our governing equations (2.20) and (2.21).

Numerical simulations [60] for the $(1+1)$D NLS equation show a shelf of low-wavenumber diffractive radiation forming under the beam as it propagates. The existence of this shelf has been verified using perturbative techniques and perturbed inverse scattering [60, 73]. Using a simple argument based on group velocity, this shelf of radiation will be explained below.

Linear waves describing the diffractive radiation of the NLS-like equation

(2.20) have group velocity $c_g = k$. Hence, low wavenumber waves have a low group velocity and remain within the vicinity of the nematicon. There is then a continuous interaction between this shelf of low wavenumber radiation and the nematicon [60, 71]. To account for the presence of the shelf, a term corresponding to the shelf height or shelf amplitude is included in the trial function for the optical beam based on equation (2.23). That is,

$$E = a \operatorname{sech}\left(\frac{r}{w}\right) e^{i\sigma} + ige^{i\sigma}. \tag{2.24}$$

Here, the amplitude a, width w, phase σ and shelf amplitude g are the nematicon parameters which vary independently with z.

Perturbative analysis [60, 73] showed that the nematicon and the shelf of radiation that accumulates under the nematicon are $\pi/2$ out-of-phase. This is reflected in the ansatz (2.24) by the multiplication of the shelf amplitude g by i and can be observed in the oscillation of the nematicon amplitude, where an increase in amplitude occurs when the shelf feeds into the nematicon, that is, the maximum amplitude occurs when they are out of phase. The shelf of diffractive radiation is assumed to be flat within the disc $0 \leq r \leq \ell$, where ℓ is the shelf radius (which needs to be determined). Outside of this shelf, g is taken to be zero. The form of the radiation outside of this shelf will be discussed below. The shed radiation that is travelling near the nematicon (the shelf) can be incorporated into suitably chosen trial functions, but the far field radiation is not included in the chosen trial function. The incorporation of the shed diffractive radiation is essential to allow the nematicon to settle towards a steady state. Otherwise there will be no damping and the nematicon will continue to oscillate around the steady state. However, over short propagation distances $z \leq 100$, the importance of the radiation loss is negligible, as the difference between the full numerical solution and the modulation theory without radiation loss is minimal [60]. Over longer propagation distances $z > 100$, there is a noticeable amount of damping in the amplitude of the full numerical solution. However, if the radiation loss is taken into account the modulation solution undergoes damping and compares favourably with the full numerical solution.

The director angle is also represented by an ansatz that is chosen by a similar process to that for the nematicon. As there are no known solutions of the director equation (2.21), a trial function similar in form to the electric field envelope of the optical beam is used. That is, the director angle trial function in polar form is given by

$$\theta = \alpha \, \mathrm{sech}^2 \left(\frac{r}{\beta} \right), \tag{2.25}$$

where α is the amplitude and β is the width of the director angle and both are functions of z.

The trial function for the electric field envelope E (2.24) and the director rotation θ (2.25) are now substituted into the Lagrangian (2.22), which is then averaged by integrating in r from 0 to ∞.

In the local limit, $\nu \to 0$, the widths of the nematicon w and the director β are equal, $\beta = w$, and the calculation of the averaged Lagrangian is greatly simplified [74]. However, in the limit of current interest, the nonlocal limit with ν large, the widths are different $\beta \neq w$. Indeed in the nonlocal limit $\beta \gg w$. The integrals that involve the cross terms of θ and E in the averaged Lagrangian then cannot be evaluated explicitly. To enable approximations to these integrals to be evaluated, the method of equivalent functions is used [72].

Consequently, the averaged Lagrangian for a nematicon in the nonlocal limit is

$$\begin{aligned}\mathcal{L} = &-2\left(a^2w^2I_2 + \Lambda g^2\right)\sigma' - 2I_1aw^2g' + 2I_1gw^2a' + 4I_1awgw' \\ &- a^2I_{22} - 4\nu I_{42}\alpha^2 - 2qI_4\alpha^2\beta^2 + \frac{2A^2B^2\alpha a^2\beta^2w^2}{A^2\beta^2 + B^2w^2}. \qquad (2.26)\end{aligned}$$

The I's are various constants given by integrals and A and B are constants that are obtained using equivalent functions [72] and are stated in Appendix A. The area of the radiation shelf that accumulates under the evolving nematicon is modulo 2π, $\Lambda = \frac{1}{2}\ell^2$, where ℓ is the shelf radius, which needs to be determined.

Using the Euler–Lagrange equation (2.18), variations of the averaged Lagrangian with respect to the nematicon parameters generates a system of N first-order nonlinear ODEs of the form, a dynamical system,

$$\frac{d}{dz}\left(I_2a^2w^2 + \Lambda g^2\right) = 0, \qquad (2.27)$$

$$\frac{d}{dz}\left(I_1aw^2\right) = \Lambda g\sigma', \qquad (2.28)$$

$$I_1 \frac{dg}{dz} = \frac{I_{22} a}{2w^2} - \frac{A^2 B^4 \alpha a w^2 \beta^2}{\left(A^2\beta^2 + B^2 w^2\right)^2}, \tag{2.29}$$

$$I_2 \frac{d\sigma}{dz} = -\frac{I_{22}}{w^2} + \frac{A^2 B^2 \alpha \beta^2 \left(A^2\beta^2 + 2B^2 w^2\right)}{\left(A^2\beta^2 + B^2 w^2\right)^2}, \tag{2.30}$$

along with the algebraic equations

$$\alpha = \frac{A^2 B^2 \beta^2 w^2 a^2}{2\left(A^2\beta^2 + B^2 w^2\right)\left(2\nu I_{42} + q I_4 \beta^2\right)}, \tag{2.31}$$

$$\alpha = \frac{A^2 B^4 w^4 a^2}{q I_4 \left(A^2\beta^2 + B^2 w^2\right)^2}. \tag{2.32}$$

The system of equations (2.27)–(2.30) are called the modulation equations and are solved to find the evolution of the nematicon parameters with respect to the propagation length z.

Once the nematicon has ceased shedding radiation, it reaches its steady state. This means a relationship between the steady amplitude $\hat{a}$ and the steady width $\hat{w}$ can be found using equation (2.29) with $\hat{g} = 0$, yielding

$$\hat{a}^2 = \frac{I_{22}\left(A^2\hat{\beta}^2 + B^2\hat{w}^2\right)\left(2\nu I_{42} + q I_4 \hat{\beta}^2\right)}{A^2 B^6 \hat{\beta}^4 \hat{w}^6}, \tag{2.33}$$

where the carat ˆ denotes the steady state values or fixed points.

The following procedure is adopted to determine the shelf radius ℓ. The modulation equations (2.27)–(2.30) are linearised using perturbations about the fixed points for the amplitude a, width w and shelf height g. That is,

$$a = \hat{a} + a_1, \quad w = \hat{w} + w_1 \quad \text{and} \quad g = \hat{g} + g_1 = g_1, \tag{2.34}$$

where a_1, w_1 and g_1 are the first order perturbations of $\hat{a}$, $\hat{w}$ and $\hat{g}$. Linearised modulation equations are obtained by substitution of (2.34) into equations (2.27)–(2.30). The perturbation of the shelf amplitude g_1 is found to be given by the simple harmonic oscillator equation

$$\frac{d^2 g_1}{dz^2} - \frac{Q\Lambda\hat{\sigma}'}{I_1^2\left(\hat{w}^2 + 2\hat{a}\hat{w}\Theta\right)} g_1 = 0. \tag{2.35}$$

By matching the oscillation frequency $\hat{\sigma}$ of the steady nematicon (using equation (2.30) at the fixed point) to the frequency of the oscillator equation, the area of the low wavenumber diffractive radiation shelf is found to be

$$\Lambda = \frac{1}{2}\ell^2 = -\frac{\hat{\sigma}' I_1^2\left(\hat{w}^2 + 2\hat{a}\hat{w}\Theta\right)}{Q} \tag{2.36}$$

where Θ and Q [72] are stated in Appendix A.

Now the nonlocal interaction between the director and the beam extends the radiation shelf [72]. This is due to the director response to the beam having a longer tail, a result caused by the large value of ν. This in turn forces the electric field E to have a longer extension of the radiation tail, with the radiation shed from the edge of the extended tail. Hence, in the nonlocal regime the shelf of diffractive radiation is made up of two components. There is an inner portion of the shelf related to the radius ℓ defined by (2.36) on the region $0 \leq r \leq \ell$. This inner portion of the shelf is due to the resonant interaction of the zero wavenumber diffractive radiation with the light beam. The outer portion of the shelf is due to the nonlocal forcing of the optical axis, and has a radius ρ [60, 72, 73]. The outer shelf radius ρ

is related to the half-width of the optical disturbance of width β, that is, $\beta_{1/2} = \operatorname{sech}^{-1}(1/\sqrt{2})\beta$. Therefore, the outer shelf area is given by (modulo 2π)

$$\tilde{\Lambda} = \frac{1}{2}\rho^2 \tag{2.37}$$

an analogy with the inner shelf (2.36). Comparison with numerical solutions gives $\rho = 7\beta_{1/2}$ [72], which is robust for different initial conditions. Hence, the modulation equations (2.27)–(2.30) along with the shelf lengths (2.36) and (2.37), form a complete system of evolution equations for a nematicon. However, losses due to shed diffractive radiation have not been accounted for. Before the radiation loss is added to the modulation equations, a summary of the major details that will reappear throughout the remaining chapters will be presented. If and when there are differences, these details will be noted within the relevant sections. The points below are universal to the analytical technique used to study the evolution of optical beams and consist of

- the derivation of dynamical equations that model the particular governing equations of interest accurately and
- the choice of a trial function whose parameters vary independently and realistically with the propagation distance.

In addition to these points, there are several key details common to the variational method for determining the evolution of a nematicon

- the trial function for the beam envelope takes the form of a sech profile, plus an extra term which factors in the accumulation of the radiation under the nematicon,
- the amplitude of the shelf is small compared to that of the beam, $|g| \ll a$;
- the nematicon solutions will oscillate about a fixed point, which is a centre; and
- the evolution of the nematicon towards the steady state requires damping in the form of shed diffractive radiation.

The calculation and a discussion of the radiative loss are dealt with in the next section.

2.3.4 Radiative losses and a simple nematicon system

As for our example in section 2.3.3, the radiation loss is calculated using the governing equation (2.20) for the electric field envelope.

The shed diffractive radiation has small amplitude compared to the nematicon. Hence it is governed by the linearised equation (2.20), which is the Schrödinger equation

$$i\frac{\partial E}{\partial z} + \frac{1}{2r}\frac{\partial}{\partial r}\left(r\frac{\partial E}{\partial r}\right) = 0. \tag{2.38}$$

The boundary condition for the linearised NLS equation (2.38) requires that the shed radiation be matched to the shelf formed under the nematicon, that is, $E = S(z)$ at $r = \ell$. Now, the major contribution of this shed radiation is via mass shed from the nematicon as it evolves to the steady state. Using the mass density $\rho = |E|^2$ and the mass flux density $J = \frac{i}{2}\left(EE_r^* - E^*E_r\right)$, the mass conservation equation is

$$\frac{\partial \rho}{\partial z} + \frac{1}{r}\frac{\partial}{\partial r}\Big(rJ\Big) = i\frac{\partial}{\partial z}\left(r|E|^2\right) + \frac{1}{2}\frac{\partial}{\partial r}\left(rEE_r^* - rE^*E_r\right) = 0. \tag{2.39}$$

The mass flux transferring into dispersive radiation to the right of the nematicon from the evolving nematicon can be determined by integrating equation (2.39) from the edge of the shelf $r = \ell$ to $r = \infty$ and is given by

$$\frac{d}{dz}\int_{\ell}^{\infty} r|E|^2\,dr = \mathbf{Im}\left(rE^*E_r\right)\Big|_{r=\ell} + O\left[\dot{\ell}(z)\right]. \tag{2.40}$$

For the mass loss equation (2.40) to be useful, a relationship between E_r and E at the edge of the shelf $r = \ell$ needs to be established and the boundary condition $S(z)$ requires to be determined in terms of the nematicon parameters. The boundary condition $S(z)$, in terms of the nematicon parameters, is found by looking within the vicinity of the disk $r \leq \ell$. The trial function for the electric field envelope can be decomposed into the fixed-point solution $\hat{E}$ plus a component E_1 that must eventually be radiated away

$$E = \hat{E} + E_1, \tag{2.41}$$

where E_1 is the radiated component and $|E_1| \ll |\hat{E}|$.

The mass conservation equation (2.39) indicates that the mass density decomposes as

$$\int_0^{\ell(z)} |E|^2 r\, dr = \int_0^{\ell(z)} \left[|\hat{E}|^2 + 2\mathrm{Re}\left(\hat{E}E_1\right) + |E_1|^2\right] r\, dr. \tag{2.42}$$

Assuming that a small overlap exists between $\hat{E}$ and E_1, we have

$$I_2 a^2 w^2 + \Lambda g^2 = I_2 \hat{a}^2 \hat{w}^2 + \Lambda |E_1|^2\big|_{r=\ell}\,. \tag{2.43}$$

The total mass is given by the mass variational equation (2.27) as

$$I_2 a^2 w^2 + \Lambda g^2 \tag{2.44}$$

Setting $|E_1|\big|_{r=\ell} = S(z)$, equation (2.43) leads to the approximation involving mass conservation to give $S(z)$ as

$$|S(z)|^2 = \frac{1}{\Lambda}\left[I_2 a^2 w^2 - I_2 \hat{a}^2 \hat{w}^2 + \Lambda g^2\right]. \tag{2.45}$$

In order to calculate the mass flux (2.40) one final quantity, $\mathbf{Im}\,(rE^* E_r)$, needs to be determined. To evaluate this, the linearised NLS equation (2.38) together with the boundary condition $E = S(z)$ on $r = \ell$ needs to be solved. As the shelf radius ℓ is slowly varying, it may be treated as a constant throughout the following calculation.

The linearised NLS equation (2.38) is solved using Laplace transforms

$$\bar{E}(r,s) = \mathscr{L}\left\{E(r,z)\right\} = \int_0^{\infty} e^{-sz} E\, dz. \tag{2.46}$$

On taking Laplace transforms equation (2.38) becomes

$$is\bar{E} + \frac{1}{2r}\frac{\partial}{\partial r}\left(r\frac{\partial \bar{E}}{\partial r}\right) = 0, \tag{2.47}$$

where s is the Laplace transform variable. By making the substitution $r = \alpha w$, this transform equation can be set in terms of the modified Bessel's equation of order zero

$$w\bar{E}_{ww} + \bar{E}_w - w\bar{E} = 0, \tag{2.48}$$

which has the solution

$$\bar{E} = AK_0[w] = AK_0\left[\sqrt{2s}re^{-i\pi/4}\right], \tag{2.49}$$

where K_0 is the modified Bessel's function of order 0. We are interested in finding E_r. Taking the derivative of $\bar{E}$ with respect to r we obtain

$$\bar{E}_r = -A\sqrt{2s}e^{-i\pi/4}K_1\left[\sqrt{2s}re^{-i\pi/4}\right], \tag{2.50}$$

where K_1 is the modified Bessel's function of order 1. Rearranging equation (2.49) to find A and substituting it into equation (2.50), the Laplace transform (2.50) can be inverted using convolution theorem to give

$$E_r|_{r=\ell} = -\frac{1}{2\pi i}\int_C \sqrt{2s}e^{-i\pi/4}\frac{K_1\left[\sqrt{2s}e^{-i\pi/4}\ell\right]}{K_0\left[\sqrt{2s}e^{-i\pi/4}\ell\right]}\bar{E}_0 e^{sz}\,ds. \tag{2.51}$$

Here E_0 is the boundary condition for E at $r = \ell$ and the integral is over the usual inversion contour C for Laplace transforms. The required flux product for the mass loss integral (2.40) is then of the form

$$E^*E_r = S(z)^*\int_0^z G(z-z')E_0(z')\,dz', \tag{2.52}$$

since $E = S$ at $r = \ell$. The Green's function G is

$$G(\chi) = -\frac{1}{2\pi i}\int_C \sqrt{2s}e^{-i\pi/4}\frac{K_1\left[\sqrt{2s}e^{-i\pi/4}\ell\right]}{K_0\left[\sqrt{2s}e^{-i\pi/4}\ell\right]}e^{s\chi}\,ds, \tag{2.53}$$

where $\chi = z - z'$. By writing S in polar form

$$S(z) = R(z)e^{i\phi(z)}, \tag{2.54}$$

and assuming that the phase ϕ is slowly varying, the flux product can be simplified to

$$E^* E_r = R(z) \int_0^z G(z - z')R(z')\, dz'. \tag{2.55}$$

Equation (2.54) gives that $|R| = |S|$ and the radiation flux is thus determined by calculating the Green's function G. The Green's function in its current form is not suitable, so a useful approximation will now be derived. To calculate G, the integrand in equation (2.53) can be rearranged in the form

$$-\frac{2s}{\ell}\frac{d}{ds}\log\left\{K_0\left[\sqrt{2s}e^{-i\pi/4}\ell\right]\right\}. \tag{2.56}$$

The shed radiation accumulates under the nematicon over a long propagation length. As a result, we are interested in the behaviour of the radiation flux for large z. Thus the above expression (2.56) can be expanded for $s \to 0$ using the asymptotic expansion [75]

$$K_0(z) \sim -\log\left(\frac{z}{2}\right) \quad \text{as } z \to 0. \tag{2.57}$$

When $s \to 0$ the integrand in equation (2.53) can be approximated by

$$-\frac{1}{\ell}\frac{2}{\log s + \log\Lambda - \frac{i\pi}{2}}, \tag{2.58}$$

where $\Lambda = \ell^2/2$. Hence, the Green's function (2.53) becomes

$$G(\chi) = \frac{1}{2\pi i\ell}\int_C \frac{2e^{s\chi}}{\log s + \log\Lambda - \frac{i\pi}{2}}\, ds. \tag{2.59}$$

To evaluate the integral (2.59) the contour C must be deformed around the branch cut due to $\log s$ on the whole of the negative real line. The deformation results in the Green's function integral becoming

$$G(\chi) = \frac{1}{2\ell}\int_{-\infty}^{\infty} \frac{e^{-e^{\mu}\chi+\mu}}{\left(\frac{\mu}{2}+\frac{\log\Lambda}{2}\right)^2 - \frac{i\pi}{2}\left(\frac{\mu}{2}+\frac{\log\Lambda}{2}\right)+\frac{3\pi^2}{16}}\, d\mu. \tag{2.60}$$

The Green's function is now in a form that allows the use of the method of stationary phase for large z. We rewrite the integral (2.60) as

$$2\ell G(\chi) = \int_{-\infty}^{\infty} g(\mu) e^{f(\mu)}\, d\mu, \tag{2.61}$$

where

$$f(\mu) = -e^{\mu}\chi + \mu, \text{ and} \tag{2.62}$$

$$g(\mu) = \left[\left(\frac{\mu}{2}+\frac{\log\Lambda}{2}\right)^2 - \frac{i\pi}{2}\left(\frac{\mu}{2}+\frac{\log\Lambda}{2}\right)+\frac{3\pi^2}{16}\right]^{-1}. \tag{2.63}$$

The advantage of the method of stationary phase is that upon evaluation of the integral, only the dominant contribution is asymptotically important. This means that only the highest stationary point of $f(\mu)$ will offer the major contribution, which turns out to be a saddle point as we are working in the complex plane. The result is derived from the Taylor series expansion of $f(\mu)$ about the point μ_0, where μ_0 is chosen such that $df/d\mu_0 = 0$, that is, the stationary point. It is found that $\mu_0 = -\log\chi$. The method of stationary phase then gives

$$2\ell G(\chi) \approx g(\mu_0) e^{f(\mu_0)} \left(\frac{2\pi}{|d^2 f(\mu_0)/d\mu^2|}\right)^{1/2}. \tag{2.64}$$

Substitution of μ_0 into equation (2.64) reveals the approximate solution for the Green's function to be

$$2\ell G(\chi) = \frac{\sqrt{2\pi}}{e\chi\left(\left(\frac{1}{2}\log\frac{\chi}{\Lambda}+\frac{i\pi}{4}\right)^2+\frac{\pi^2}{4}\right)}. \tag{2.65}$$

The Green's function (2.65) can now be substituted into the flux term (2.55) to give

$$E_r = \frac{\sqrt{2\pi}}{2\ell e}\int_0^z \frac{R(z')}{\left\{\left(\frac{1}{2}\log\left(\frac{z-z'}{\Lambda}\right)+\frac{i\pi}{4}\right)^2+\frac{\pi^2}{4}\right\}}\frac{dz'}{(z-z')}. \tag{2.66}$$

Mass conservation then shows that the mass flux to radiation result (2.40) gives mass conservation for the nematicon as

$$\begin{aligned}\frac{d}{dz}\left(a^2w^2I_2+\Lambda g^2\right) &= \frac{d}{dz}\int_\ell^\infty r|E|^2\,dr \qquad (2.67)\\ &= -\,\mathbf{Im}\left\{\frac{\sqrt{2\pi}R(z)}{2e}\int_0^z\frac{R(z')}{\left\{\left(\frac{1}{2}\log\left(\frac{z-z'}{\Lambda}\right)+\frac{i\pi}{4}\right)^2+\frac{\pi^2}{4}\right\}}\right\}\frac{dz'}{(z-z')}\end{aligned}$$

Finally, to complete the calculation the height of the shelf of radiation $R(z)$ needs to be calculated. This is done by equating the area of the shelf to the difference in mass between the solution at z and the fixed point solitary wave, so that

$$|R(z)|^2\Lambda = (I_2a^2w^2 - I_2\hat{a}^2\hat{w}^2+\Lambda g^2). \tag{2.68}$$

Incorporating the mass loss into the modulation equation for g, equation (2.29) in its final form becomes the modified modulation equation

$$I_1\frac{dg}{dz} = \frac{I_{22}a}{2w^2}-\frac{I_4a^3}{q}+\frac{3I_8a^7}{q^3}-2\delta g, \tag{2.69}$$

where δ is the loss coefficient. The conservation of mass equation (2.67) is

$$\frac{d}{dz}\left(a^2w^2I_2\right) + 2\Lambda g\frac{dg}{dz} = -\mathbf{Im}\left\{\ell RE_r|_{r=\ell}\right\}. \tag{2.70}$$

Further, at the fixed point it is assumed that the radiation loss term is the major contributor from equation (2.69)

$$\frac{dg}{dz} \sim -\frac{2\delta g}{I_1}, \tag{2.71}$$

so that equation (2.70) yields

$$-\frac{4\Lambda\delta g^2}{I_1} = -\frac{4\Lambda\delta R^2}{I_1} = -\mathbf{Im}\left\{\ell RE_r|_{r=\ell}\right\}. \tag{2.72}$$

The loss coefficient δ is then

$$\delta = \frac{\mathbf{Im}\left\{\ell RE_r|_{r=\ell}\right\} I_1}{4\Lambda R^2}. \tag{2.73}$$

After evaluating the imaginary part of the integral for E_r from (2.66), the final form of the loss coefficient δ is

$$\begin{aligned}\delta = &-\frac{\pi\sqrt{2\pi}I_1}{32eR(z)\Lambda} \\ &\times \int_0^z \frac{R(z')\log\left(\frac{z-z'}{\Lambda}\right)}{\left[\left(\left\{\frac{1}{2}\log\left(\frac{z-z'}{\Lambda}\right)\right\}^2 + \frac{3\pi^2}{16}\right)^2 + \frac{\pi^2}{16}\left\{\log\left(\frac{z-z'}{\Lambda}\right)\right\}^2\right]}\frac{dz'}{(z-z')}\end{aligned} \tag{2.74}$$

It should be noted that a minor bracketing error occurred in the term $\left(\left\{\frac{1}{2}\log\left(\frac{z-z'}{\Lambda}\right)\right\}^2 + \frac{3\pi^2}{16}\right)^2$ for δ in reference [72], which has been corrected in this thesis. This expression for δ, along with the modulation equations (2.27), (2.28) and (2.30) with the extended equation (2.69) form a complete set of modulation equations approximating a single nematicon's evolution in the nonlocal regime of a NLC.

Before continuing, it is worth noting that the radiation calculation presented here is identical for all the work presented in Chapters 3, 4 and 5. Where there are differences, these will be discussed in the respective chapter.

The numerical technique used to solve the modulation equations is the subject of the next section.

2.3.5 Solving the modulation equations

In section 2.3.3 a system of first order nonlinear ODEs, known as modulation or variational equations, were obtained using approximate methods to analytically solve the governing equations (2.20) and (2.21) for optical beams in NLC. This system of equations (2.27), (2.28), (2.30) along with (2.69), needs to be solved numerically. The modulation equations can be solved using the standard fourth-order Runge–Kutta method (RK4), for instance.

The modulation equations as they are currently expressed form a nonlinear system of first order ODEs in terms of the nematicon parameters present in the trial functions (2.24) and (2.25) for the electric field envelope and nematic response, respectively.

In order to use the fourth order Runge–Kutta scheme (RK4) to determine the solution of the system of ODEs, the modulation equations need to be expressed in the form of an initial value problem (IVP) as

$$\underset{\sim}{\mathbf{x}}'(z) = \underset{\sim}{\Phi}(z, \underset{\sim}{\mathbf{x}}), \quad \underset{\sim}{\mathbf{x}}(z_0) = \underset{\sim}{\mathbf{x}_{\mathbf{0}}}, \tag{2.75}$$

where $\underset{\sim}{\mathbf{x}} = (x_1, x_2, \ldots, x_N)^T$, N is the number of nematicon parameters.

The current modulation equations (2.27)–(2.30) and (2.69) are of the form

$$A\underset{\sim}{\mathbf{x}}' = \underset{\sim}{\mathbf{b}}, \tag{2.76}$$

where A is the matrix of coefficients of $\underset{\sim}{\mathbf{x}}'$ and $\underset{\sim}{\mathbf{b}} = (b_1, b_2, \ldots, b_n)^T$ is the right hand sides of the system of ODEs. A is initially given by the initial nematicon parameter values. Provided that $\det A \neq 0$, then the matrix A can be decomposed into lower, L, and upper, U, triangular matrices via an LU decomposition. That is, equation (2.76) can be written as

$$LU\underset{\sim}{\mathbf{x}}' = \underset{\sim}{\mathbf{b}}. \tag{2.77}$$

Pre-multiplying by L^{-1} both sides of equation (2.77) leads to

$$U\underset{\sim}{\mathbf{x}}' = L^{-1}\underset{\sim}{\mathbf{b}}. \tag{2.78}$$

If we let

$$\underset{\sim}{\mathbf{y}} = L^{-1}\underset{\sim}{\mathbf{b}} \tag{2.79}$$

then equation (2.76) becomes a coupled system of equations of the form

$$L\underset{\sim}{\mathbf{y}} = \underset{\sim}{\mathbf{b}} \tag{2.80}$$

$$U\underset{\sim}{\mathbf{x}}' = \underset{\sim}{\mathbf{y}}, \tag{2.81}$$

where $\underset{\sim}{\mathbf{y}}$ and $\underset{\sim}{\mathbf{x}}'$ are obtained through the usual numerical forward and backward substitution techniques, respectively.

It should be noted that equation (2.75) could have been obtained by evaluating

$$\underset{\sim}{\mathbf{x}}' = A^{-1}\underset{\sim}{\mathbf{b}}, \tag{2.82}$$

where $\underset{\sim}{\boldsymbol{\Phi}}(z, \underset{\sim}{\mathbf{x}}) = A^{-1}\underset{\sim}{\mathbf{b}}$. However, the process of factorising the matrix A using an LU decomposition increases the efficiency of calculating the solution by a factor of three over the inversion of A.

In equations (2.80) and (2.81), each b_i and y_i for the N nematicon parameters is easily solved. This procedure has the advantage over Gaussian elimination, as the computation of $\underset{\sim}{\mathbf{x}}'$ for each b_i would slow down the process as the elimination process would need to be performed N times [76].

The system of ODEs written as an IVP in equation (2.75) can now be solved for $\underset{\sim}{\mathbf{x}}$ using RK4, where the ith component is given by

$$\underset{\sim}{\mathbf{x}}_{i+1} = \underset{\sim}{\mathbf{x}}_i + \frac{1}{6}\left(\underset{\sim}{\mathbf{k}}_1 + 2\underset{\sim}{\mathbf{k}}_2 + 2\underset{\sim}{\mathbf{k}}_3 + \underset{\sim}{\mathbf{k}}_4\right), \tag{2.83}$$

$$z_{i+1} = z_i + h. \tag{2.84}$$

Here $i = 1, 2, \ldots, N$, $\underset{\sim}{\mathbf{x}}_i$ is the vector of nematicon parameters at the position z_i within the cell after i steps, and $\underset{\sim}{\mathbf{x}}_{i+1}$ are the values of the nematicon parameters at the next propagation distance z_{i+1}. The estimates of the slopes $\underset{\sim}{\mathbf{k}}_j$ $(j = 1, \ldots, 4)$ are

$$\underset{\sim}{\mathbf{k}}_1 = \underset{\sim}{\mathbf{\Phi}}\left(z_i, \underset{\sim}{\mathbf{x}}_i\right), \tag{2.85}$$

$$\underset{\sim}{\mathbf{k}}_2 = \underset{\sim}{\mathbf{\Phi}}\left(z_i + \frac{h}{2}, \underset{\sim}{\mathbf{x}}_i + \frac{h}{2}\underset{\sim}{\mathbf{k}}_1\right), \tag{2.86}$$

$$\underset{\sim}{\mathbf{k}}_3 = \underset{\sim}{\mathbf{\Phi}}\left(z_i + \frac{h}{2}, \underset{\sim}{\mathbf{x}}_i + \frac{h}{2}\underset{\sim}{\mathbf{k}}_2\right), \tag{2.87}$$

$$\underset{\sim}{\mathbf{k}}_4 = \underset{\sim}{\mathbf{\Phi}}\left(z_i + h, \underset{\sim}{\mathbf{x}}_i + h\underset{\sim}{\mathbf{k}}_3\right). \tag{2.88}$$

The system (2.76) is now solved to fourth order accuracy.

Prior to solving the system of equations (2.76), diffractive radiation loss (derived in Section 2.3.4) needs to be included, as the loss allows the nematicon to approach its steady state. In the next section, a method will be developed to numerically account for the radiation loss.

Section 2.3.6 now describes how the diffractive radiation loss is numerically calculated.

2.3.6 Numerical calculation of radiation

It was discussed in section 2.3.4 that the inclusion of diffractive radiation loss allows the nematicon to approach its steady state as z becomes large. This radiation loss term was derived from the linearised NLS equation (2.38) and determined as equation (2.74). This loss coefficient can be rewritten in the following form

$$\delta = -\frac{\pi\sqrt{2\pi}I_1}{32eR(z)\Lambda}\int_0^z \frac{g(z')}{(z - z')}\,dz', \tag{2.89}$$

where

$$g\left(z'\right) = \frac{R\left(z'\right)\ln\left[\frac{(z-z')}{\Lambda}\right]}{\left(\left(\left\{\frac{1}{2}\ln\left[\frac{(z-z')}{\Lambda}\right]\right\}^2 + \frac{3\pi^2}{16}\right)^2 + \frac{\pi^2}{16}\left\{\ln\left[\frac{(z-z')}{\Lambda}\right]\right\}^2\right)}. \tag{2.90}$$

It is easily seen that equation (2.89) has a singularity at the upper limit of the integral at $z' = z$, complicating the evaluation of the integral. Miksis and Ting [77] developed a general numerical method to deal with similar singular integrals involved in integro-differential equations. The numerical method requires the region of integration ($0 \leq z' \leq z$) to be split into two separate regions. Thus, the region of integration is separated into a region without the singularity ($0 \leq z' \leq M$) and a region containing the singularity ($M < z' \leq z$), where $M \in [0, z]$. That is, the integral in equation (2.89) can be written as

$$\begin{aligned}\int_0^z \frac{g(z')}{(z-z')^\kappa}\,dz' &= \int_0^M \frac{g(z')}{(z-z')^\kappa}\,dz' + \int_M^z \frac{g(z')}{(z-z')^\kappa}\,dz' \\ &= \Psi_1 + \Psi_2, \end{aligned} \tag{2.91}$$

where g is non-singular. The integral is divergent if $\kappa \geq 1$. The value of M is chosen carefully, so that it is sufficiently far from the singularity $z' = z$, and also, ensures Ψ_1 will be smooth.

García-Reimbert [74] modified the original method of Miksis and Ting [77] to allow the denominator of equation (2.89) to be approximated by a leading order singularity as $z' \to z$. Note for our case that $\kappa = 1$ in the denominator of equation (2.91). This means that the integral in equation (2.89) could be divergent. However, as $z \to z'$ in (2.90) the logarithms, give that the integral still converges. A careful analysis of the singularity near $z = z'$ taking account of the logarithms in the denominator shows that the singularity is integrable.

Ψ_1 can be numerically integrated using a standard technique, such as the trapezoidal rule.

The integral Ψ_2 containing the singularity then remains to be considered. Ψ_2 is singular at the upper limit $z' = z$ and for this reason the integral is expressed as the sum of integrals, such that

$$\Psi_2 = \sum_{j=k}^{m} \int_{z_j}^{z_{j+1}} \frac{g(z')}{(z - z')} \, dz', \tag{2.92}$$

where z_k is chosen so that $z_k = M$ and $z_{m+1} = z$.

Hence, the singularity that appears in the region of integration $[0, z]$ is dealt with by splitting the region into two distinct regions, Ψ_1 and Ψ_2. The singular part is integrated exactly with g set as $g(z_j)$ within each term.

2.4 Full numerical scheme

The modulation analysis in the preceding sections was in relation to the propagation of a $(2+1)$D nematicon in an infinite plane NLC cell. The reason for this was to develop an understanding of the basic arguments used to construct semi-analytical solutions for the propagation of light beams in soft matter, followed by a simple example to give full details in the simplest case. In this section, discussion will centre on deriving a full numerical scheme for beam propagation in a finite NLC cell . The main reasons for shifting the focus are

- this thesis concentrates on the propagation of a nematicon in a finite NLC cell;
- the numerical scheme for a finite NLC cell is different to that for an infinite NLC cell used in [72], which was a pseudo-spectral method. Hence, it is left to the reader to refer to the paper by Fornberg and Whitham [78] that describes the basic numerical scheme used in this work.

The approximate method used to solve the governing equations has been developed in Section 2.3. In this section the full numerical scheme for the coupled system of PDEs (2.14) and (2.16) that govern the propagation of a light beam in a finite NLC cell will be described.

The non-dimensional governing equations are

$$iE_z + \nabla^2 E + 2\theta E = 0, \tag{2.93}$$

$$\nu \nabla^2 \theta + 2|E|^2 = 0. \tag{2.94}$$

The boundaries that enclose the region of interest are a closed rectangle with dimensions $0 \leq x \leq L_x$ and $0 \leq y \leq L_y$, as shown in figure 2.1. This rectangle resembles a typical non-dimensional finite sized NLC cell in the $x-y$ cross-section. On all four of the boundaries the director is anchored, so

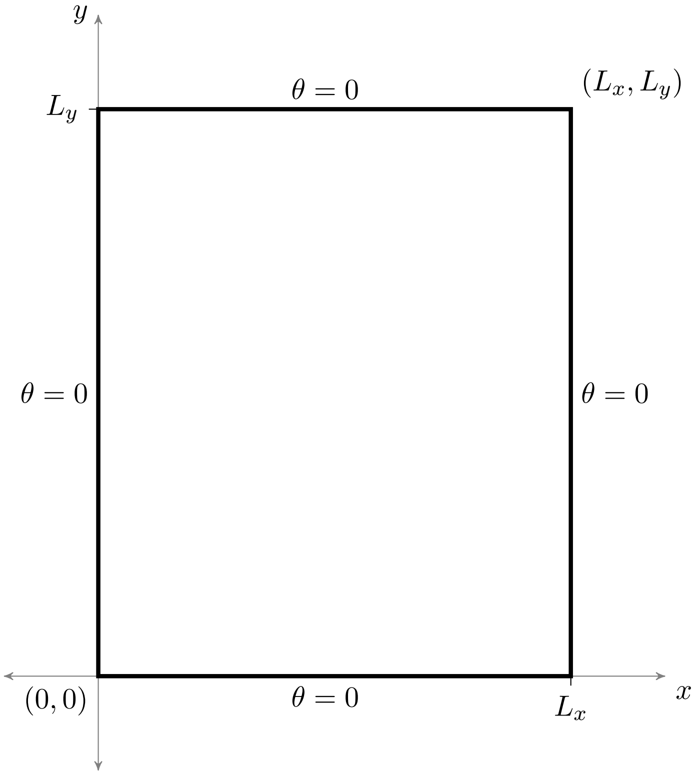

Figure 2.1: Diagram of the NLC cell in the $x-y$ plane with the propagation direction z going into the page. The NLC cell is bounded by $0 \leq x \leq L_x$ and $0 \leq y \leq L_y$. The director is anchored at zero on the four walls of the cell, $\theta = 0$ at $x = 0, L_x$ and $y = 0, L_y$.

that the director perturbation angle $\theta = 0$. That is, $\theta = 0$ on $x = 0, L_x$ and $y = 0, L_y$ for all z (see figure 2.1). For numerical purposes, we represent the continuous $x - y$ plane of the NLC cell as an uniformly spaced discretised $m \times n$ grid, where $m = 0, 1, \ldots, M$ and $n = 0, 1, \ldots, N$. The uniform spacing between each of the grip points is given by Δx and Δy (see figure 2.2) in the x and y directions, respectively. The final grid points are chosen so that

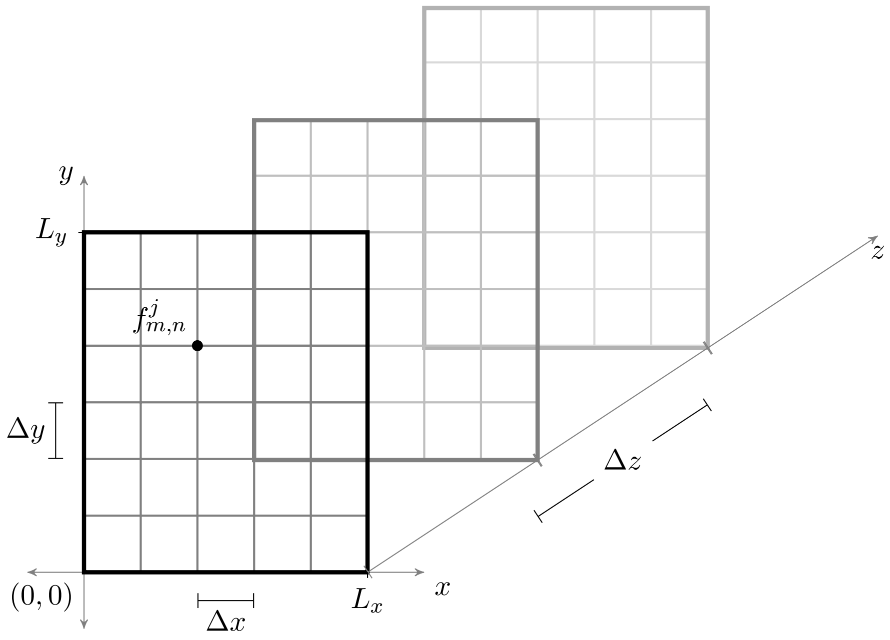

Figure 2.2: Diagram of the discretised NLC cell. The x, y and z axes have uniformly spaced step sizes Δx, Δy and Δz, respectively. The point $f^j_{m,n}$ represents the point $f(x_m, y_n, z_j)$ on the grid.

$M\Delta x = L_x$ and $N\Delta y = L_y$.

Further, the light beam is propagating through a NLC cell in the z (time-like) direction, which is also discretised by uniform grid spacing Δz (see figure 2.2). Numerically, j will represent the discretised propagation length $0 \leq j \leq J$, where the final propagation length is chosen so that $J\Delta z = z_f$. Hence, a function $f(x, y, z)$ can be represented on the discretised grid by the point $f(x_m, y_n, z_j)$, where each discrete set of points is written as

$$\begin{aligned} x_m &= x_0 + m\Delta x, \quad m = 0, 1, \ldots, M \\ y_n &= y_0 + n\Delta y, \quad n = 0, 1, \ldots, N \\ z_j &= z_0 + j\Delta z, \quad j = 0, 1, \ldots, J. \end{aligned} \tag{2.95}$$

From now on, we will write $f^j_{m,n}$ to represent $f(x_m, y_n, z_j)$.

To begin with, initial conditions are applied to the system. The director angle θ is uniformly set to equal zero over the $x - y$ plane, that is, $\theta^0_{m,n} = 0$. The electric field envelope for the light beam is the trial function (equation (2.17)) with $g = 0$, with the nematicon parameters chosen to be typical non-dimensional values for an input light beam, that is, $E^0_{m,n} = f(h_{1_{m,n}}(0), \ldots, h_{N_{n,m}}(0))$.

Let us now discretise equation (2.93) for the electric field envelope of the light beam using second-order centred differences for the Laplacian $\nabla^2 E$. The spatial step sizes are set to be equal, that is, $\Delta x = \Delta y$. The numerical solution for the next time step can then be calculated by

$$E^{j+1}_{m,n} = E^j_{m,n} + i\Delta z f^j_{m,n}, \tag{2.96}$$

where

$$f^j_{n,m} = u^j_{m,n} + v^j_{m,n} \tag{2.97}$$

$$u^j_{m,n} = \frac{E^j_{m+1,n} + E^j_{m-1,n} + E^j_{m,n+1} + E^j_{m,n-1} - 4E^j_{m,n}}{2(\Delta x)^2} \tag{2.98}$$

$$v^j_{m,n} = 2\theta^j_{m,n} E^j_{m,n}. \tag{2.99}$$

The accuracy of the numerical scheme in its current form can be improved by using a predictor-corrector method based on the second-order Runge–Kutta method. The method works by predicting the values of the electric field envelope at the $(j+1)$th z step. We will denote the predicted values by $P^j_{m,n}$, which are calculated using the equation in (2.96)

$$P^{j+1}_{m,n} = E^j_{m,n} + i\Delta z\left(u^j_{m,n} + v^j_{m,n}\right). \tag{2.100}$$

Now that we have predicted the solution at the next time step, we use these values to correct the linearisation of the derivative, given by f in equation (2.96). Let us denote the corrector by $C^j_{m,n}$. Then

$$C^{j+1}_{m,n} = E^j_{m,n} + \frac{i\Delta z}{2}\left(f^j_{m,n} + p^{j+1}_{m,n}\right), \tag{2.101}$$

where $p^{j+1}_{m,n}$ uses the predicted values from $P^{j+1}_{m,n}$ to calculate the slope, yielding

$$p^{j+1}_{m,n} = \frac{P^{j+1}_{m+1,n}P^{j+1}_{m-1,n} + P^{j+1}_{m,n+1} + P^{j+1}_{m,n-1} - 4P^{j+1}_{m,n}}{2(\Delta x)^2} + 2\theta^j_{m,n}P^{j+1}_{m,n}. \tag{2.102}$$

A more accurate solution of equation (2.93) has now been found, where the corrected value becomes the solution at the $(j+1)$th time step, that is, $C^{j+1}_{m,n} = E^{j+1}_{m,n}$. The error in this scheme is $O(\Delta x^2, \Delta z^2)$.

However, to be able to solve equation (2.93) at the next time-step z_{j+1}, the solution for the director angle at z_j needs to be determined. Again, using the standard second order centred differences for the Laplacian $\nabla^2\theta$, we can write the discretised boundary value problem (BVP), equation (2.94), as

$$\theta^j_{m,n} = \frac{\left(\theta^j_{m+1,n} + \theta^j_{m-1,n} + \theta^j_{m,n+1} + \theta^j_{m,n-1}\right)}{4} + \frac{(\Delta x)^2 |E^j_{m,n}|^2}{2\nu}, \qquad (2.103)$$

where the boundary conditions are $\theta_{0,n} = \theta_{M,n} = \theta_{m,0} = \theta_{m,N} = 0$ for all $j \in [0, J]$. To solve the above BVP, an iterative technique is employed with a convergence criteria used to determined when the solution reaches the required level of accuracy. Equation (2.103) is solved using Jacobi iteration, by which the four nearest neighbouring points on the grid (shown in figure 2.3), plus the source term, the last term on the right hand side of (2.103) are iterated until convergence. The convergence criteria requires that the difference between successive iterations be less than or equal to some ϵ, where $\epsilon \ll 1$, that is,

$$\max \left| \theta^j_{(m,n)_{k+1}} - \theta^j_{(m,n)_k} \right| \leq \epsilon \qquad (2.104)$$

where k is the number of iterations performed.

The combination of equations (2.101) and (2.103) give the full numerical solution for the nematicon governing equations (2.14) and (2.16) and act as a numerically accurate comparison for the solutions that will be derived in the next chapters using the semi-analytical methods outlined in this chapter.

Within this chapter we have addressed how a physical model of a light beam propagating through a NLC cell can evolve into a mathematical model consisting of a strongly coupled system of PDEs that can describe the non-

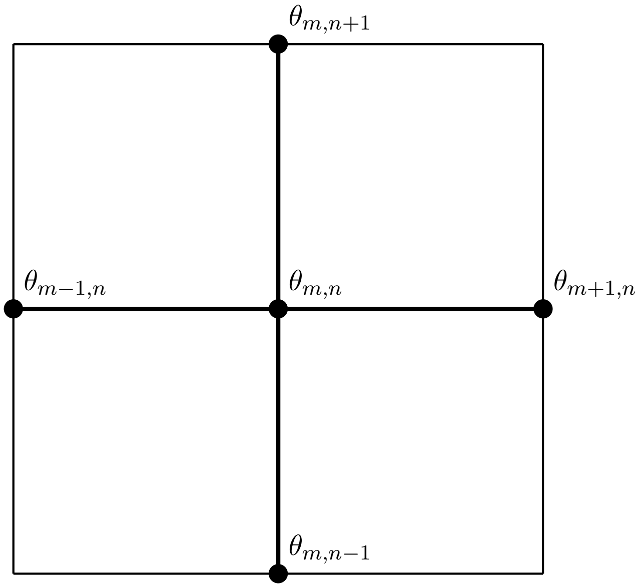

Figure 2.3: Shows the four nearest neighbours of the source term used to calculate the director angle $\theta_{m,n}$ numerically.

linear behaviour of such a light beam. As there is currently no known exact solitary wave solution for these governing equations, an approximate theory was developed to explore a semi-analytical method of solution. This approximate method involved using applications of modulation theory and conservation equations for a nematicon.

An illustration of this approximate method was achieved by using a $(2+1)$D nematicon as an example. This example gave insight and understanding of the theory. The approximate theory was further developed by the derivation of the effect of the diffractive radiation shed by the evolving nematicon. The importance of accounting for shed diffractive radiation in the model is that it allowed damping to settle the solution to its steady state.

The approximate method resulted in a system of N ODEs, where N is the number of nematicon parameters. This system of ODEs was solved using an LU decomposition and RK4 to gain fourth order accurate results. Finally, a full numerical solution was outlined, which gives an accurate comparison for the semi-analytical solution. This chapter represents the groundwork for the approximate and numerical methods used throughout the remaining Chapters 3, 4 and 5. These methods will be built upon in each case.

Chapter 3

Propagation of optical solitary waves in bias-free nematic liquid crystal cells.

3.1 Background

The field of nonlinear optics is no different to the any other field, where new advances in technology are constantly being sort to enhance the specialised effects presented by an optical medium. In nonlinear optics, this effect is the nonlinearity experienced by the input laser beam as it traverses through the nonlinear medium. It turns out that nematic liquid crystal (NLC), or nematic for short, is an ideal medium for the propagation of such input beams. The 'huge' nonlinearity displayed by the NLC means that the nonlinear effects can be observed over millimeter distances [28]. The nematic also offers the additional advantage of nonlocality whereby the effect of the light beam on the NLC extends far beyond the waist of the beam (see Chapter 1 for more details of an NLC's properties). The usual catastrophic collapse of a two-dimensional bulk solitary wave is then arrested by the nonlocal response of the nematic [29, 36, 50].

There have been many investigations into nonlocal nonlinear media, for which the driving force for self-focusing is the intensity-dependent change in the refractive index, which can balance the diffraction of the beam to form a self-trapped solitary wave in NLC, or a nematicon [29]. The mechanism that changes the refractive index of the NLC is the dipole moment that forms in the nematic molecules due to the interaction with the electric field of the beam, thus causing a rotation of the molecules and, in turn, a change in the refractive index [23]. Nematic liquid crystals have attracted interest due to their potential use in all-optical devices, such as logic gates [23, 29, 79].

The phenomenon, known as the Freédericksz threshold, requires a minimum beam power to overcome the inertia of the molecules to rotate and allow the beam to self-focus and thus form a nematicon. To reduce the need for using high power beams, which destroy the NLC, the molecules are pre-tilted, thus overcoming the threshold and allowing the propagation of low power (milliwatt) beams [29, 36]. There are two ways in which the molecular pre-tilt is achieved. The first is to apply an external static electric field in the polarisation direction x, perpendicular to the propagation direction z. This method has been well studied both experimentally [29, 62, 79, 80] and theoretically [15, 36, 81, 82]. The second technique to overcome the threshold is to "rub" the cell walls of the nematic so that the nematic molecules are pre-tilted at the walls. The elastic response of the NLC enables the pre-tilt at the cell walls to be propagated through the remaining bulk of the medium.

This chapter and the remainder of this thesis will only consider the rubbing pre-tilt method. The underlying physical difference between the two pre-tilt mechanisms is that, in the case of the application of the static external electric field, the director response decays exponentially away from the local area of the beam [30]. The typical ratio of the cell to beam width is $O(20)$. If the nematicon is then launched near the centre of the cell, the effect of the cell walls can be neglected. However, if the cell walls are "rubbed" to pre-tilt the nematic molecules, the molecular re-orientation behaves logarithmically, making the cell walls an integral part of the system [30].

The model presented here aims to include the repulsion due to the cell walls experienced by a nonlinear optical beam as it propagates through the NLC. Let us consider a coherent, linearly polarised light beam input into a planar liquid crystal cell, propagating in the z (pseudo-time) direction, with the $x-y$ plane orthogonal to the propagation direction. The direction of polarisation is the x direction. To allow the formation of nematicons [29] from milliwatt beam powers, the nematic molecules are pre-tilted, thus avoiding the diffraction of the beam and overcoming the Freédricksz threshold [23, 36]. The rubbing pre-tilts the nematic molecules by an angle θ_0 to the cell walls. The elastic response of the nematic is then responsible for the transmission of the pre-tilt angle throughout the bulk of the nematic. The pre-tilt angle θ_0 is made with the z direction in the $x-z$ plane. The introduction of the electric field of the light beam causes a further rotation θ of the nematic director. The total director angle is thus $\phi = \theta_0 + \theta$. The equations governing the propagation of a single light beam in NLC consist of a nonlinear Schrödinger-like (NLS-like) equation for the light beam's electric field and a director (Poisson) equation governing the perturbation of the nematic molecules from the pre-tilt angle. In non-dimensional form the governing equations are [30, 43, 44]

$$i\frac{\partial E}{\partial z} + \frac{1}{2}\nabla^2 E + E\sin 2\theta = 0, \tag{3.1}$$

$$\nu\nabla^2\theta + 2|E|^2\cos 2\theta = 0, \tag{3.2}$$

where the Laplacian ∇^2 is in the $x-y$ plane. The parameter ν is a measure of the elastic response of the nematic, and thus is a measure of the nonlocality, with large values corresponding to a nonlocal response. The variable E is the complex-valued slowly varying envelope of the electric field of the beam [36]. Typical values of ν are of $O(100)$ in experiments [26]. Also, experimentally a prominent effect known as walk-off occurs, whereby the beam trajectory follows the Poynting vector which is at an angle to the input wavevector. This effect has been eliminated from equation (3.1) with the use of a phase factor [40, 42] for constant walk-off. The phase factor is valid as the nematic has constant properties and so the walk-off is constant [42]. The full derivation of the nematicon governing equations can be found in Section 2.2.

3.2 Analysis

3.2.1 Nematicon governing equations

For milliwatt beam powers in the nonlocal limit (ν large), the small deviation angle approximation can be used. Hence, the perturbation angle of the nematic molecules θ from the pre-tilt angle θ_0 is small, $|\theta| \ll \theta_0$. For this small angle limit the nematicon governing equations (3.1) and (3.2) may be approximated by

$$i\frac{\partial E}{\partial z} + \frac{1}{2}\nabla^2 E + 2E\theta = 0, \tag{3.3}$$

$$\nu\nabla^2\theta + 2|E|^2 = 0. \tag{3.4}$$

We will consider a rectangular cell geometry and take the cell to lie within $0 \leq x \leq L_x$ and $0 \leq y \leq L_y$. In experimental studies of the effect of cell boundaries on nematicon propagation, typical dimensional values are a cell thickness of 75 μm with a beam waist of 3 μm for a 1.064 μm beam at a beam power of 3 mW [40]. Hence, a typical non-dimensional cell length is 25. The nematic molecules are fixed at the boundaries at the angle θ_0. Therefore, the appropriate boundary conditions for the perturbation angle θ are $\theta = 0$ on the four walls $x = 0, L_x$ and $y = 0, L_y$ (see figure 2.1).

As previously stated, the nematicon governing equations (3.3) and (3.4) have no known solitary wave solution at present. Using the methods outlined in Chapter 2 the coupled system of equations are written in terms of a Lagrangian as

$$L = i\left(E^* E_z - E E_z^*\right) - |\nabla E|^2 + 4\theta|E|^2 - \nu|\nabla\theta|^2. \tag{3.5}$$

Here, the superscript * denotes the complex conjugate.

To demonstrate that the Lagrangian (3.5) represents the nematicon governing equations (3.3) and (3.4), we take variations of the Lagrangian (3.5) with respect to both the electric field envelope E and the director angle θ. Consider the variation in E, that is,

$$\delta E: \quad \frac{\partial}{\partial z}\left(\frac{\partial L}{\partial E_z}\right) + \frac{\partial}{\partial x}\left(\frac{\partial L}{\partial E_x}\right) + \frac{\partial}{\partial y}\left(\frac{\partial L}{\partial E_y}\right) - \frac{\partial L}{\partial E} = 0. \tag{3.6}$$

Substituting equation (3.5) into equation (3.6) yields

$$2iE_z^* - E_{xx}^* - E_{yy}^* - 4\theta E^* = 0. \tag{3.7}$$

Then taking the complex conjugate of (3.7) results in the NLS-like governing equation (3.3). Similarly, taking variations of the Lagrangian with respect to the director angle θ, we have

$$\delta\theta : \quad \frac{\partial}{\partial x}\left(\frac{\partial L}{\partial \theta_x}\right) + \frac{\partial}{\partial y}\left(\frac{\partial L}{\partial \theta_y}\right) - \frac{\partial L}{\partial \theta} = 0. \tag{3.8}$$

Again, by substituting the Lagrangian (3.5) we obtain equation (3.4)

An alternative form of the Lagrangian is to use a Green's function $G(x, y, x', y')$ for the solution of the director equation (3.4). In this case the Lagrangian can be written as

$$\begin{aligned} L &= i\left(E^* E_z - E E_z^*\right) - |\nabla E|^2 \\ &\quad + \frac{4}{\nu}|E|^2 \int_0^{L_y} \int_0^{L_x} |E\left(x', y'\right)|^2 \, G\left(x, y, x', y'\right) \, dx' \, dy'. \end{aligned} \tag{3.9}$$

This alternative Lagrangian arises as the director equation (3.4) is also solvable by using a Green's function. Thus, the solution for the director takes the form

$$\theta = \frac{2}{\nu} \int_0^{L_y} \int_0^{L_x} |E\left(x', y'\right)|^2 \, G\left(x, y, x', y'\right) \, dx' \, dy'. \tag{3.10}$$

The Green's function $G(x, y, x', y')$ satisfies the differential equation

$$\nu \nabla^2 G(x, y, x', y') = -\delta(x - x')\delta(y - y'). \tag{3.11}$$

The remainder of this chapter will concentrate on developing modulation equations for the two Lagrangians (3.5) and (3.9). To achieve this, two equivalent solutions for the director equation (3.4) will be derived.

3.2.2 Working towards the modulation equations - evolution of the system

As was stated in Chapter 2, the NLS-like governing equation (3.3) has no known exact solitary wave solution. In this case, approximate techniques, many based on averaged Lagrangian methods [39], have proved successful in obtaining solutions in excellent agreement with numerical and experimental results. Furthermore, these techniques have offered insights into the mechanisms and the underlying physics not available from numerical solutions alone [26, 42, 72, 83, 84, 85, 86, 87, 88]. To enable tracking of the evolutionary path of the nematicon, we shall use a hybrid of an exact solution and trial function and averaged Lagrangian techniques, as outlined in Chapter 2. There are two main choices for the profile of the trial function, each with their own advantages. They are a hyperbolic secant (sech) and a Gaussian. It was noted that the sech profile is the exact soliton solution for the one-dimensional NLS equation [60], while the Gaussian profile is the limiting profile of a nematicon in the limit of infinite nonlocality ν for the medium [89]. It has previously been shown that around its peak, a nematicon has a Gaussian profile, while in its tails it has the exponential decay of the modified Bessel function K_0, which is similar to the decay of the sech [36].

In this chapter we will use the Gaussian trial function, due to its simplicity for calculating the integrals for the averaged Lagrangian

$$E = \left(ae^{-r^2/w^2} + ig\right) e^{i\psi}, \tag{3.12}$$

where

$$r^2 = (x-\xi)^2 + (y-\eta)^2\,, \tag{3.13}$$

$$\psi = \sigma + V_x\,(x-\xi) + V_y\,(y-\eta)\,. \tag{3.14}$$

The trial function beam parameters are the amplitude a, width w, position (ξ, η), propagation constant (V_x, V_y), phase σ, and the shelf height g. These parameters are all functions of z. It can be seen from (3.13) that the trial function is radially symmetric. However, experimental results show that nematicons have a slight elliptic cross section [79]. This will be, for analytic simplicity, neglected in the modulation theory. The first term in (3.12) represents a slowly varying nematicon-like beam. The second term represents the shelf of low wavenumber diffractive radiation which accumulates under the evolving nematicon [60, 72], as described in Chapter 2. The existence of the shelf of radiation for the $(1+1)$D NLS equation has been shown using perturbed inverse scattering theory [60]. While for a coupled system of NLS equations, and for the defocussing NLS equation, the existence of the shelf of radiation has been shown using perturbation theory [73, 90, 91]. However, a simple explanation shows the existence of the shelf. The dispersion relation for the linearised electric field equation (3.3) is $\omega = |\mathbf{k}|^2/2$, so that the group velocity is $\mathbf{c}_g = \mathbf{k}$. Low wavenumber (corresponding to long wavelength) waves then have low group velocity and so accumulate under the evolving nematicon. The shelf is also $\pi/2$ out of phase with the nematicon and this is accounted for in the trial function (3.12) by the multiplication of g by i. This phase difference is seen when the in-phase perturbations serve to change the amplitude and width of the nematicon [60]. The variable g is the height of this radiation shelf.

Optical power cycles in and out of the shelf, resulting in the nematicon's amplitude and width oscillating as it evolves. This shelf of radiation cannot remain flat indefinitely, so it is assumed that g is nonzero in the disk $(x-\xi)^2 + (y-\eta)^2 \leq \ell^2$.

In previous work, the director angle θ was approximated by a sech^2 profile [72]. This was a good choice as the director was pre-tilted by a static external electric field, which caused the director response due to the light beam to decay exponentially away from it. However, when there is no static external electric field to pre-tilt the director, the response behaves logarithmically away from the light beam, as may be found from the director equation (3.4) on setting $E = 0$. This different decay rate of the light beam and the director response can be seen in figure 3.1. In this case it is better to solve the director equation (3.4) exactly, as found in previous work for a one-dimensional nematicon in a finite cell [30].

The equations will now be solved using two methods: a Fourier series solution which corresponds to the Lagrangian given by equation (3.5) and

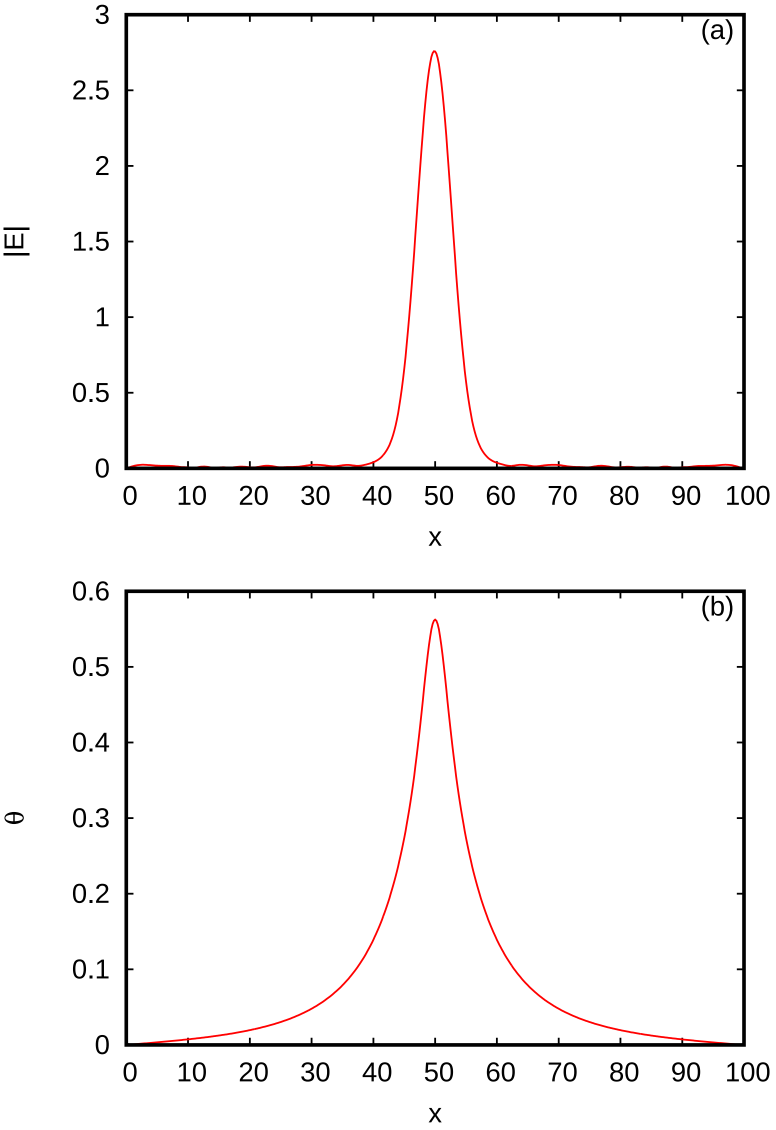

Figure 3.1: Electric field intensity versus x. Shown are the numerical solutions for (a) $|E|$ and (b) θ for $y = 25$ at $z = 500$. The initial values are $a = 2.5$, $w = 4$, $\xi = 50$, $\eta = 5$ with $\nu = 200$, $L_x = 100$ and $L_y = 50$.

a solution based on the method of images using a Green's function for the Laplacian, which occurs in the Lagrangian (3.9).

Fourier series

The director equation (3.4) has an exact solution using an eigenfunction expansion, a Fourier series, upon substitution the trial function (3.12) for the electric field envelope E. After neglecting the $O(g^2)$ contribution, the solution is found to be

$$\theta = -\sum_{n,m=1}^{\infty} \frac{C_{nm}}{\pi^2 Q_1} \sin\frac{n\pi x}{L_x} \sin\frac{m\pi y}{L_y}. \tag{3.15}$$

Using the orthogonality condition for the trigonometric functions the Fourier coefficients are

$$\begin{aligned} C_{nm} &= -\frac{8}{\nu L_x L_y} \int_0^{L_y}\int_0^{L_x} |E|^2 \sin\frac{n\pi x}{L_x} \sin\frac{m\pi y}{L_y}\, dx\, dy \\ &= -\frac{4\pi a^2 w^2}{\nu L_x L_y} e^{-\gamma_1} \sin\frac{n\pi \xi}{L_x} \sin\frac{m\pi \eta}{L_y}, \end{aligned} \tag{3.16}$$

where

$$Q_1 = \frac{n^2}{L_x^2} + \frac{m^2}{L_y^2}, \qquad \gamma_1 = \frac{\pi^2 Q_1 w^2}{8}. \tag{3.17}$$

The director solution (3.15) for θ and the trial function (3.12) for the electric field envelope E are now substituted into the Lagrangian (3.5), which is then averaged by integrating in x and y over the cell [39] to yield the averaged Lagrangian

$$\begin{aligned} \mathcal{L} = &-2\left(\frac{1}{4}a^2w^2 + \Lambda g^2\right)\left(\sigma' - V_x\xi' - V_y\eta' + \frac{1}{2}V_x^2 + \frac{1}{2}V_y^2\right) - aw^2g' + gw^2a' \\ &+ 2agww' - \frac{1}{2}a^2 + \frac{2a^4w^4}{\pi\nu L_x L_y}\sum_{n,m=1}^{\infty}\frac{e^{-2\gamma_1}}{Q_1}\sin^2\frac{n\pi\xi}{L_x}\sin^2\frac{m\pi\eta}{L_y}. \end{aligned} \tag{3.18}$$

Here $\Lambda = \ell^2/2$, which is the area under the shelf, modulo 2π. Taking variations of the averaged Lagrangian using the Euler–Lagrange equation we find the modulation equations

$$\frac{\partial}{\partial z}\frac{\partial \mathcal{L}}{\partial p_j'} - \frac{\partial \mathcal{L}}{\partial p_j} = 0, \tag{3.19}$$

where p_j and p_j' are the j $(= 1, 2, \ldots, n)$ nematicon parameters and their corresponding derivatives with respect to z. The modulation equations provide the evolutionary information for the propagating nematicon. This system of first-order ODEs, the modulation equations, is

$$\frac{d}{dz}\left[\frac{1}{4}a^2w^2 + \Lambda g^2\right] = 0, \tag{3.20}$$

$$\frac{d}{dz}(aw^2) = 2\Lambda g\left[\sigma' - V_x\xi' - V_y\eta' + \frac{1}{2}V_x^2 + \frac{1}{2}V_y^2\right], \tag{3.21}$$

$$\frac{d\xi}{dz} = V_x, \qquad \frac{d\eta}{dz} = V_y, \tag{3.22}$$

$$\frac{d}{dz}\left(\frac{1}{4}a^2w^2 + \Lambda g^2\right)V_x = \tag{3.23}$$
$$\frac{2a^4w^4}{\nu L_x^2 L_y}\sum_{n,m=1}^{\infty}\frac{ne^{-2\gamma_1}}{Q_1}\sin\frac{n\pi\xi}{L_x}\cos\frac{n\pi\xi}{L_x}\sin^2\frac{m\pi\eta}{L_y},$$

$$\frac{d}{dz}\left(\frac{1}{4}a^2w^2 + \Lambda g^2\right)V_y = \tag{3.24}$$
$$\frac{2a^4w^4}{\nu L_x L_y^2}\sum_{n,m=1}^{\infty}\frac{me^{-2\gamma_1}}{Q_1}\sin^2\frac{n\pi\xi}{L_x}\sin\frac{m\pi\eta}{L_y}\cos\frac{m\pi\eta}{L_y},$$

$$\frac{dg}{dz} = \frac{a}{2w^2} - \frac{\pi a^3w^4}{2\nu L_x L_y}\sum_{n,m=1}^{\infty}e^{-2\gamma_1}\sin^2\frac{n\pi\xi}{L_x}\sin^2\frac{m\pi\eta}{L_y}, \tag{3.25}$$

$$\frac{d\sigma}{dz} = -\frac{2}{w^2} + \frac{8a^2w^2}{\pi\nu L_x L_y}\sum_{n,m=1}^{\infty}\frac{e^{-2\gamma_1}}{Q_1}\sin^2\frac{n\pi\xi}{L_x}\sin^2\frac{m\pi\eta}{L_y} \tag{3.26}$$
$$+\frac{1}{2}(V_x^2 + V_y^2) + \frac{\pi a^2w^4}{\nu L_x L_y}\sum_{n,m=1}^{\infty}e^{-2\gamma_1}\sin^2\frac{n\pi\xi}{L_x}\sin^2\frac{m\pi\eta}{L_y}.$$

The modulation equation (3.20) is the equation for conservation of mass (optical power) and equations (3.23) and (3.24) are those for conservation of x and y momentum, respectively. The primary concern of the present work is the trajectory of the nematicon, which is given by the modulation equations (3.22), (3.23) and (3.24).

As the nematicon evolves it sheds diffractive radiation in order to settle to a steady state [60, 72, 74]. The flux of diffractive radiation from the nematicon has been calculated previously (see Section 2.3.4) [60, 72, 74]. From these previous works, we know to include loss to diffractive radiation in the mass equation (3.20) and the modulation equation (3.25) for g. They thus become

$$\frac{d}{dz}\left[\frac{1}{4}a^2w^2 + \Lambda g^2\right] = -2\delta\Lambda\kappa^2, \tag{3.27}$$

$$\frac{dg}{dz} = \frac{a}{2w^2} - \frac{\pi a^3 w^4}{2\nu L_x L_y}\sum_{n=1}^{\infty}\sum_{m=1}^{\infty} e^{-2\gamma_1}\sin^2\frac{n\pi\xi}{L_x}\sin^2\frac{m\pi\eta}{L_y} - 2\delta g. \tag{3.28}$$

The loss coefficient δ is

$$\delta = -\frac{\sqrt{2\pi}}{32e\kappa\tilde{\Lambda}}\int_0^z \pi\kappa(z')\ln[(z-z')/\tilde{\Lambda}]\times \tag{3.29}$$
$$\left[\left(\left\{\frac{1}{2}\ln[(z-z')/\tilde{\Lambda}]\right\}^2 + \frac{3\pi^2}{4}\right)^2 + \pi^2\left\{\ln[(z-z')/\tilde{\Lambda}]\right\}^2\right]^{-1}\frac{dz'}{(z-z')},$$

where

$$\kappa^2 = \frac{1}{\tilde{\Lambda}}\left[\frac{1}{4}a^2w^2 - \frac{1}{4}\hat{a}^2\hat{w}^2 + \tilde{\Lambda}g^2\right]. \tag{3.30}$$

One major effect of nonlocality is to shift the point at which the nematicon sheds diffractive radiation from the edge of the shelf $\sqrt{(x-\xi)^2 + (y-\eta)^2} =$

ℓ to a new radius $\tilde{\ell}$ from the nematicon position (ξ, η), which is the edge of the director response [72]. This radius for the radiation response was termed the outer shelf radius [72]. In the present case of a finite cell, the director response extends to the cell walls. Hence

$$\tilde{\Lambda} = \tilde{\ell}^2/2, \tag{3.31}$$

where

$$\tilde{\ell} = \min\left(\frac{L_x}{2}, \frac{L_y}{2}\right). \tag{3.32}$$

In the case of a finite cell, the diffractive radiation is then shed in a boundary layer at the cell walls.

The final steady state for the nematicon can be found from energy conservation. Total energy conservation for the nematicon can be found from Nöther's theorem based on the invariance of the Lagrangian (3.5) with respect to shifts in z. Nöther's theorem then gives that the energy conservation equation for the Lagrangian (3.5) is

$$\begin{aligned} &\frac{\partial}{\partial z}\left[\frac{\partial E}{\partial z}\frac{\partial L}{\partial E_z} + \frac{\partial E^*}{\partial z}\frac{\partial L}{\partial E_z^*} + \frac{\partial \theta}{\partial z}\frac{\partial L}{\partial \theta_z} - L\right] \\ &+ \frac{\partial}{\partial x}\left[\frac{\partial E}{\partial z}\frac{\partial L}{\partial E_x} + \frac{\partial E^*}{\partial z}\frac{\partial L}{\partial E_x^*} + \frac{\partial \theta}{\partial z}\frac{\partial L}{\partial \theta_x}\right] \\ &+ \frac{\partial}{\partial y}\left[\frac{\partial E}{\partial z}\frac{\partial L}{\partial E_y} + \frac{\partial E^*}{\partial z}\frac{\partial L}{\partial E_y^*} + \frac{\partial \theta}{\partial z}\frac{\partial L}{\partial \theta_y}\right] = 0. \end{aligned} \tag{3.33}$$

Averaging the energy conservation equation by integrating in x and y from

$-\infty$ to ∞ gives the average energy conservation equation

$$\frac{dH}{dz} = \frac{d}{dz}\int_0^{L_y}\int_0^{L_x}\left[\frac{\partial E}{\partial z}\frac{\partial L}{\partial E_z} + \frac{\partial E^*}{\partial z}\frac{\partial L}{\partial E_z^*} + \frac{\partial \theta}{\partial z}\frac{\partial L}{\partial \theta_z} - L\right] dx\, dy = 0, \tag{3.34}$$

which yields

$$\begin{aligned}\frac{dH}{dz} &= \frac{d}{dz}\int_0^{L_y}\int_0^{L_x}[|\nabla E|^2 - 4\theta|E|^2 + \nu|\nabla\theta|^2]\, dx\, dy \\ &= \frac{d}{dz}\left[\frac{1}{2}a^2 - \frac{2a^4w^4}{\pi\nu L_x L_y}\sum_{n,m=1}^{\infty}\frac{e^{-2\gamma_1}}{Q_1}\sin^2\frac{n\pi\xi}{L_x}\sin^2\frac{m\pi\eta}{L_y}\right] = 0. \end{aligned} \tag{3.35}$$

The final steady nematicon can be determined from this energy conservation equation (3.35) for any given initial input optical beam. The repulsive nature of the cell walls on the nematicon [43, 44] help it settle into the centre of the cell at the final steady state. Denoting the steady-state by a carat ˆ, we have $(\hat{\xi}, \hat{\eta}) = (L_x/2, L_y/2)$ and $V_x = V_y = 0$. Since the nematicon has settled to the steady state it will no longer shed diffractive radiation, that is $g = 0$. Solving equation (3.25) for $g = 0$, we find the steady state relationship between the amplitude $\hat{a}$ and width $\hat{w}$

$$\hat{a}^2 = \frac{\nu L_x L_y}{\pi \hat{w}^6}\left[\sum_{n,m=1}^{\infty} e^{-2\hat{\gamma}_1}\right]^{-1}, \tag{3.36}$$

where

$$\hat{\gamma_1} = \frac{\pi^2\hat{w}^2 Q_1}{8}. \tag{3.37}$$

Combining the energy conservation equation (3.35) and the steady state relationship (3.36), the final steady state amplitude and width of the nematicon can be determined for any initial input beam.

Method of images

An alternative technique to the Fourier series solution, found via an eigenfunction expansion for the director equation (3.4), is to use a Green's function G. The simplest manner in which to determine this Green's function is to use the method of images (MoI) [92].

The method of images is as follows. By taking a point source inside the (x, y) plane of the cell, say at (x', y'), a series of source and sink image terms is constructed around the point source, as shown in figure 3.2. This infinite series of images is constructed so that the boundary conditions at the cell walls are satisfied. The appropriate Green's function for the rectangular cell is then given by [92]

$$G(x, y, x', y') = -\frac{1}{2\pi}\mathrm{Re}\left\{\ln f(x, y, x', y')\right\}. \tag{3.38}$$

An expression for the function f needs to be found. As the function f has only simple poles and simple zeros and is periodic, the simplest analytical expression for f is in terms of elliptic functions [92]

$$f(x, y) = \frac{\sigma(h-\mu, x, y)\sigma(h+\mu, x, y)}{\sigma(h-\mu^*, x, y)\sigma(h+\mu^*, x, y)}, \tag{3.39}$$

where

$$h = x + iy, \qquad \mu = x' + iy',$$

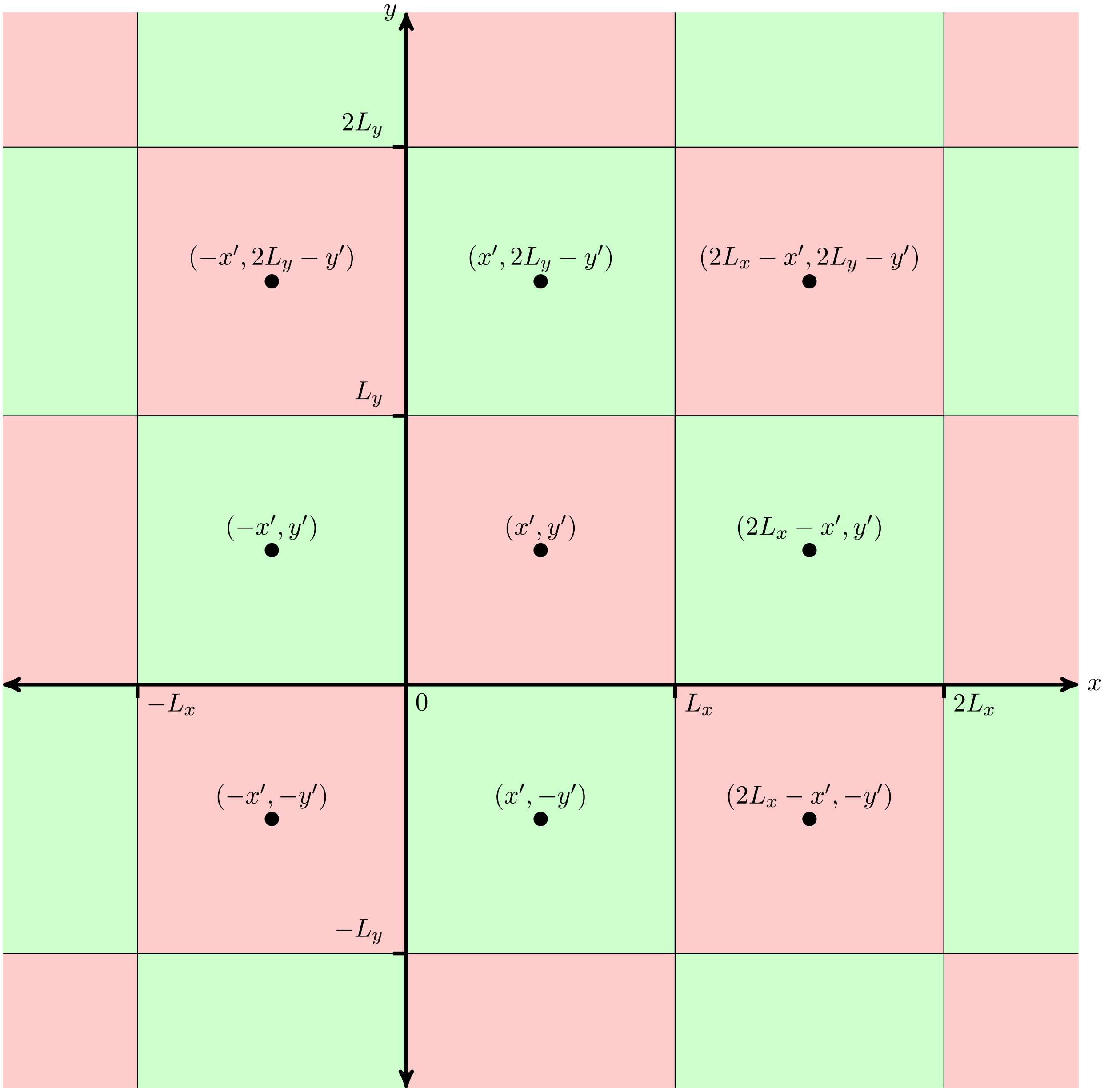

Figure 3.2: Method of images depicting the sources (red or dark squares) and the sinks (green or light squares) over the constructed lattice for the first eight images.

$$\sigma(u, x, y) = u \prod_{\omega \neq 0} \left[\left(1 - \frac{u}{2\omega}\right) e^{u/(2\omega)+u^2/(8\omega^2)} \right] \text{ [75].} \tag{3.40}$$

In equation (3.40) u is a complex valued function and

$$\omega = nL_x + imL_y, \qquad n = 0, \pm 1, ..., \quad m = 0, \pm 1, ...$$

This Green's function (3.38) is a conformal mapping of the half-plane onto a rectangle via the Weierstrass elliptic function σ [92] This makes the MoI a versatile technique for different geometries for which a closed form expression for the Green's function exists, via conformal mapping for instance. The Green's function (3.38) is now substituted into the solution (3.10) for θ. However, the resulting integral cannot be evaluated exactly. The NLC we are considering is in the nonlocal limit, that is large ν. Hence, the director response is much wider than the beam waist and a standard approximation can be made [45]. The Green's function does not show significant variation over the light beam [53, 88], allowing the Gaussian component of the trial function (3.12) to be replaced with a Dirac delta function. Hence,

$$\theta = \frac{2}{\nu} \int_0^{L_y} \int_0^{L_x} |E(x', y')|^2 \, G(x, y, x', y') \, dx' \, dy'$$

where

$$\begin{aligned} |E|^2 &\sim a^2 e^{-2r^2/w^2} \sim \pi a^2 w^2 \delta(x' - \xi) \, \delta(y' - \eta) \\ \theta &= \frac{\pi a^2 w^2}{\nu} \int_0^{L_y} \int_0^{L_x} G(x, y; x', y') \, \delta(x' - \xi) \, \delta(y' - \eta) \, dx' \, dy' \\ &= \frac{\pi a^2 w^2}{\nu} G(x, y, \xi, \eta). \end{aligned} \tag{3.41}$$

In this case, the solution (3.10) for the director perturbation θ can be approximated by (3.41), that is

$$\theta = -\frac{a^2w^2}{2\nu}\mathrm{Re}\left\{\ln\frac{\sigma(h-\tau,x,y)\sigma(h+\tau,x,y)}{\sigma(h-\tau^*,x,y)\sigma(h+\tau^*,x,y)}\right\}, \qquad (3.42)$$

where $\tau = \xi + i\eta$. This solution is now substituted into the Lagrangian (3.9), which is averaged over the cell in the $x-y$ plane to give the averaged Lagrangian

$$\begin{aligned}\mathcal{L} = &-2\left(\frac{1}{4}a^2w^2+\Lambda g^2\right)\left(\sigma' - V_x\xi' - V_y\eta' + \frac{1}{2}V_x^2 + \frac{1}{2}V_y^2\right)\\ &- aw^2g' + gw^2a' + 2agww' - \frac{a^2}{2} - \frac{a^4w^4}{4\nu}\Big[\Delta_1+\Delta_2-\Delta_3-\Delta_4\Big].\end{aligned} \qquad (3.43)$$

Here

$$\Delta_1 = \ln\frac{w}{\sqrt{2}} - \frac{\gamma}{2} - \ln 2 + \ln\sqrt{\xi^2+\eta^2} - \ln(\xi\eta), \qquad (3.44)$$

$$\begin{aligned}\Delta_2 = \sum_{n,m=-\infty}^{\infty}&\left[\frac{1}{2}\ln\frac{(nL_x-\xi)^2+(mL_y-\eta)^2}{n^2L_x^2+m^2L_y^2}\right.\\ &\left.+\frac{(\xi^2-\eta^2)(n^2L_x^2-m^2L_y^2)+4nm\xi\eta L_xL_y}{2(n^2L_x^2+m^2L_y^2)^2}\right],\end{aligned} \qquad (3.45)$$

$$\Delta_3 = \sum_{n,m=-\infty}^{\infty}\left[\frac{1}{2}\ln\frac{n^2L_x^2+(mL_y-\eta)^2}{n^2L_x^2+m^2L_y^2} + \frac{\eta^2(n^2L_x^2-m^2L_y^2)}{2(n^2L_x^2+m^2L_y^2)^2}\right], \qquad (3.46)$$

$$\Delta_4 = \sum_{n,m=-\infty}^{\infty}\left[\frac{1}{2}\ln\frac{(nL_x-\xi)^2+m^2L_y^2}{n^2L_x^2+m^2L_y^2} + \frac{\xi^2(n^2L_x^2-m^2L_y^2)}{2(n^2L_x^2+m^2L_y^2)^2}\right], \qquad (3.47)$$

where γ is Euler's constant, $\gamma = 0.577215665$ [75].

Taking variations of the averaged Lagrangian (3.43) with respect to the nematicon parameters results in the system of first-order ODEs, or modulation equations,

$$\frac{d}{dz}\left[\frac{1}{4}a^2w^2+\Lambda g^2\right] = 0, \qquad (3.48)$$

$$\frac{d}{dz}(aw^2) = 2\Lambda g\left[\sigma' - V_x\xi' - V_y\eta' + \frac{1}{2}V_x^2 + \frac{1}{2}V_y^2\right], \tag{3.49}$$

$$\frac{d\xi}{dz} = V_x, \qquad \frac{d\eta}{dz} = V_y, \tag{3.50}$$

$$\begin{aligned}\frac{d}{dz}\left(\frac{1}{4}a^2w^2 + \Lambda g^2\right)V_x = \frac{a^4w^4}{8\nu}\Bigg\{&\frac{\eta^2}{\xi\,(\xi^2+\eta^2)} - \sum_{n,m=-\infty}^{\infty}\frac{nL_x-\xi}{(nL_x-\xi)^2+m^2L_y^2}\\ &+\sum_{n,m=-\infty}^{\infty}\left[\frac{nL_x-\xi}{(nL_x-\xi)^2+(mL_y-\eta)^2} - \frac{2\eta nmL_xL_y}{(n^2L_x^2+m^2L_y^2)^2}\right]\Bigg\},\end{aligned} \tag{3.51}$$

$$\begin{aligned}\frac{d}{dz}\left(\frac{1}{4}a^2w^2 + \Lambda g^2\right)V_y = \frac{a^4w^4}{8\nu}\Bigg\{&\frac{\xi^2}{\eta\,(\xi^2+\eta^2)} - \sum_{n,m=-\infty}^{\infty}\frac{mL_y-\eta}{n^2L_x^2+(mL_y-\eta)^2}\\ &+\sum_{n,m=-\infty}^{\infty}\left[\frac{mL_y-\eta}{(nL_x-\xi)^2+(mL_y-\eta)^2} - \frac{2\xi nmL_xL_y}{(n^2L_x^2+m^2L_y^2)^2}\right]\Bigg\},\end{aligned} \tag{3.52}$$

$$\frac{dg}{dz} = \frac{a}{2w^2} - \frac{a^3w^2}{8\nu}, \tag{3.53}$$

$$\frac{d\sigma}{dz} = -\frac{2}{w^2} + \frac{1}{2}(V_x^2+V_y^2) - \frac{a^2w^2}{\nu}\left[\Delta_1 + \Delta_2 - \Delta_3 - \Delta_4 - \frac{1}{4}\right]. \tag{3.54}$$

The modulation equation (3.48) is the equation for conservation of mass (optical power) and equations (3.51) and (3.52) are those for conservation of x and y momentum, respectively. The primary concern of the present work is the trajectory of the nematicon, which is given by the modulation equations (3.50), (3.51) and (3.52).

From previous discussions, as the nematicon evolves it sheds diffractive radiation in order to settle to a steady state (see Section 2.3.4) [60, 72, 74]. As in the Fourier series approach, to account for the shed radiation the modulation equations (3.48) and (3.53) are modified to become

$$\frac{d}{dz}\left[\frac{1}{4}a^2w^2+\Lambda g^2\right]=-2\delta\Lambda\kappa^2, \tag{3.55}$$

$$\frac{dg}{dz}=\frac{a}{2w^2}-\frac{a^3w^2}{8\nu}-2\delta g. \tag{3.56}$$

The loss coefficient δ is given by (3.29), with $\tilde{\Lambda}$ given by (3.31).

Nöther's theorem may again be used to find the averaged energy conservation equation

$$\begin{aligned}\frac{dH}{dz}&=\frac{d}{dz}\int_0^{L_y}\int_0^{L_x}\left[|\nabla E|^2-2|E|^2\theta\right]\,dx\,dy\\&=\frac{d}{dz}\left\{\frac{1}{2}a^2+\frac{a^4w^4}{4\nu}\left[\Delta_1+\Delta_2-\Delta_3-\Delta_4\right]\right\}=0.\end{aligned} \tag{3.57}$$

The final steady state nematicon can be determined from this energy conservation equation. The relationship between the steady state amplitude $\hat{a}$ and width $\hat{w}$ is given by the modulation equation (3.53) with $g=0$, yielding

$$\hat{a}^2=\frac{4\nu}{\hat{w}^4}. \tag{3.58}$$

The final steady state values for any initial input light beam can now be calculated using the combination of (3.57) and (3.58).

The final parameter to be determined is the shelf radius ℓ. In previous studies the modulation equations were linearised about their steady state. This resulted in a simple harmonic oscillator equation [60, 83]. The frequencies of this oscillator and the steady state nematicon were then matched to determine Λ [60, 83]. However, in a finite cell this method does not work for the present modulation equations, as was the case for a one-dimensional nematicon in a finite cell [30]. The reason is that a localised distribution is not formed around the perturbation of the director angle θ, as is the case for an infinite cell where the pre-tilting of the nematic molecules is done via a static external electric field [30, 72, 83]; see figure 3.1. To overcome this problem, there is a matching of the frequency of the nematicon's amplitude oscillation as given by the modulation equations to the full numerical solution for a particular input beam. The established frequency was then shown to be robust for different input beams, as was the situation for the one-dimensional case [30].

The shelf radius is taken to be

$$\ell = \frac{3\beta\pi^2\hat{w}}{8}, \tag{3.59}$$

where β is a constant to be determined by the above matching and validation process. The shelf length for the NLS equation is found when $\beta = 1$ in this expression [60]. It was found that $\beta = 0.4$ gave a robust match for the period of the numerical solutions.

An alternative derivation of the Green's function is as follows. The Green's function $G(x, y, x', y')$ satisfies

$$\nabla^2 G(x, y, x', y') = -\delta(x - x')\delta(y - y') \tag{3.60}$$

with homogeneous boundary conditions on the cell walls. An equivalent solution of this equation is

$$G(x, y, x', y') = \frac{4}{\pi^2 L_x L_y} \sum_{n,m=1}^{\infty} \frac{\phi_n(\xi)\phi_m(\eta)\phi_n(x)\phi_m(y)}{Q_1}, \tag{3.61}$$

where

$$\phi_n(x) = \sin \frac{n\pi x}{L_x}, \qquad \phi_m(y) = \sin \frac{m\pi y}{L_y}. \tag{3.62}$$

Substitution into the solution (3.10) for θ yields the Fourier series solution (3.15). This shows that the two methods of solution for the director angle are equivalent. The Green's function solution via the MoI rearranges the infinite series in another form. Numerical computations give excellent agreement for the equilibrium nematicon as given by the Fourier series (3.35) and the MoI solution (3.57), as required.

3.3 Results

In this section the full numerical solution for the nematicon governing equations (3.3) and (3.4) will be compared with the modulation solution to test the accuracy and reliability of the approximations used to derive the approximate equations for the evolution of the nematicon as it propagates down the NLC cell. The numerical method presented in Section 2.4 will be used here with the trial function for the electric field envelope E (3.12) with $g = 0$ forming the initial input beam. The step sizes used to compute the full numerical solution are $\Delta x = \Delta y = 0.2$ and $\Delta z = 0.001$. The size of the cell was chosen based on typical experimental sizes, with the non-dimensional values of 50 and 100 used. A propagation distance of $z = 500$ was chosen as this is a typical non-dimensional cell length [26].

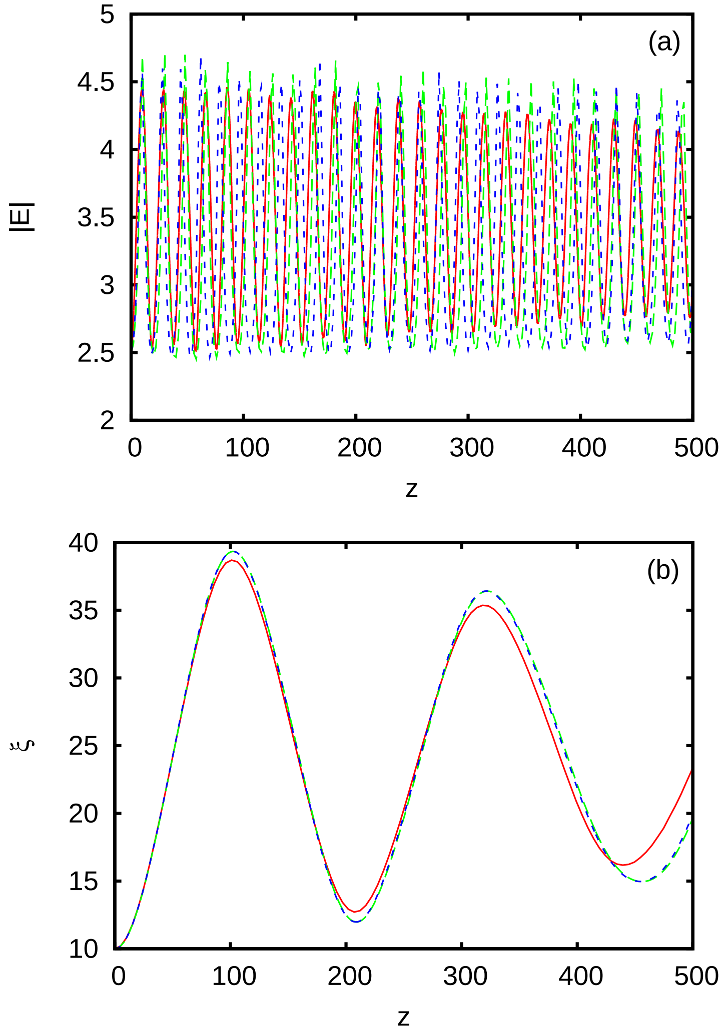

Figure 3.3: Comparison between the full numerical solution (red solid line), Fourier series solution (green dashed line) and method of images solution (blue dot-dashed line) for the (a) amplitude a and (b) x position for a square cell. The initial values are $a = 2.5$, $w = 4$, $\xi = 10$, $\eta = 15$, $V_x = 0$ and $V_y = 0$ with $\nu = 200$, $L_x = 50$ and $L_y = 50$.

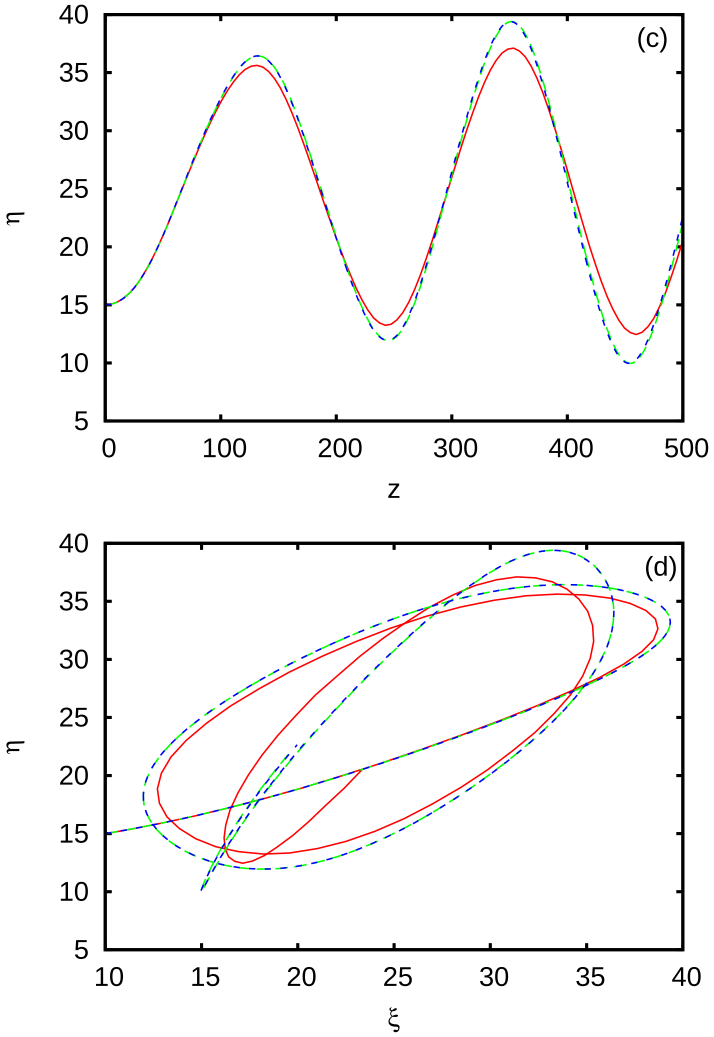

Figure 3.3: Comparison between the full numerical solution (red solid line), Fourier series solution (green dashed line) and method of images solution (blue dot-dashed line) for the (c) y position and (d) x-y position for a square cell. The initial values are $a = 2.5$, $w = 4$, $\xi = 10$, $\eta = 15$, $V_x = 0$ and $V_y = 0$ with $\nu = 200$, $L_x = 50$ and $L_y = 50$.

Let us first consider the propagation of a nematicon in a square cell. While in experiments the cell geometry is rectangular, we start with the simple case of a square cell so as to gather information as to whether the aspect ratio of the cell has an effect on the propagation of the nematicon. Figure 3.3 shows a comparison between the full numerical solution (solid red line) and the modulation solution based on the Fourier series green (dashed line) and MoI (blue dot-dashed line) for this square cell.

Excellent agreement is seen between the modulation solution and the full numerical solution for both the amplitude (figure 3.3(a)) and the trajectory (figure 3.3(d)). There is a small period difference between the amplitude oscillations as given by the modulation and full numerical solutions, with the Fourier series giving a better period agreement than the MoI. This shift in period is caused by the amplitude and width oscillations forming a nonlinear oscillator. Hence, the slight difference seen between the amplitude oscillations for the modulation and full numerical solutions translates to a shift in the period. However, the overall envelope of the amplitude given by the modulation solution is in excellent agreement with the full numerical solution.

The position of the nematicon as given by both the modulation solutions (Fourier and MoI) is identical, but there is a difference in the amplitude evolution. This is due to the evaluation of the integrals for the different

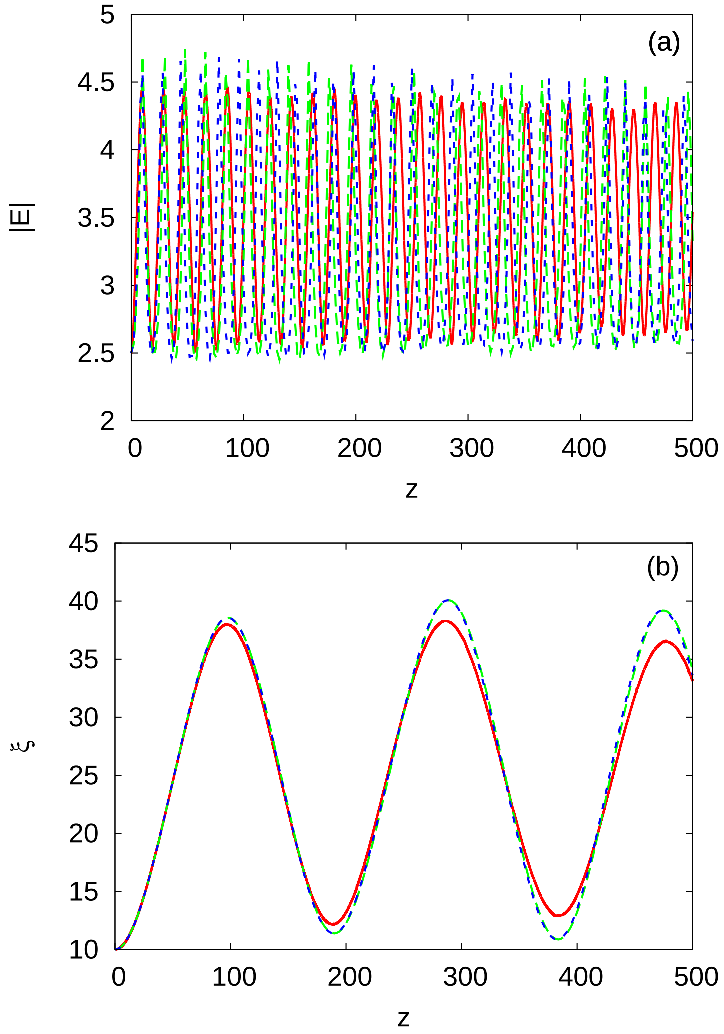

Figure 3.4: Comparison between the full numerical solution (red solid line), Fourier series solution (green dashed line) and method of images solution (blue dot-dashed line) for the (a) amplitude a and (b) x position for a rectangular cell. The initial values are $a = 2.5$, $w = 4$, $\xi = 10$, $\eta = 15$, $V_x = 0$ and $V_y = 0$ with $\nu = 200$, $L_x = 50$ and $L_y = 100$.

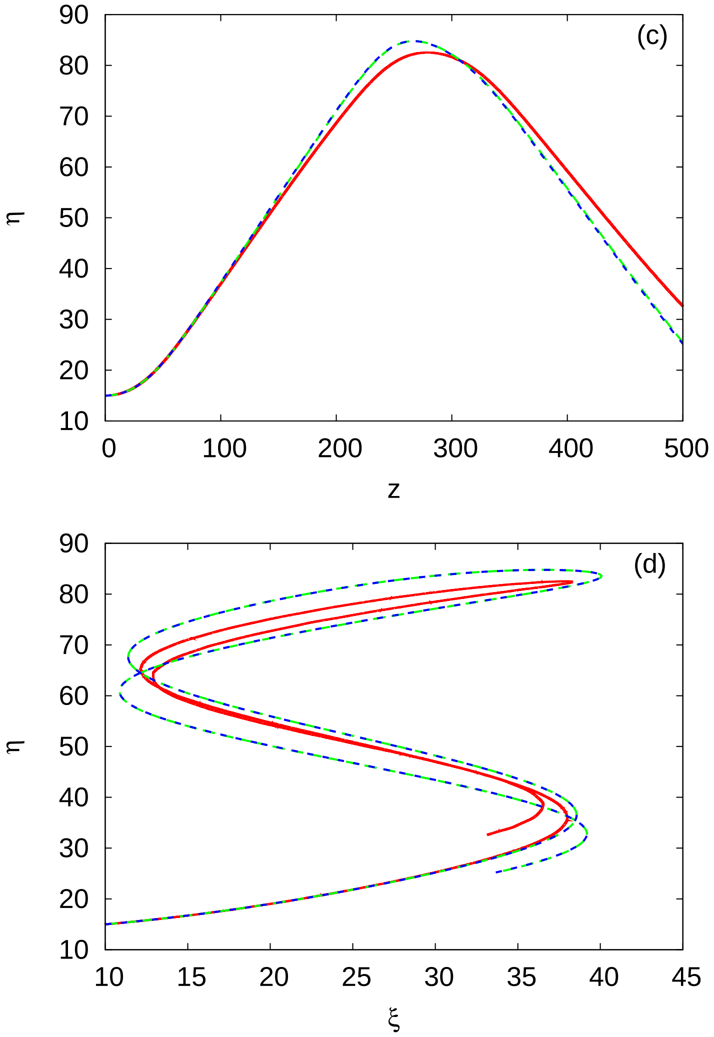

Figure 3.4: Comparison between the full numerical solution (red solid line), Fourier series solution (green dashed line) and method of images solution (blue dot-dashed line) for the (c) y position and (d) x-y position for a rectangular cell. The initial values are $a = 2.5$, $w = 4$, $\xi = 10$, $\eta = 15$, $V_x = 0$ and $V_y = 0$ with $\nu = 200$, $L_x = 50$ and $L_y = 100$.

modulation methods. The integrals for the Fourier series solution were evaluated exactly for the director solution θ, while the integrals for the MoI involving the Green's function (3.10) required asymptotic approximations for evaluation. Note that this approximate evaluation had a greater effect on the amplitude than on the position. The effects of the cell walls on a nematicon can be seen in figure 3.3(d) where it can be seen that they impart a repulsive force towards the centre of the cell [43, 44].

Importantly, the modulation equations based on the MoI are computationally faster than the Fourier series solution. Since the position is the only data experimentally available and both sets of modulation equations give identical trajectories, the MoI has an advantage over the Fourier series solution.

Let us consider the physically more realistic case of a rectangular cross-sectional cell, where the comparison of techniques is shown in figure 3.4.

The aspect ratio chosen replicates a case of two-dimensional nematicon propagation studied in [30]. In this work the motion of the nematicon was considered to be two independent movements, one in the x direction and the other in the y direction. The agreement between the modulation and full numerical solutions is similar to that for a square cell shown in figure 3.3. Again, the Fourier series and MoI solutions give identical positional information and give excellent agreement with the full numerical solution. The amplitude comparison maintains the small period difference between

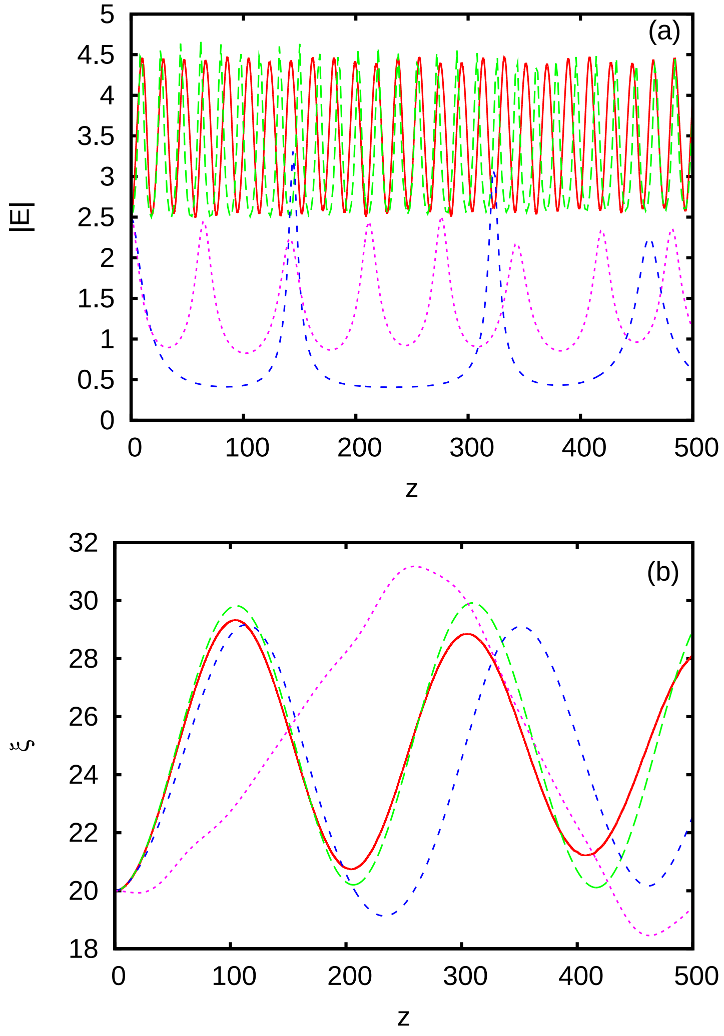

Figure 3.5: Comparison between the full numerical solution (red solid line), Fourier series solution (green long dashed line), the Fourier series solution with fundamental only (magenta dotted line), and the fundamental plus first harmonic (blue short dashed line) for the (a) amplitude a and (b) x position for a rectangular cell. The initial values are $a = 2.5$, $w = 4$, $\xi = 20$, $\eta = 25$, $V_x = 0$ and $V_y = 0$ with $\nu = 200$, $L_x = 50$ and $L_y = 100$.

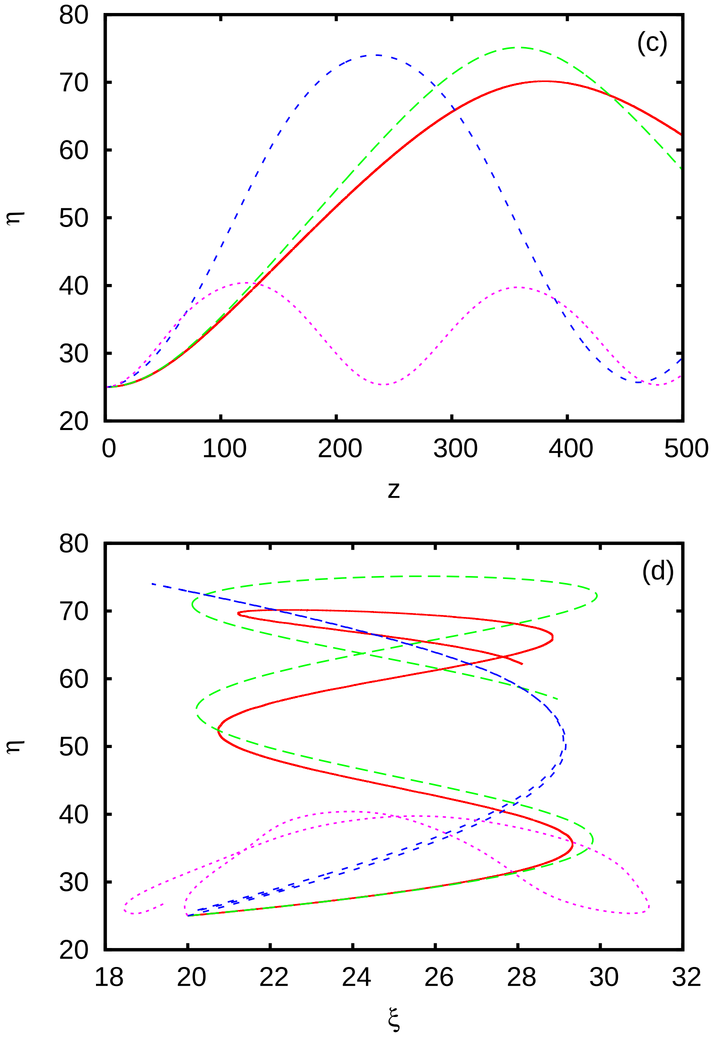

Figure 3.5: Comparison between the full numerical solution (red solid line), Fourier series solution (green long dashed line), the Fourier series solution with fundamental only (magenta dotted line), and the fundamental plus first harmonic (blue short dashed line) for the (c) y position and (d) x-y position for a rectangular cell. The initial values are $a = 2.5$, $w = 4$, $\xi = 20$, $\eta = 25$, $V_x = 0$ and $V_y = 0$ with $\nu = 200$, $L_x = 50$ and $L_y = 100$.

the modulation and full numerical solution oscillations. This is linked to the slight difference in the amplitude oscillations, as well as the modulation solutions faster decay rate to the steady state.

The major dynamical difference between the square and rectangular cells is the number of boundary interactions along the increased distance in the y direction. The nematicon is required to travel further to now interact with the boundary. It is found that the agreement in position between the modulation and the full numerical solutions is much better than for the two independent one-dimensional motion approximation of [30]. This is as expected, as the present theory in this chapter is fully two-dimensional.

The director distribution for the Fourier series solution in a finite cell is commonly approximated by its first term [93]. This approximation is of particular importance when nonparaxial effects are studied as it greatly reduces the numerical computation involved as then the Laplacian is in two, not three, dimensions. It is found that the numerical solutions of the nonparaxial nematicon equations for the nematicon trajectory are in good agreement with experimental results [93]. The Fourier series solution derived here will be used to show the validity of this approximation. In figure 3.5 the full numerical solution for the nematicon equations is compared with the full Fourier series modulation equations and the Fourier series modulation equations with that for only the fundamental and the fundamental plus first harmonic in the series. Figure 3.5(a) indicates that the truncated Fourier

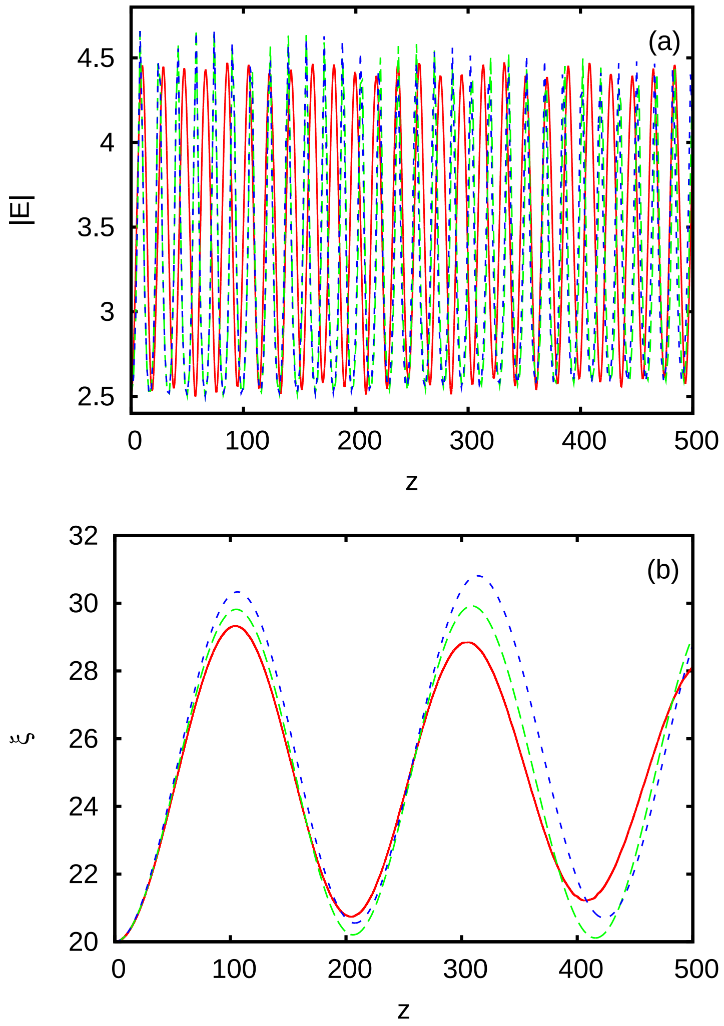

Figure 3.6: Comparison between the full numerical solution (red solid line), MoI solution (green long dashed line), and MoI solution taking only the first eight images (blue dashed line) for the (a) amplitude a and (b) x position for a rectangular cell. The initial values are $a = 2.5$, $w = 4$, $\xi = 20$, $\eta = 25$, $V_x = 0$ and $V_y = 0$ with $\nu = 200$, $L_x = 50$ and $L_y = 100$.

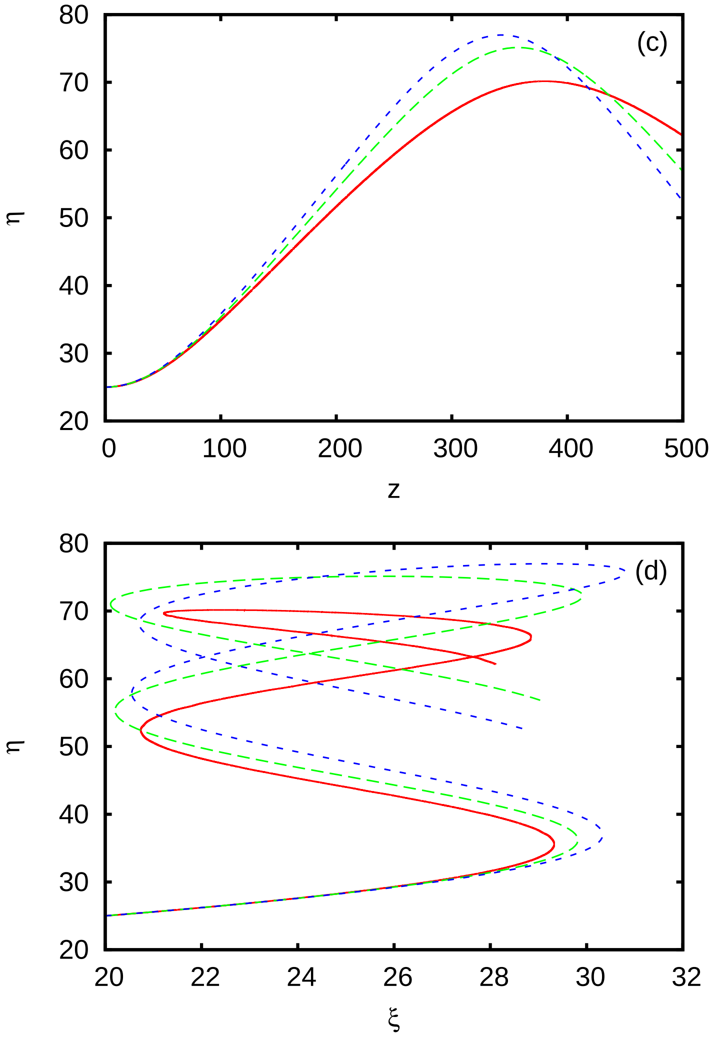

Figure 3.6: Comparison between the full numerical solution (red solid line), MoI solution (green long dashed line), and MoI solution taking only the first eight images (blue dashed line) for the (c) y position and (d) x-y position for a rectangular cell. The initial values are $a = 2.5$, $w = 4$, $\xi = 20$, $\eta = 25$, $V_x = 0$ and $V_y = 0$ with $\nu = 200$, $L_x = 50$ and $L_y = 100$.

series results in a poor amplitude comparison, while in figure 3.5(b) the position of the nematicon as found by the Fourier series including only the fundamental mode maintains a good comparison. Paradoxically, when the second harmonic mode is included the Fourier series gives a much poorer trajectory comparison. However, it improves the amplitude comparison. This is the consequence of using such low dimensional approximations compared to the full series. The results in figure 3.5 demonstrate the adequacy of the approximation used in [93] when numerical and experimental results for the nematicon trajectory are compared and only the fundamental mode is used in the approximation. The beam intensity was not compared in [93], which is a more difficult comparison.

The MoI solution (3.42) for the director equation is expressed in terms of an infinite series, and naturally a truncation of the series can also be applied and compared with the full numerical solution. Figure 3.6 shows the comparison of the full numerical solution with the MoI modulation equations solution, and the MoI modulation equations solution with only the fundamental eight images which form the nearest neighbours to the physical cell are used (see figure 3.2). It can be seen that use of these nine terms (the source plus eight images) gives an excellent comparison for both the amplitude and the trajectory of the nematicon. The reason for this is that the contribution of an image term to the solution decays both with the distance the image is from the physical cell and the cell dimensions. This shows that, for simplicity, the full images solution need not be used and the much simpler approximation of the fundamental eight images and the point source gives a good approximation.

3.4 Discussion

In this chapter we have investigated the propagation of a bulk solitary wave, or nematicon, in a finite nematic liquid crystal cell. The cell walls have been pretreated by rubbing to give the nematic molecules a pre-tilt in order to overcome the Freéderickzs threshold. To investigate the evolution of the nematicon a hybrid exact solution-modulation theory technique has been used, with the director perturbation resulting from the nematicon being found using two techniques: a Fourier series solution and a Green's function solution based on the MoI. It was shown that the two solution methods were mathematically equivalent by showing that the Green's function can be rewritten as Fourier series. In practice, these techniques have a different utility. Both methods have been found to give excellent agreement with the full numerical solutions of the governing equations. The major difference between the two methods occurs when the series is prematurely truncated, to give simpler approximate solutions. Using only the fundamental or fundamental plus the first harmonic in the Fourier series solution gives an adequate approximation for the path of the nematicon through the NLC cell, but not the amplitude (power) evolution. In contrast, using the source point plus the eight neighbouring images in the MoI solution gives excellent amplitude and positional agreement for the nematicon. The truncation of the Fourier series validates an approximation used in the study of nonparaxial effects [93]. The present chapter shows that the MoI, while it has not been widely used to analytically study nematicon evolution, has promise as an alternative to using Fourier series solutions for the director distribution. The bouncing of the nematicon by the cell walls is then clearly seen as the effect of the images. The MoI can be used for the equations describing nonlinear beam evolution in other bulk media [16, 24, 64, 65, 66, 67, 94, 95]. In this regard, the view of the effect of the cell walls as due to image sources has promise [46].

The Green's function used to solve the director angle was for the half-plane conformally mapped onto a rectangle. It is this ease of derivation for different cell geometries that allows the MoI the flexibility to be applied to any study of beam evolution in other geometries for which a closed form conformal map exists.

Chapter 4

Vortices in bounded NLC cells

4.1 Background

The study of optical vortices has been of interest for many years, beginning with the initial theoretical work of Nye and Berry [96], who mathematically studied the phase dislocations in a wave train. An optical vortex is a light beam which has an azimuthal twist, resulting in a corkscrew like structure, such that its azimuthal phase increases by $2n\pi$, with n an integer, over one twist. The integer n is referred to as the charge of the vortex. This optical phenomenon has been termed a vortex for its similarity with a vortex in fluid flow. The optical field amplitude is zero at the centre to adjust to the phase singularity there. Optical vortices have been shown to exist in many media, including photorefractive lattices [97, 98], rubidium vapour cells [99, 100] and Bose–Einstein condensates [101]. A nematic liquid crystal (NLC), as mentioned in previous chapters, is an ideal medium for its potential use in all-optical devices [24, 29, 79] and is no exception when it comes to optical vortex formation and propagation. Optical vortex solitary waves are unstable in local media. However, in nonlocal media (such as NLC) the propagation of a stable optical vortex solitary wave is supported. The reason for this is that if the nonlocality is large enough, it can suppress the symmetry breaking mode-2 azimuthal instability [52, 53]. In contrast to local media [50, 51], optical vortex solitary waves in nonlocal media have received considerably less attention, especially in a NLC [46, 47, 48, 49, 53, 88, 102].

An optical vortex can be generated experimentally when a diffracting light beam's smooth wavefront is input through a computer generated holographic mask [99, 103], as shown in figure 4.1. This creates a helical phase ramp whose thickness increases around the centre (the singularity) of the vortex by $2n\pi$, where $n = 1, 2, \ldots$ is the topological charge of the vortex [46]. The helical phase ramp with a topological charge $n = 1$ is shown in figure 4.2, where only one winding occurs.

A gradient of circulation is forced in the angular variable around the vortex, with the amplitude at the centre equal to zero to compensate for the phase singularity as discussed earlier and shown in figure 4.3. An optical vortex in NLC undergoes the same formation process as an optical solitary wave or nematicon does, whereby a balance between the diffractive spreading of a light beam and the self-focusing induced by the nonlinear dependence of the refractive index of the NLC on the beam's intensity exists [29, 36]. As was mentioned extensively in the previous Chapters 1, 2 and 3, the Freédericksz threshold is a requirement that a minimum beam power is needed to obtain a rotation of the nematic molecules, which in turn self-focuses the light beam [23, 24, 25, 104]. Rubbing the NLC cell walls is one way to overcome the Freédericksz threshold by creating a static charge which pre-tilts the nematic molecules at the cell walls by an angle θ_0. Here, the nonlocality of the NLC, the intermolecular elastic forces [25], propagates this pre-tilt angle throughout the bulk of the medium, thus allowing the use of milliwatt beam powers to form an optical vortex solitary wave. The pre-tilt angle is set to be $\theta_0 \sim \pi/4$ as it has been shown that θ_0 is a minimum when the nematic molecules make an angle of $\pi/4$ with the z axis [33]. Thus, pre-tilting the nematic molecules by rubbing creates a linear (1D) or logarithmic (2D) decay of the nematic response away from the beam centre [30, 44]. This implies that all the nematic molecules are affected by the presence of the beam in the cell [30] and particular attention must be placed on the proper inclusion of the boundary conditions.

In this chapter, the behaviour and propagation of an optical vortex solitary wave in a finite nematic cell will be investigated. This chapter is concerned with nonlinear optical vortex solitary waves, and not with linear optical vortices. From now on the term optical vortex will mean nonlinear optical vortex solitary wave. This chapter will focus on the effect of the cell boundaries on both the propagation and stability of the optical vortex. The task is achieved by a blend of an exact solution found using two alternative, but equivalent methods, as described in Chapter 3 for a nematicon. These methods being an eigenfunction expansion and the method of images (MoI), plus a trial function coupled with a Lagrangian formulation of the governing equations and modulation theory [39].

The use of modulation theory with suitable trial functions to model optical beams has proved highly successful, with excellent comparisons with full numerical solutions [42, 53, 72, 84, 88, 102, 105] and experimental results [26, 106].

A study of the propagation of an optical vortex in a finite NLC cell will form the first half of this chapter, while an analysis of the stability of an optical vortex will be explored in the second half.

4.2 Analysis

4.2.1 Optical vortex governing equations

An optical vortex is input at the NLC-air interface of a cell filled with nematic liquid crystal. The z direction is taken as the non-dimensional

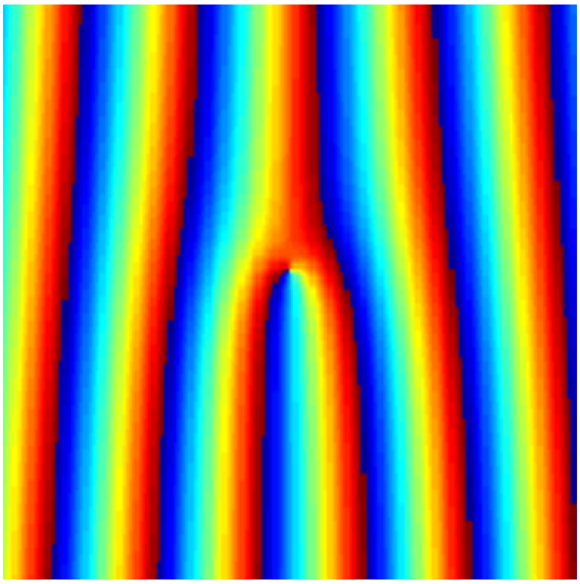

Figure 4.1: A computer-generated holographic mask which the optical beam is input through, resulting in the winding of the beam around the phase singularity.

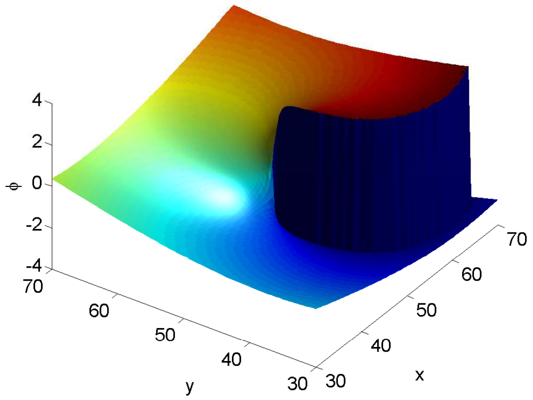

Figure 4.2: Depiction of the phase ramp with one circulation of the beam around the singularity, $n = 1$ of a $(50, 50)$ NLC cell.

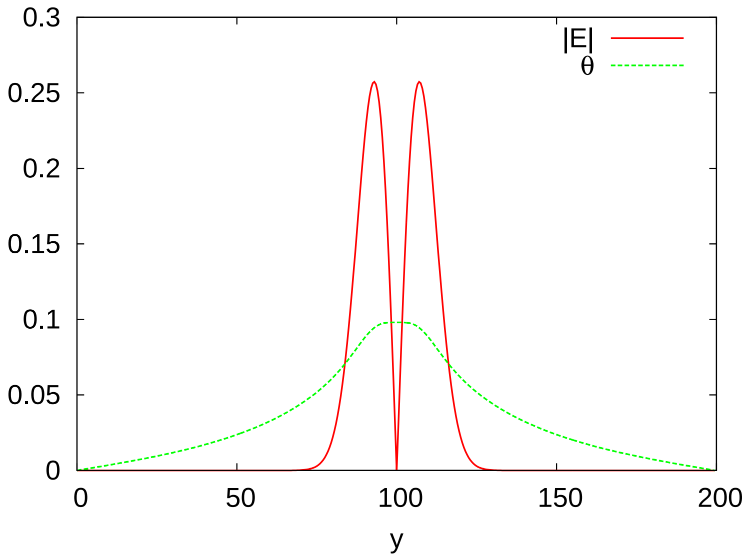

Figure 4.3: Shows the phase singularity at $y = 100$ for the beam profile (red solid line) and the director angle (green dashed line) using a Gaussian trial function given by equation (4.6).

propagation direction down the cell, with the $x - y$ plane perpendicular to this. The optical beam is polarised in the x (non-dimensional) direction. The nematic molecules are rotated in the $x - z$ plane due to rubbing and are arranged in a planar configuration within the cell. The intermolecular elastic forces between the nematic molecules are used to pass the pre-tilt angle θ_0 induced by the static charge created from rubbing the cell walls through the bulk of the medium. The application of the pre-tilt overcomes the Freédericksz threshold [23, 28, 36], a threshold which requires a minimum beam power to rotate the nematic molecules. As stated previously, the Freédericksz threshold is a minimum when the molecules are pre-tilted by

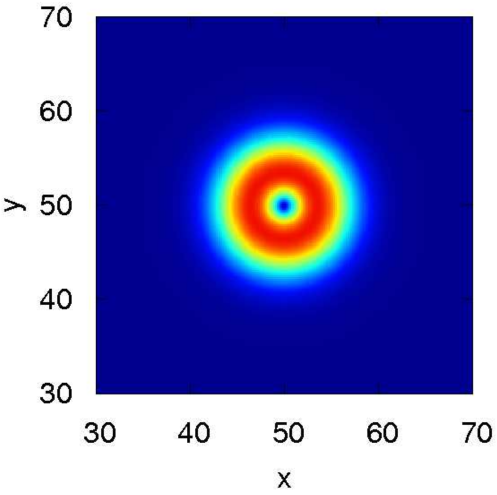

(a) Profile for an optical vortex.

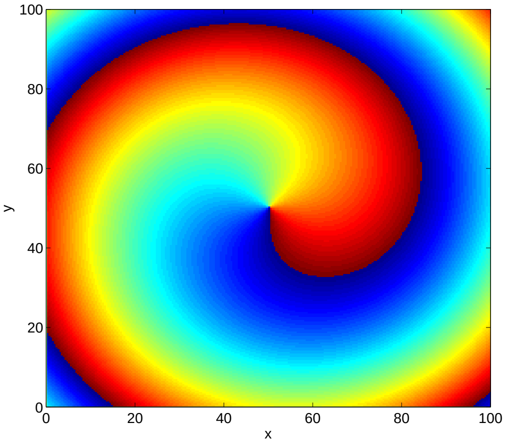

(b) Phase plot for the profile of an optical vortex, with the phase singularity occurring in the centre of the spiral.

Figure 4.4: An example of an initial optical profile and phase plot showing the phase singularity at the centre of the vortex.

$\theta_0 = \pi/4$ [33]. This allows milliwatt beam powers to be used, as they can now self-focus and form optical vortices with the nonlinear self-focusing balancing the diffractive spreading [29]. The optical field therefore causes an additional rotation θ of the director, so that the total director angle is $\theta_0 + \theta$ to the z direction. For milliwatt beam powers, this extra rotation is small $|\theta| \ll |\theta_0|$. In this small extra rotation limit, the governing equations are as described in (2.14) and (2.16) with $q = 0$. The non-dimensional equations governing the propagation of the optical vortex beam in the paraxial approximation are then [30, 43, 44, 45]

$$iE_z + \frac{1}{2}\nabla^2 E + 2\theta E = 0, \tag{4.1}$$

$$\nu \nabla^2 \theta + 2|E|^2 = 0. \tag{4.2}$$

The Laplacian ∇^2 is in the $x - y$ plane [29, 36, 72]. E is the complex valued envelope of the optical beam's electric field. The nonlocality parameter ν is related to the elastic response of the nematic and is experimentally of the order of $O(100)$ [26]. The light beam experiences a phenomenon known as walk-off, whereby the beam deviates from the input wavevector. The walk-off angle is the angle between the Poynting vector and the input beam's wavevector. As the nematic is uniform and the walk-off is also constant, it can be removed from the governing equations by a phase factor [40, 42], which has been done in deriving (4.1). The cell geometry is rectangular in the cross section, with $0 \leq x \leq L_x$ and $0 \leq y \leq L_y$ and is shown in figure 2.1.

The governing equations (4.1) and (4.2) have the following equivalent Lagrangians

$$L = i\left(E^* E_z - E E_z^*\right) - |\nabla E|^2 + 4\theta |E|^2 - \nu |\nabla \theta|^2, \tag{4.3}$$

$$L = i\left(E^* E_z - E E_z^*\right) - |\nabla E|^2 + 2\theta |E|^2. \tag{4.4}$$

The * denotes the complex conjugate. The two distinct Lagrangians arise due to the two alternative methods used to solve the director equation (4.2). Equation (4.3) uses an eigenfunction expansion to write the director angle θ as an infinite series solution, while for the Lagrangian (4.4) the director equation is solved using a Green's function $G(x, y, x', y')$, so that

$$\theta = \frac{2}{\nu} \int_0^{L_y} \int_0^{L_x} |E(x', y', z)|^2 G(x, y, x', y')\, dx'\, dy'. \tag{4.5}$$

This chapter will now focus on the application of the semi-analytical method (as described in Chapter 2) to the problem of an optical vortex propagating in a finite NLC cell.

4.2.2 Optical vortex: The evolutionary process

A point that has been discussed previously in this thesis is the fact that the governing equations (4.1) and (4.2) have no known exact solitary wave solution and in this specific case they have no known vortex solution [72]. As a result techniques based around averaged Lagrangian methods [39] have proven successful in the past in gaining insights into the underlying physics and mechanics of the nonlinear beams that full numerical solutions cannot supply. The analysis presented in this chapter is based on an exact solution and a trial function averaged Lagrangian method [30, 45, 88]. The trial function for the optical beam's electric field uses a Gaussian profile and is given by

$$E = \left(are^{-r^2/w^2} + ig\right) e^{i\psi + in\phi}, \tag{4.6}$$

where

$$\psi = \sigma + V_x(x-\xi) + V_y(y-\eta), \tag{4.7}$$

and r and ϕ are polar coordinates based on the centre of the vortex,

$$r^2 = (x-\xi)^2 + (y-\eta)^2, \quad \phi = \tan^{-1}\left(\frac{y-\eta}{x-\xi}\right). \tag{4.8}$$

The vortex parameters a, width w, the phase σ, the position (ξ, η), the velocity (V_x, V_y) and the shelf height g all depend on the evolution variable z. The azimuthal angle is given by ϕ and the topological charge n is the number of windings around the phase singularity that are undertaken by the beam. A profile of this trial function for an optical vortex is shown in figure 4.3 by the solid red line and a 3D representation is shown in figure 4.4.

The first term in the trial function (4.6) represents the electric field of the optical vortex. Hence, the amplitude of the optical vortex is

$$A = \frac{aw}{\sqrt{2}} e^{-r^2/w^2} \tag{4.9}$$

and this peak amplitude occurs at the radius $r = w/\sqrt{2}$. It should be noted that the peak amplitude of the vortex is derived from the trial function (4.6) by finding the maximum value of E,

$$\frac{\partial E}{\partial r} = a\left(1 - \frac{2r}{w^2}\right) e^{-r^2/w^2} e^{i\psi + in\phi} = 0. \tag{4.10}$$

In this chapter we will only concern ourselves with vortices of charge 1, so that $n = 1$. This is shown in figure 4.2 where only one winding of phase around the singularity occurs.

The second term in the trial function (4.6) is related to the shelf of low wavenumber diffractive radiation that accumulates under the evolving vortex [60]. This radiation shelf can be clearly seen in figure 4.5. The existence of the shelf of radiation is shown by conducting a perturbation analysis by linearising the electric field equation (4.1) about the steady state [60, 73]. This shed radiation allows the vortex to evolve to its final steady state.

Finally, the shelf of low wavenumber radiation under the evolving vortex is $\pi/2$ out of phase with it [60]. The height of the shelf of radiation is denoted by g in equation (4.6). The shelf form under the vortex within the region $r_{min} \leq r \leq r_{max}$, where $r_{max,min} = w \pm R/2$ [53] and R is to be determined.

For a nematicon, the director perturbation can be approximated by a

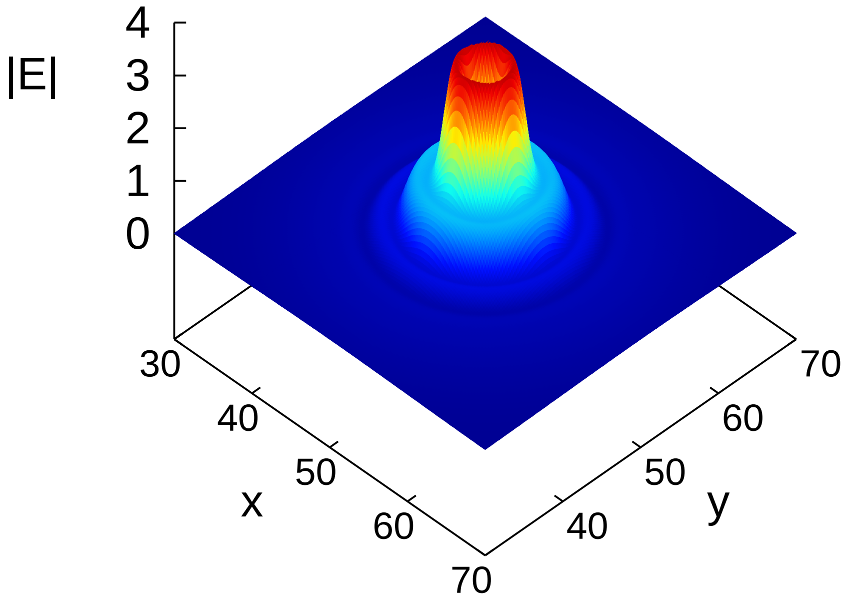

Figure 4.5: Evolution for $|E|$ of the vortex equations (4.1) and (4.2) at $z = 30$ for the initial condition (4.6) with $g = 0$ showing the shelf under the vortex.

sech^2 profile derived from the electric field, as was the case in Section 2.3.3, equation (2.25) [72, 74, 84]. This profile is found to simulate the behaviour observed numerically and experimentally of the liquid crystal under the influence of the light beam very well. However, in the case of a vortex, using a similar approximation for the director perturbation does not work, as the nonlocality smooths out its response near the central dip in the vortex, so that it does not have the same profile as the electric field. This is shown in figure 4.3 by the green dashed line, which shows the numerical solution for the director. To overcome the difficulty caused by the smoothing, the director equation (4.2) is solved exactly for θ using two alternative methods. The first method uses an eigenfunction expansion or Fourier series, while the second method uses a Green's function and the MoI. The director solution θ now contains an accurate representation of the logarithmic far field response of the nematic under the influence of the anchoring boundary conditions [44]. This approach of using an exact solution for the director response has been used for both a 1D cell [30] and a 2D cell [45] (Chapter 3), where excellent comparisons with the full numerical solutions were obtained in both cases.

The director equation (4.2) will now be solved using two methods: a Fourier series solution that corresponds to the Lagrangian given by equation (4.3) and a solution based on the MoI to determine the Green's function for the Laplacian in the Lagrangian (4.4).

Fourier series

An exact solution for the director equation (4.2) can be found using an eigenfunction expansion, a Fourier series, upon substituting the trial function for the electric field envelope E, equation (4.6) into the director equation. After neglecting the $O(g^2)$ contribution, the solution is

$$\theta = -\sum_{n,m=1}^{\infty} \frac{C_{nm}}{\pi^2 Q_1} \sin\left(\frac{n\pi x}{L_x}\right) \sin\left(\frac{m\pi y}{L_y}\right), \tag{4.11}$$

where

$$\begin{aligned} C_{nm} &= -\frac{8}{\nu L_x L_y} \int_0^{L_y} \int_0^{L_x} |E|^2 \sin\left(\frac{n\pi x}{L_x}\right) \sin\left(\frac{m\pi y}{L_y}\right) dx\, dy \\ &= -\frac{\pi a^2 w^4}{\nu L_x L_y} e^{-\gamma_1/2} (P_1 - \gamma_1) \sin\left(\frac{n\pi\xi}{L_x}\right) \sin\left(\frac{m\pi\eta}{L_y}\right). \end{aligned} \tag{4.12}$$

Here,

$$P_1 = 2 - \gamma_1, \quad Q_1 = \frac{n^2}{L_x^2} + \frac{m^2}{L_y^2}, \quad \gamma_1 = \frac{1}{4}\pi^2 w^2 Q_1. \tag{4.13}$$

The director solution (4.11) is now substituted into the corresponding Lagrangian (4.3), along with the trial function for the electric field E (4.6) and averaged over the NLC cell in the $x-y$ plane [39], resulting in the averaged Lagrangian

$$\begin{aligned} \mathcal{L} = &-4\left(\frac{a^2 w^4}{8} + g^2\Lambda_1\right)\left(\sigma' - V_x\xi' - V_y\eta' + \frac{V_x}{2} + \frac{V_y}{2}\right) \\ &- \sqrt{\pi} a g' w^3 + \sqrt{\pi} a' g w^3 + 3\sqrt{\pi} a g w^2 w' - a^2 w^2 \\ &- 2g^2\Lambda_2 + \sum_{n,m=1}^{\infty} \frac{\nu L_x L_y C_{nm}^2}{4\pi^3 Q_1}, \end{aligned} \tag{4.14}$$

where $\Lambda_1 = wR$ and $\Lambda_2 = \ln(r_{max}/r_{min})$.

Taking variations of the averaged Lagrangian (4.14) with respect to the vortex parameters gives the modulation equations describing the evolution of the vortex. These modulation equations are stated below and include the previously derived diffractive radiation shed as the vortex evolves towards the final steady state [60, 72, 74] (see Section 3.2.2)

$$\frac{d}{dz}\left[\frac{a^2w^4}{8}+g^2\Lambda_1\right]=-2\delta\tilde{\Lambda}\kappa^2, \tag{4.15}$$

$$\sqrt{\pi}\frac{d}{dz}\left(aw^3\right)-4g\Lambda_1\sigma'=-2g\Lambda_1\left(V_x^2+V_y^2\right)+2g\Lambda_2, \tag{4.16}$$

$$\xi'=V_x, \quad \eta'=V_y, \tag{4.17}$$

$$\begin{aligned}&\frac{d}{dz}\left[\left(\frac{a^2w^4}{8}+g^2\Lambda_1\right)V_x\right]=\\&\quad\frac{a^4w^8}{8\nu L_x^2L_y}\sum_{n,m=1}^{\infty}\frac{nP_1^2e^{-\gamma_1}}{Q_1}\sin\left(\frac{n\pi\xi}{L_x}\right)\cos\left(\frac{n\pi\xi}{L_x}\right)\sin^2\left(\frac{m\pi\eta}{L_y}\right),\end{aligned} \tag{4.18}$$

$$\begin{aligned}&\frac{d}{dz}\left[\left(\frac{a^2w^4}{8}+g^2\Lambda_1\right)V_y\right]=\\&\quad\frac{a^4w^8}{8\nu L_xL_y^2}\sum_{n,m=1}^{\infty}\frac{mP_1^2e^{-\gamma_1}}{Q_1}\sin^2\left(\frac{n\pi\xi}{L_x}\right)\sin\left(\frac{m\pi\eta}{L_y}\right)\cos\left(\frac{m\pi\eta}{L_y}\right),\end{aligned} \tag{4.19}$$

$$\begin{aligned}\frac{dg}{dz}=&-\frac{\sqrt{\pi}a^3w^7}{8\nu L_xL_y}\sum_{n,m=1}^{\infty}\left[\left(1+\frac{P_1}{2}\right)P_1e^{-\gamma_1}\sin^2\left(\frac{n\pi\xi}{L_x}\right)\sin^2\left(\frac{m\pi\eta}{L_y}\right)\right]\\&+\frac{a}{\sqrt{\pi}w}-2\pi^{3/2}\delta g,\end{aligned} \tag{4.20}$$

$$\begin{aligned}\frac{d\sigma}{dz}=&\frac{\pi a^2w^6}{4\nu L_xL_y}\sum_{n,m=1}^{\infty}\left[\left(1+\frac{P_1}{2}\right)P_1e^{-\gamma_1}\sin^2\left(\frac{n\pi\xi}{L_x}\right)\sin^2\left(\frac{m\pi\eta}{L_y}\right)\right]\\&+\frac{a^2w^4}{\pi\nu L_xL_y}\sum_{n,m=1}^{\infty}\frac{P_1^2e^{-\gamma_1}}{Q_1}\sin^2\left(\frac{n\pi\xi}{L_x}\right)\sin^2\left(\frac{m\pi\eta}{L_y}\right)\\&+\frac{1}{2}\left(V_x^2+V_y^2\right)-\frac{4}{w^2}.\end{aligned} \tag{4.21}$$

The loss coefficient δ is given by equation (3.29) and

$$\kappa^2 = \frac{1}{\tilde{\Lambda}}\left[\frac{1}{8}a^2w^4 - \frac{1}{8}\hat{a}^2\hat{w}^4 + \tilde{\Lambda}g^2\right]. \tag{4.22}$$

One major effect of nonlocality is to shift the point at which the vortex sheds diffractive radiation from the edge of the shelf $\sqrt{(x-\xi)^2+(y-\eta)^2} = \ell^2$ to a new radius $\tilde{\ell}$ from the vortex's position (ξ, η), which is the edge of the director response [72]. The radius for the radiation response is termed the outer shelf radius [72]. In the present case of a finite cell, the director response extends to a boundary layer at the cell walls [45], as for the nematicon of Chapter 3. Hence,

$$\tilde{\ell} = \min\left(\frac{L_x}{2}, \frac{L_y}{2}\right) \tag{4.23}$$

and therefore the outer area of the shelf is $\tilde{\Lambda} = \tilde{\ell}^2/2$. For a finite cell, the diffractive radiation is then shed in a boundary layer at the cell walls.

The final quantity required is the radius R of the shelf of low wavenumber radiation that accumulates under the vortex. For a vortex in an unbounded region, it was found that the radius was equal to the vortex width, $R = w$ [53]. However, in a bounded region, the shelf of radiation is affected by the cell walls, and this unbounded cell radius will not work. As the actual effect of the cell walls on the vortex and shelf is complicated and difficult to analyse, it was found easiest to set $R = \beta w$, with β to be determined. Then,

$$\Lambda_1 = \beta w^2, \quad \Lambda_2 = \ln\left(\frac{1+\beta/2}{1-\beta/2}\right). \tag{4.24}$$

A comparison of the modulation solution with the full numerical solution found that a value of $\beta = 0.2$ is robust for numerous input vortices.

The final steady state of the vortex for a given input beam can be found from total energy conservation for the system. This energy conservation equation is most easily found using Nöther's theorem based on the invariance of the Lagrangian (4.3) with respect to shifts in z (refer to Section 3.34 for an outline of the process). The averaged energy conservation equation can then be found by integrating this energy conservation equation in x and y over the cell, resulting in

$$\begin{aligned}\frac{dH}{dz} =& \frac{d}{dz}\int_0^{L_y}\int_0^{L_x}\left[|\nabla E|^2 - 2\theta|E|^2\right]\,dx\,dy\\ =& \frac{d}{dz}\left\{a^2w^2 + \sum_{n,m=1}^{\infty}\frac{\nu L_x L_y C_{nm}^2}{4\pi^3 Q_1}\right\} = 0. \end{aligned} \tag{4.25}$$

It was found that the cell boundaries act with a repulsive force towards the vortex [30, 45, 53]. As a result, the vortex traverses a spiral path towards the centre of the cell, where the repulsive forces exerted by the boundaries are in balance. Hence, at the steady state the vortex will be in the centre of the cell. The steady state is denoted using a carat ˆ. We then have $\hat{\xi} = L_x/2$, $\hat{\eta} = L_y/2$ with $V_x = 0$ and $V_y = 0$. Further, the vortex will have ceased shedding radiation at the steady state and hence the shelf height $\hat{g}$ will be zero. Thus, the modulation equation (4.20) can be used to find a relationship between the steady state amplitude $\hat{a}$ and width $\hat{w}$, which yields

$$\hat{a}^2 = \frac{8\nu L_x L_y}{\hat{w}^8}\left[\sum_{n,m=1}^{\infty}\left(1+\frac{P_1}{2}\right)P_1 e^{-\gamma_1}\right]^{-1}. \tag{4.26}$$

Hence, equations (4.25) and (4.26) can be used to determine the final steady state values of the amplitude $\hat{a}$ and width $\hat{w}$ for a given initial condition.

Method of images

The second method used to solve the director equation (4.2) is the MoI [92]. A point source is taken at (x', y') within the $x - y$ plane of the NLC cell. An infinite series of images is taken of this point, as shown in figure 3.2. The images are reflections of the point source, and are taken so that the Green's function satisfies the boundary condition $\theta = 0$ at the cell walls $x = 0, L_x$ and $y = 0, L_y$. The Green's function that satisfies these boundary conditions is [92]

$$G = -\frac{1}{2\pi}\mathbf{Re}\left\{\ln\left[\frac{\sigma(t-\tau,x,y)\sigma(t+\tau,x,y)}{\sigma(t-\tau^*,x,y)\sigma(t+\tau^*,x,y)}\right]\right\}, \tag{4.27}$$

where

$$\sigma(\upsilon,x,y) = \upsilon\prod_{\omega\neq 0}\left[\left(1-\frac{\upsilon}{2\omega}\right)e^{\upsilon/(2\omega)+\upsilon^2/(8\omega)^2}\right] \tag{4.28}$$

is the Weierstrass σ function. Here, t and τ are the complex coordinates $t = x + iy$ and $\tau = x' + iy'$, respectively. Finally, υ is complex valued and

$$\omega = nL_x + mL_y, \quad n = 0, \pm 1, \dots, \quad m = 0, \pm 1, \dots. \tag{4.29}$$

The Green's function (4.27) is obtained by mapping the Green's function for the half plane onto the rectangle $[0, L_x] \times [0, L_y]$ using the elliptic function σ [92]. The director angle θ solution (4.5) is then found by substituting in the Green's function, equation (4.27).

The usual experimental regime for nonlinear optics in liquid crystals is the nonlocal one where ν is large, that is, $\nu = O(100)$ [26]. In this limit, the director distribution is slowly varying on a length scale $O(\sqrt{\nu})$, so that relative to the director, the vortex can be treated as a Dirac delta function. Using this approximation for the vortex, $|E|^2$, in the Green's function solution (4.5) for the director θgives the perturbation of the director angle as

$$\theta = -\frac{a^2 w^4}{2\nu} \mathbf{Re} \left\{ \ln \frac{\sigma(t-\zeta)\sigma(t+\zeta)}{\sigma(t-\zeta^*)\sigma(t+\zeta^*)} \right\}, \tag{4.30}$$

where $\zeta = \xi + i\eta$, as was found for the nematicon of Chapter 3. This solution for θ and the trial function, equation (4.6), are now substituted into the Lagrangian (4.4), which is then integrated over x and y to find the averaged Lagrangian [39]

$$\begin{aligned} \mathcal{L} = &-\sqrt{\pi} a g' w^3 + \sqrt{\pi} a' g w^3 + 3\sqrt{\pi} a g w^2 w' - a^2 w^2 - 2g^2 \Lambda_2 \\ &- 4\left(\frac{a^2 w^4}{8} + g^2 \Lambda_1\right)\left(\sigma' - V_x \xi' - V_y \eta' + \frac{V_x^2}{2} + \frac{V_y^2}{2}\right) \\ &- \frac{a^4 w^8}{8\nu}\left[\Delta_1 + \Delta_2 - \Delta_3 - \Delta_4\right]. \end{aligned} \tag{4.31}$$

Here,

$$\Delta_1 = \ln \frac{w}{\sqrt{2}} + \frac{1-\gamma}{2} - \ln 2 + \ln \sqrt{\xi^2+\eta^2} - \ln\left(\xi\eta\right), \tag{4.32}$$

$$\begin{aligned}\Delta_2 = \sum_{n,m=-\infty}^{\infty} &\left[\frac{1}{2}\ln \frac{\left(nL_x-\xi\right)^2 + \left(mL_y-\eta\right)^2}{n^2L_x^2+m^2L_y^2}\right. && (4.33)\\ &+ \left.\frac{\left(\xi^2-\eta^2\right)\left(n^2L_x^2-m^2L_y^2\right) + 4nm\xi\eta L_xL_y}{2\left(n^2L_x^2+m^2L_y^2\right)^2}\right], && (4.34)\end{aligned}$$

$$\Delta_3 = \sum_{n,m=-\infty}^{\infty} \left[\frac{1}{2}\ln \frac{n^2L_x^2 + \left(mL_y-\eta\right)^2}{n^2L_x^2+m^2L_y^2} - \frac{\eta^2\left(n^2L_x^2-m^2L_y^2\right)}{2\left(n^2L_x^2+m^2L_y^2\right)^2}\right], \tag{4.35}$$

$$\Delta_4 = \sum_{n,m=-\infty}^{\infty} \left[\frac{1}{2}\ln \frac{\left(nL_x-\xi\right)^2 + m^2L_y^2}{n^2L_x^2+m^2L_y^2} + \frac{\xi^2\left(n^2L_x^2-m^2L_y^2\right)}{2\left(n^2L_x^2+m^2L_y^2\right)^2}\right], \tag{4.36}$$

and γ is Euler's constant, $\gamma = 0.577215665\ldots$ [75]. Also, Λ_1 and Λ_2 maintain the values stated in section 4.2.2, equation (4.24), and the same value of $\beta = 0.2$ remains a robust fit for a wide variety of input vortices.

Using the Euler–Lagrange equation (2.18) and taking variations of the averaged Lagrangian equation (4.31) with respect to the vortex parameters yields the modulation equations describing the vortex evolution. To these are added loss terms to account for the effect of the shed diffractive radiation (see Section 3.2.2 for an explanation) these equations are

$$\frac{d}{dz}\left[\frac{a^2w^4}{8} + g^2\Lambda_1\right] = -2\delta\tilde{\Lambda}\kappa^2, \tag{4.37}$$

$$\sqrt{\pi}\frac{d}{dz}\left(aw^3\right) - 4g\Lambda_1\frac{d\sigma}{dz} = -2g\Lambda_1\left(V_x^2+V_y^2\right) + 2g\Lambda_2, \tag{4.38}$$

$$\xi' = V_x, \quad \eta' = V_y, \tag{4.39}$$

$$\begin{aligned}\frac{d}{dz}\left[\left(\frac{a^2w^4}{8} + g^2\Lambda_1\right)V_x\right] &= \frac{a^4w^8\eta^2}{32\nu\xi\left(\xi^2+\eta^2\right)} \\ &+ \frac{a^4w^8}{32\nu}\sum_{n,m=-\infty}^{\infty}\left[\frac{(nL_x-\xi)}{\left(nL_x\xi\right)^2+\left(mL_y-\eta\right)^2}\right. \\ &- -\frac{2nm\eta L_xL_y}{\left(n^2L_x^2+m^2L_y^2\right)^2} - \left.\frac{(nL_x-\xi)}{\left(nL_x-\xi\right)^2+m^2L_y^2}\right],\end{aligned} \tag{4.40}$$

$$\begin{aligned}\frac{d}{dz}\left[\left(\frac{a^2w^4}{8} + g^2\Lambda_1\right)V_y\right] &= \frac{a^4w^8\xi^2}{32\nu\eta\left(\xi^2+\eta^2\right)} \\ &+ \frac{a^4w^8}{32\nu}\sum_{n,m=-\infty}^{\infty}\left[\frac{(mL_y-\eta)}{\left(nL_x-\xi\right)^2\left(mL_y-\eta\right)^2}\right. \\ &+ -\frac{2nm\xi L_xL_y}{\left(n^2L_x^2+m^2L_y^2\right)^2} - \left.\frac{(mL_y-\eta)}{n^2L_x^2+\left(mL_y-\eta\right)^2}\right],\end{aligned} \tag{4.41}$$

$$\frac{dg}{dz} = \frac{a}{\sqrt{\pi}w} - \frac{a^3w^5}{16\sqrt{\pi}\nu} - 2\delta g, \tag{4.42}$$

$$\frac{d\sigma}{dz} = \frac{1}{2}\left(V_x^2+V_y^2\right) - \frac{4}{w^2} - \frac{a^2w^4}{2\nu}\left[\Delta_1+\Delta_2-\Delta_3-\Delta_4-\frac{1}{4}\right]. \tag{4.43}$$

Again, the loss coefficient δ is given by equation (3.29) and κ by equation (4.22). The modulation equation (4.37) is the equation for conservation of mass (optical power) and equations (4.40) and (4.41) are those for conservation of x and y momentum, respectively. The primary concern of the present work is the trajectory of the vortex, which is given by the modulation equations (4.39), (4.40) and (4.41).

As with the Fourier series analysis, the final steady state values can be found using total energy conservation for the system. An application of Nöther's theorem (equation (3.34)) based on the invariance of the Lagrangian for the MoI (4.4) with respect to shifts in z results an equation for total energy conservation. Averaging this energy conservation equation by integrating in x and y over the cell, gives the averaged energy conservation equation

$$\begin{aligned}\frac{dH}{dz} =& \frac{d}{dz}\int_0^{L_y}\int_0^{L_x}\left[|\nabla E|^2 - 2\theta|E|^2\right]\,dx\,dy\\ =& \frac{d}{dz}\left\{a^2w^2 + \frac{a^4w^8}{8\nu}\left[\Delta_1+\Delta_2-\Delta_3-\Delta_4\right]\right\} = 0. \end{aligned} \tag{4.44}$$

The steady state relationship between the amplitude $\hat{a}$ and width $\hat{w}$ can be found from equation (4.42) to be

$$\hat{a}^2 = \frac{16\nu}{\hat{w}^6} \tag{4.45}$$

on setting $g = 0$. Using the same argument as for the Fourier series, equations (4.44) and (4.45) are used to determine the final steady state values of the amplitude $\hat{a}$ and width $\hat{w}$ for a given input vortex.

4.2.3 Stability analysis

Vortices are unstable in local media [50, 97, 98, 107]. However, in nonlocal media, vortices are stable for high enough nonlocality [52, 53]. These results are for a vortex propagating in infinite region. This section is dedicated to the study of how the interaction of a vortex with a boundary can change the stability of a vortex even in a nonlocal medium for which the nonlocality is high enough to guarantee stability away from the boundary. The linearised

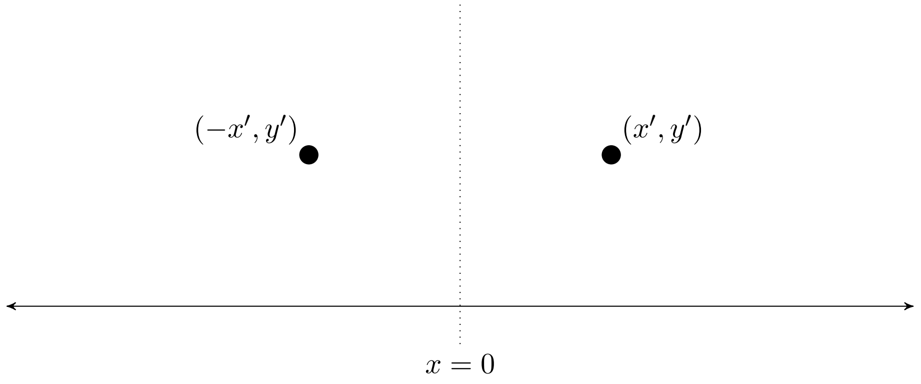

Figure 4.6: A picture of the half-plane, showing the point source at (x', y') and the reflection at the boundary $(-x', y')$.

stability analysis conducted here will make use of the MoI. To simplify the stability analysis, let us assume that the vortex is close enough to one of the cell walls such that the effect of the other three boundaries on the vortex are negligible. Let us take this wall to be the plane where $x = 0$. To calculate the Green's function for this simplified geometry, a point source (x', y') is taken within the half plane, $x > 0$. Hence, the boundary condition, $\theta = 0$ at $x = 0$ is satisfied by taking a point sink at the image point of the source $(-x', y')$. Figure 4.6 shows the point source and its reflection about this plane. Using this newly constructed Green's function, an appropriate averaged Lagrangian can be calculated from the governing equations (4.1) and (4.2). However, the calculation of this averaged Lagrangian differs from those previously calculated throughout this thesis. The stability of the vortex is dependent on the azimuthal angle ϕ around the circumference of the vortex, as a vortex becomes unstable via a symmetry-breaking azimuthal instability which splits the vortex in two [52, 53]. Hence, the stability analysis needs to account for this, and as a result the vortex parameters need to vary independently with respect to z and ϕ. Therefore, the Green's function for the half plane with zero boundary condition on the wall $x = 0$ is [92]

$$G = -\frac{1}{2\pi}\left[\ln\sqrt{(x-x')^2+(y-y')^2} - \ln\sqrt{(x+x')^2+(y-y')^2}\right]. \quad (4.46)$$

The trial function for the electric field E remains the same as in (4.6). However, for the stability analysis all the parameters are dependent on z and ϕ (for example, $a = a(z, \phi)$). The director angle for the half plane can be calculated by substituting the Green's function (4.46) and the trial function for the electric field E (4.6) into the Green's function solution for θ equation (4.5). Now, using the previously discussed asymptotic Dirac delta function approximation for the electric field relative to the director (valid in the nonlocal limit) to evaluate the resulting integral in equation (4.5) yields

$$\theta = -\frac{a^2w^4}{4\nu}\left[\ln\frac{w}{\sqrt{2}} + \frac{1-\gamma}{2} - \ln\sqrt{(x+\xi)^2+(y-\eta)^2}\right]. \quad (4.47)$$

Due to the new dependence on the polar angle ϕ, the Lagrangian for the governing equations (4.1) and (4.2) is now

$$L = i(E^*E_z - EE_z^*) - |E_r|^2 - \frac{|E_\phi|^2}{r^2} + 2\theta|E|^2. \quad (4.48)$$

After substituting the trial function E (4.6) and the exact solution θ for the half plane (4.47) into the Lagrangian (4.48) the averaged Lagrangian is found by integrating in x and y over the half plane $x > 0$, which results in

$$\begin{aligned}\mathcal{L} = &-\sqrt{\pi} a g_z w^3 + \sqrt{\pi} a_z g w^3 + 3\sqrt{\pi} a g w^2 w_z + 2\sqrt{\pi} a_\phi g w \\ &+ 2\sqrt{\pi} a g w_\phi - 2\sqrt{\pi} a g_\phi w - a^2 w^2 - \frac{a_\phi^2 w^2}{2} - a^2 w_\phi^2 - 2g^2\Lambda_2 \\ &- a w a_\phi w_\phi - 2g_\phi^2 \Lambda_2 - \frac{a^4 w^8}{8\nu}\left(\ln\frac{w}{\sqrt{2}} + \frac{1-\gamma}{2} - \ln 2\xi\right) \\ &- 4\left(\frac{a^2 w^4}{8} + g^2\Lambda_1\right)\left(\sigma_z - V_x\xi_z - V_y\eta_z + \frac{V_x}{2} + \frac{V_y}{2}\right). \qquad (4.49)\end{aligned}$$

Noted that the phase σ is taken to be a function of z alone due to w and g being conjugate variables governing the stability of the vortex. Hence, σ as a function of z only does not affect the linearised stability analysis [53].

The expressions (4.24) for the shelf remain valid. An extension of the Euler–Lagrangian equation to two variables (z, ϕ) is required so as to calculate the modulation equations. The extended Euler–Lagrange equation is given by

$$\frac{\partial L}{\partial h_i} - \frac{d}{dz}\frac{\partial L}{\partial h_{i,z}} - \frac{d}{d\phi}\frac{\partial L}{\partial h_{i,\phi}} = 0, \qquad (4.50)$$

where the vortex parameters $h_i(z, \phi)$, $i = 1 \ldots n$, are now dependent upon z and ϕ. Also, $h_{i,z}$ and $h_{i,\phi}$ represent the derivatives with respect to z and ϕ, respectively. The resulting modulation equations are then

$$\frac{d}{dz}\left[\frac{a^2 w^4}{8} + g^2\Lambda_1\right] = 0, \qquad (4.51)$$

$$\begin{aligned}\sqrt{\pi}\left(a w^3\right)_z + 2\sqrt{\pi}\left(a w\right)_\phi = &4g\Lambda_1\left(\sigma_z - V_x\xi_z - V_y\eta_z + \frac{V_x^2}{2} + \frac{V_y^2}{2}\right) \\ &- 2\Lambda_2\left(g_{\phi\phi} + g\right), \qquad (4.52)\end{aligned}$$

$$\frac{d\xi}{dz} = V_x, \quad \frac{d\eta}{dz} = V_y, \tag{4.53}$$

$$\frac{d}{dz}\left[\left(\frac{a^2w^4}{8} + g^2\Lambda_1\right)V_x\right] = \frac{a^4w^8}{32\nu\xi}, \tag{4.54}$$

$$\frac{d}{dz}\left[\left(\frac{a^2w^4}{8} + g^2\Lambda_1\right)V_y\right] = 0, \tag{4.55}$$

$$\sqrt{\pi}\frac{dg}{dz} = \frac{a}{w} + \frac{aw_\phi^2}{w^3} + \frac{2\sqrt{\pi}g_\phi}{w^2} - \frac{a_{\phi\phi}}{2w} - \frac{a^3w^5}{16\nu}, \tag{4.56}$$

$$\begin{aligned}\frac{d\sigma}{dz} =& \frac{1}{2}\left(V_x^2 + V_y^2\right) - \frac{4}{w^2} - \frac{3w_\phi^2}{w^4} + \frac{2a_\phi w_\phi}{aw^3} - \frac{8\sqrt{\pi}g_\phi}{a^2w^3} + \frac{2a_{\phi\phi}}{aw^2} \\ &+ \frac{w_{\phi\phi}}{w^3} - \frac{a^2w^4}{2\nu}\left(\ln\frac{w}{\sqrt{2}} + \frac{1-2\gamma}{4} - \ln 2\xi\right).\end{aligned} \tag{4.57}$$

A linearised stability analysis about the steady state is now conducted to find the minimum distance of approach of the vortex to the boundary before it becomes unstable. We perturb about the steady state with

$$a = \hat{a} + a_1, \quad w = \hat{w} + w_1 \quad \text{and} \quad g = \hat{g} + g_1 = g_1, \tag{4.58}$$

since $\hat{g} = 0$ at the steady state. The modulation equations (4.51), (4.52), (4.56) and (4.57) are linearised using the perturbations given in equation (4.58), yielding the following linearised equations

$$\frac{d}{dz}\left[\frac{(\hat{a}+a_1)^2(\hat{w}+w_1)^4}{8}\right] = 0, \tag{4.59}$$

$$\begin{aligned}6\sqrt{\pi}\hat{a}\hat{w}^2\frac{dw_1}{dz} &+ 2\sqrt{\pi}\hat{w}\frac{da_1}{dz} + 4\sqrt{\pi}\hat{a}\frac{da_1}{d\phi} + 4\sqrt{\pi}\hat{w}\frac{\partial a_1}{\partial\phi} - 8g_1\Lambda_1\frac{\partial\sigma}{\partial z} + 4\Lambda_2\frac{\partial^2 g_1}{\partial\phi^2} \\ &= -4g_1\Lambda_1\left(V_x^2 + V_y^2\right) + 4g_1\Lambda_2,\end{aligned} \tag{4.60}$$

$$\sqrt{\pi}\frac{\partial g_1}{\partial z} - \frac{2\sqrt{\pi}}{\hat{w}^2}\frac{\partial g_1}{\partial \phi} + \frac{1}{2\hat{w}}\frac{\partial^2 a_1}{\partial \phi^2} = \frac{\hat{a}}{\hat{w}} - \frac{\hat{a}^3\hat{w}^5}{16\nu} - \frac{\hat{a}w_1}{\hat{w}^2} + \frac{a_1}{\hat{w}} - \frac{5\hat{a}^3\hat{w}^4 w_1}{16\nu}$$
$$- \frac{3\hat{a}^2\hat{w}^5 a_1}{16\nu}. \tag{4.61}$$

$$\frac{\partial \hat{\sigma}}{\partial z} = \frac{1}{2}\left(V_x^2 + V_y^2\right) - \frac{2}{\hat{w}^2} - \frac{\hat{a}^2\hat{w}^4}{2\nu}\left(\ln\frac{\hat{w}}{\sqrt{2}} + \frac{1-\gamma}{2} - \ln 2\xi\right) \tag{4.62}$$

Perturbation terms of quadratic order and higher have been neglected, that is, $O(a_1^2)$, $O(w_1^2)$ and $O(g_1^2)$ terms.

Modal solutions of the linearised equations (4.60) and (4.61) are sought of the form

$$w_1 = We^{i(\lambda z + \rho\phi)}, \quad g_1 = Ge^{i(\lambda z + \rho\phi)}, \tag{4.63}$$

where ρ is the azimuthal wavenumber of the vortex [53], and $\rho = 1, 2, \ldots$. The linearised mass equation (4.59) gives a relationship between the perturbation amplitude a_1 and width w_1

$$a_1 = -\frac{2\hat{a}}{\hat{w}}w_1. \tag{4.64}$$

After some algebra, the linearised modulation equations (4.60) and (4.61) can be written in the form of a determinant to find the stability eigenvalues λ

$$\begin{vmatrix} i\sqrt{\pi}\left(\lambda - \frac{2\rho}{\hat{w}^2}\right) & \hat{a}M_1 \\ 4M_2 & i2\sqrt{\pi}\hat{a}\left(\hat{w}^2\lambda - 2\rho\right) \end{vmatrix} = 0. \tag{4.65}$$

Here

$$M_1 = \frac{3}{\hat{w}^2} + \frac{\rho^2}{\hat{w}^2} - \frac{\hat{a}^2\hat{w}^4}{16\nu}, \tag{4.66}$$

$$M_2 = \frac{4\Lambda_1}{\hat{w}^2} + \frac{\hat{a}^2\hat{w}^4\Lambda_1 K_1}{\nu} - \left(1+\rho^2\right)\Lambda_2, \tag{4.67}$$

$$K_1 = \ln\frac{\hat{w}}{\sqrt{2}} + \frac{1-\gamma}{2} - \ln 2\xi. \tag{4.68}$$

This yields the eigenvalues λ given by

$$\lambda = \frac{4\pi\rho \pm \sqrt{-8\pi\hat{w}^2 M_1 M_2}}{2\pi\hat{w}^2}. \tag{4.69}$$

The vortex is unstable when $M_1M_2 > 0$, with the borderline cases occurring when $M_1 = 0$ and $M_2 = 0$. We are interested in the minimum distance of approach to the boundary which causes instability in the vortex. As M_1 does not involve the distance parameter ξ, we proceed to study M_2 only. We can thus determine the minimum distance of approach of the vortex to the wall at which instability sets in from equation (4.67) as determined by

$$M_2 = \frac{4\Lambda_1}{\hat{w}^2} + \frac{\hat{a}^2\hat{w}^4\Lambda_1 K_1}{\nu} - \left(1+\rho^2\right)\Lambda_2 = 0. \tag{4.70}$$

This leads to the formula

$$\xi_{min} = \frac{1}{2}e^{-\varsigma}, \tag{4.71}$$

where

$$\varsigma = \frac{\nu}{\hat{a}^2\hat{w}^4\Lambda_1}\left[-\frac{4\Lambda_1}{\hat{w}^2} + (1+\rho^2)\Lambda_2\right] - \ln\frac{\hat{w}}{\sqrt{2}} - \frac{1-\gamma}{2}. \tag{4.72}$$

The vortex is stable for distances ξ for which $M_1M_2 < 0$. In previous studies of vortices propagating in an infinite NLC, it was found that the most unstable mode was given by $\rho = 2$ [52, 53]. For the present finite nematic cell, the same is true for $\rho = 2$, as the stability eigenvalue given by equation (4.69) shows a maximum when $\rho = 2$ for $M_1 M_2 > 0$. This is in agreement with the full numerical solutions which show the vortex splits into two beams when it becomes unstable on approach to a wall. This will be discussed further in the next section. Additionally, the value of ρ is insensitive to the value of β in the calculation. Hence, $\rho = 2$ will be used in the minimum distance expression (4.71) for comparison with full numerical solutions in the next section.

In the above stability calculation, resulting in the distance expression (4.71), it should be noted that the distance ξ given in the trial function (4.6) is considered fixed. This has allowed a simple expression (4.71) for the minimum distance of approach to be found. If the distance were allowed to vary the stability analysis would become much more involved, with no equivalent simple expression to (4.71) being found.

The vortex becomes highly distorted upon approach to the boundary, as will be shown in the full numerical solutions. This is expected, and hence, the fixed trial function for the vortex profile ceases to be valid close to the wall. Hence, including a distance perturbation in the analysis still would not capture the complete dynamical process. The expression (4.71) will be found to be in reasonable accord with the full numerical solutions, even given the approximations described in this section. Therefore, this represents a balance between simplicity and capturing the full details, a point mentioned by Malomed [59] and in Chapter 2.

4.3 Results

In this section, we will compare full numerical solutions of the governing equations (4.1) and (4.2) with those of the modulation equations found using both the Fourier series and the MoI methods for the director equation (4.2). The modulation equations for each solution, given in section 4.2.2, were solved using the standard RK4 method, as described in Section 2.3.5. The full numerical solution for the governing equations (4.1) and (4.2) was obtained using the numerical scheme outlined in Section 2.4, where the trial function (4.6) with $g = 0$ forms the initial condition for the optical beam's electric field E.

To satisfy the stability criteria and maintain accuracy, the numerical step sizes used were $\Delta x = \Delta y = 0.2$ and $\Delta z = 0.001$. The propagation length was taken to be $z = 500$, which is a typical non-dimensional cell length [26]. The numerical investigation was first conducted on a square cell with a non-dimensional width and breadth of $(L_x, L_y) = (100, 100)$.

4.3.1 Stable vortex propagation - results

Consider the propagation of a stable vortex which is sufficiently far from the cell walls so that it does not become unstable. The vortex's behaviour within a finite NLC cell will be compared and contrasted to that of a nematicon given in Chapter 3 [45].

An optical vortex displays the same "bouncing" experienced by a nematicon as the boundary acts as a repulsive force on both optical beams [43, 45]. The vortex is also stable when it is sufficiently far from the cell walls, as was found in previous studies for a circular cell [46, 88]. The input parameters for the optical vortex were chosen so that the minimum power requirements for existence were met, while remaining below the threshold at which the vortex will split into two beams.

Figure 4.7 shows a typical comparison between the full numerical solution and both Fourier and MoI modulation solutions. In previous studies, the first harmonic of the Fourier series solution has been used to compare the path taken by a nematicon to the experimental trajectory, with the first term giving an adequate approximation [93]. In Chapter 3, this idea was taken further, by looking at the MoI solution and using only the fundamental images neighbouring the point source to construct the trajectory for a nematicon, with very good results obtained [45]. The same idea will be used in this chapter for a vortex, where the eight images surrounding the point source will be used to approximate the evolution of the vortex, with the obvious advantage being the number of calculations required to compute an accurate solution compared to the full series the Fourier series solution. Figure 3.2 shows the first eight images and the point source. In figure 4.7(a) comparisons of the vortex amplitude A are shown. From this figure it can

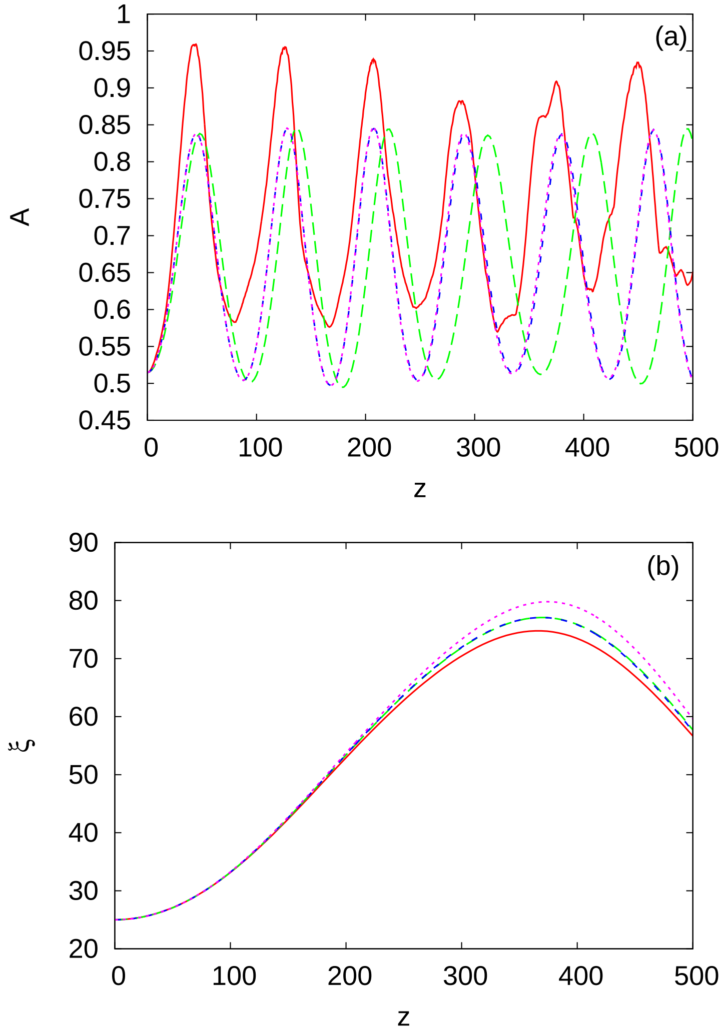

Figure 4.7: Comparison between the full numerical solution (red solid line), Fourier series solution (green dashed line), MoI solution (blue dot-dashed line), and MoI solution including only the first eight images (magenta dotted line) for (a) amplitude A and (b) x position for a square cell. The initial values are $a = 0.15$, $A = 0.52\ldots$, $w = 8$, $(\xi, \eta) = (25, 20)$, and $(V_x, V_y) = (0, 0)$, with $\nu = 200$ and $(L_x, L_y) = (100, 100)$.

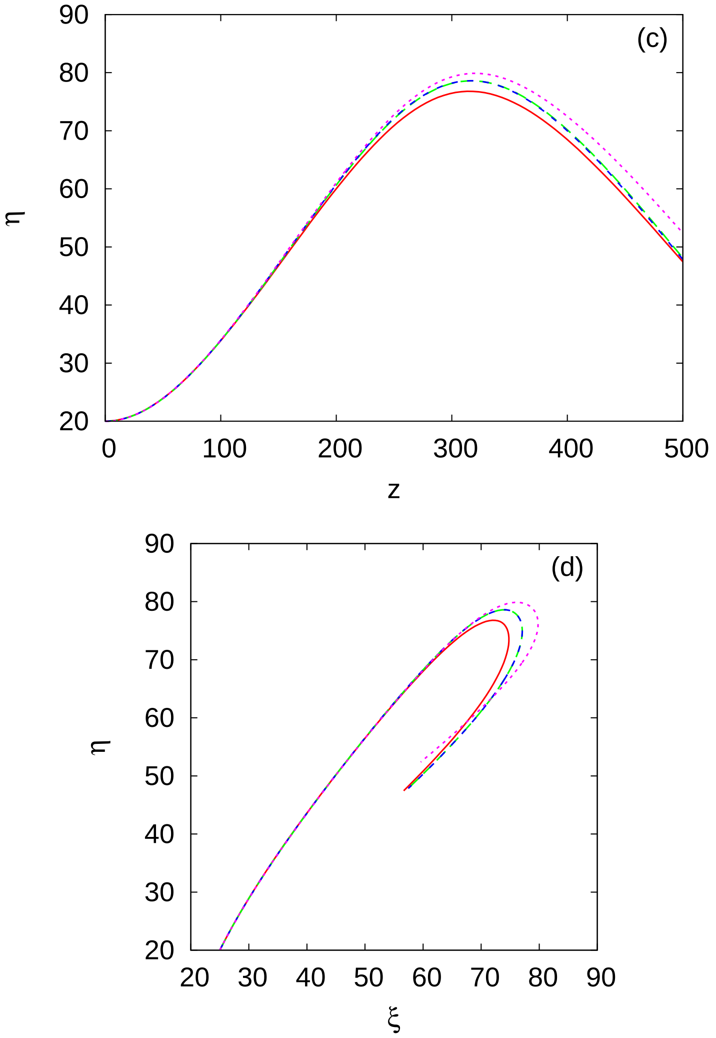

Figure 4.7: Comparison between the full numerical solution (red solid line), Fourier series solution (green dashed line), MoI solution (blue dot-dashed line), and MoI solution including only the first eight images (magenta dotted line) for (c) y position, and (d) (x, y) position for a square cell. The initial values are $a = 0.15$, $A = 0.52\ldots$, $w = 8$, $(\xi, \eta) = (25, 20)$, and $(V_x, V_y) = (0, 0)$, with $\nu = 200$ and $(L_x, L_y) = (100, 100)$.

be seen that using the first eight images is all that is necessary to obtain good agreement for the vortex amplitude with the full numerical solution, with no discernible difference with the MoI solution calculated using 10 200 images.

As the vortex propagates further through the NLC cell, a period difference is noticeable between the Fourier series solution and the MoI, as well as with the full numerical solution period, with the periods of the later two in agreement. The MoI and Fourier series solutions use different approximations to calculate the corresponding modulation equations, which accounts for the difference in the periods between them.

The amplitude found from the full numerical solution shows a more complicated behaviour, which is not evident in either of the modulation solutions. This is due to the deformation of the vortex upon interaction with the boundary. This can be verified by comparison of the numerical amplitude with the vortex's position in figure 4.7(d), which shows that the distortions occur when the vortex is close to the boundary. These distortions at the boundaries cannot be captured by the fixed trial function (4.6).

Figures 4.7(b) and (c) show a comparison for the trajectory components ξ and η as functions of z, respectively. It can be seen that both modulation solutions give identical results that are in excellent agreement with the full numerical trajectory. The reason lies in the fact that the amplitude-width and position-velocity oscillations of nonlinear beams in NLC's decouple [42, 85, 86, 105]. Hence, the amplitude of the two solutions can differ, but the position can agree. Again, it is noted that the fundamental images for the MoI solution give an excellent comparison with the full numerical position. This further confirms the superiority of the MoI over the traditional Fourier series solutions, as first suggested in reference [45]. Figure 4.7(d) shows the helical trajectory of the vortex as it propagates through the NLC cell, taking the z direction to be into the page. As stated previously, the repulsive nature of the cell walls can be clearly seen. The initial motion of the vortex is solely due to the repulsive behaviour of the cell walls, as the vortex was not given an initial velocity. Thus, if the interaction of the vortex with the cell walls does not upset the phase singularity, stability of the vortex will be maintained, and the vortex will be repelled away from the cell wall, as was the case for a vortex in a circular cell [46, 88]. Figure 4.7(d) confirms the conclusions drawn from figures 4.7(b) and 4.7(c), that is, both modulation solutions are in agreement and are in excellent agreement with the numerical solution and the first eight nearest neighbour images give an excellent approximation to the vortex trajectory.

4.3.2 Instability, minimum distance - results

A comparison between the analytical minimum stable distance of approach to the boundary, given by equation (4.71), and minimum stable distance of approach as given by the full numerical solution is shown in figure 4.8. In this

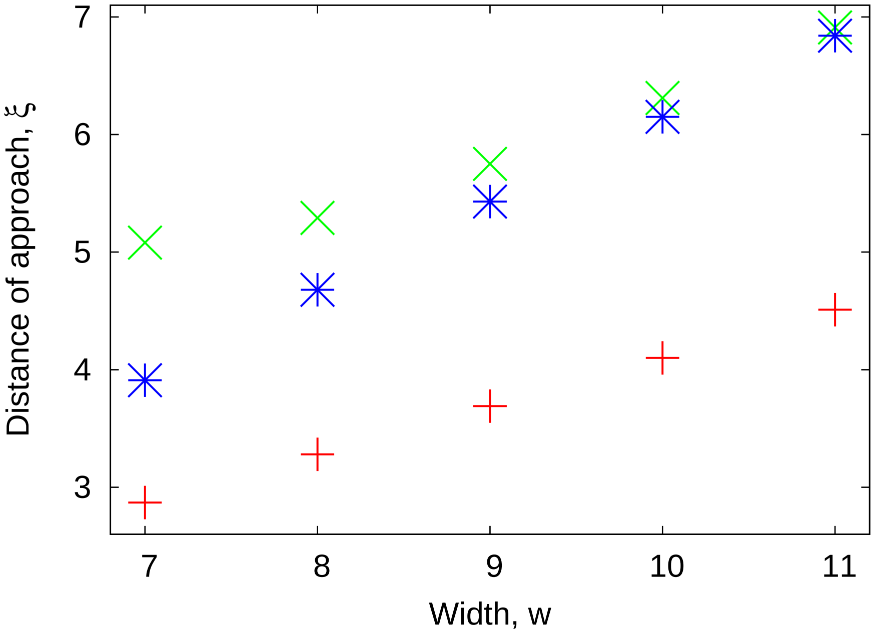

Figure 4.8: A comparison between the analytical stability boundary (4.71)(red plus sign $+$) with the full numerical solution (green crosses $\times$) for $(V_x, V_Y) = (0.8, 0)$ and the full numerical solution (blue stars, $*$) for $(V_x, V_y) = (1.5, 0)$. The numerical stability boundary is the distance from the boundary at which instability first occurs. The initial conditions used were a given by equation (4.73), $(\xi, \eta) = (50, 100)$ for $(L_x, L_y) = (100, 200)$.

figure, the stability boundary is shown as a function of the initial width w of the vortex for two different initial velocities, these being, $(V_x, V_y) = (0.8, 0)$ and $(V_x, V_y) = (1.5, 0)$.

The stability boundary, equation (4.71), was found using a small perturbation from the steady vortex. In order to obtain a comparison with this expression, the numerical solution must also initially start near a steady vortex. The modulation equation (4.56) gives the steady state amplitude-width relationship as

$$\hat{a}^2\hat{w}^6 = 16\nu. \tag{4.73}$$

Given an initial vortex width, this equation was used to determine the initial amplitude for the comparisons in figure 4.8. Note that the cell dimensions and initial positions were chosen to mirror the analytical description, that is, close enough to one of the cell walls, yet sufficiently far from the other three walls so that there is no effect on the vortex. The analytical and numerical minimum distances are in reasonable agreement for all initial widths, but the smaller widths are in better agreement for the higher initial velocity. This comparison shows that the assumptions used in section 4.2.3 for the linearised stability analysis are reasonable.

The numerical solutions show that the minimum distance of approach is only weakly dependent on the initial velocity, particularly at larger initial widths. The main cause of the differences between the minimum distance of approach as given by the linearised stability analysis and the full numerical solutions is the deformation that the leading edge of the vortex undergoes as it interacts with the boundary. The trial function E, given by equation (4.6), does not take into account this distortion of the vortex during interaction with a boundary, other than changes in its amplitude and width for a fixed functional form.

Figure 4.9 shows the numerical evolution of the vortex for a typical case for which the vortex approaches closer than the minimum distance and is reflected, breaking up into two nematicons. The large deformation of the vortex, particularly at the leading edge, can be clearly seen in figure 4.9(c). Here, the anchoring boundary condition fixing $\theta = 0$ at the cell wall induces the instability of the vortex. It has been shown that the nonlocality of NLC lifts the director angle θ sufficiently above zero under the centre of the vortex, to stabilise it [52]. At the boundary, the anchoring boundary condition forces θ to zero, which has the effect of making the NLC act like a local medium there, for which vortices are unstable to a mode 2 symmetry-breaking azimuthal instability [53]. We note that in a local medium the director perturbation is zero at the vortex core [53].

A further complication in the analytic and full numerical comparison is that the numerical vortex's position in calculated at its centre of mass. That is,

$$\xi = \frac{\int_0^{L_y} \int_0^{L_x} x|E|^2 \, dx \, dy}{\int_0^{L_y} \int_0^{L_x} |E|^2 \, dx \, dy}. \tag{4.74}$$

This is clearly the centre (phase singularity) of the vortex when it is symmetric. However, the distortion of the vortex when it interacts with the boundary (as shown in figure 4.9), implies that the centre of mass has shifted and no longer coincides with the phase singularity of the vortex which is the position of the vortex as given by the modulation equations. This accounts for some of the differences seen in the comparisons of the analytical expression for the position of the vortex given by equation (4.74) and the full numerical solutions seen in figure 4.7. Finally, figure 4.9(f) shows that the result of the instability of the vortex is it splits in two, forming two nematicons. These nematicons are stable, unlike in a local medium [50, 99]. The stability of the two nematicons is due to the nonlocality of the nematic response, which extends far beyond the waist of the electric field (see figure 4.3) and acts as an attractive potential. This attraction of nonlinear beams in (nonlocal) NLCs is in accord with experimental observations [47, 48] and theoretical results [83, 108].

4.4 Discussion

In this chapter we have studied the propagation of an optical vortex solitary wave in a finite nematic liquid crystal cell. A Lagrangian formulation of the governing equations was used in conjunction with a hybrid of a trial function and an exact solution to model the evolution of the vortex. The director equation was solved exactly, using two different, but equivalent methods, the method of images and a Fourier sine series. Both of these methods produced modulation equations whose solutions were in good agreement with the full numerical solutions. However, the MoI proved to be far superior and computationally more efficient as only the fundamental eight images surrounding the point source were needed to gain good agreement. This confirms the prediction stated in Chapter 3 [45] that the MoI is a powerful tool and an excellent alternative to Fourier series solutions for the director distribution.

The MoI was also used to analyse the stability of the vortex at a boundary, in particular, the effect the anchoring boundary condition has on the vortex stability. The vortex was assumed to be close enough to one wall, so that the remaining three walls did not influence the vortex. This simplified the analysis as the other boundaries could be ignored. This assumption allowed an analytical expression for the minimum distance of approach for a vortex to the cell wall before instability arose to be found. The formula for the minimum distance was found to be in reasonable agreement with full numerical results, especially since the numerical results showed that the vortex becomes highly deformed on approach to the boundary, which cannot be captured by the fixed trial function in use.

The simple use of the MoI reinforces its utility in nonlinear beam propagation problems. In the next chapter we will explore an elliptic shaped beam with angular momentum in a finite NLC cell.

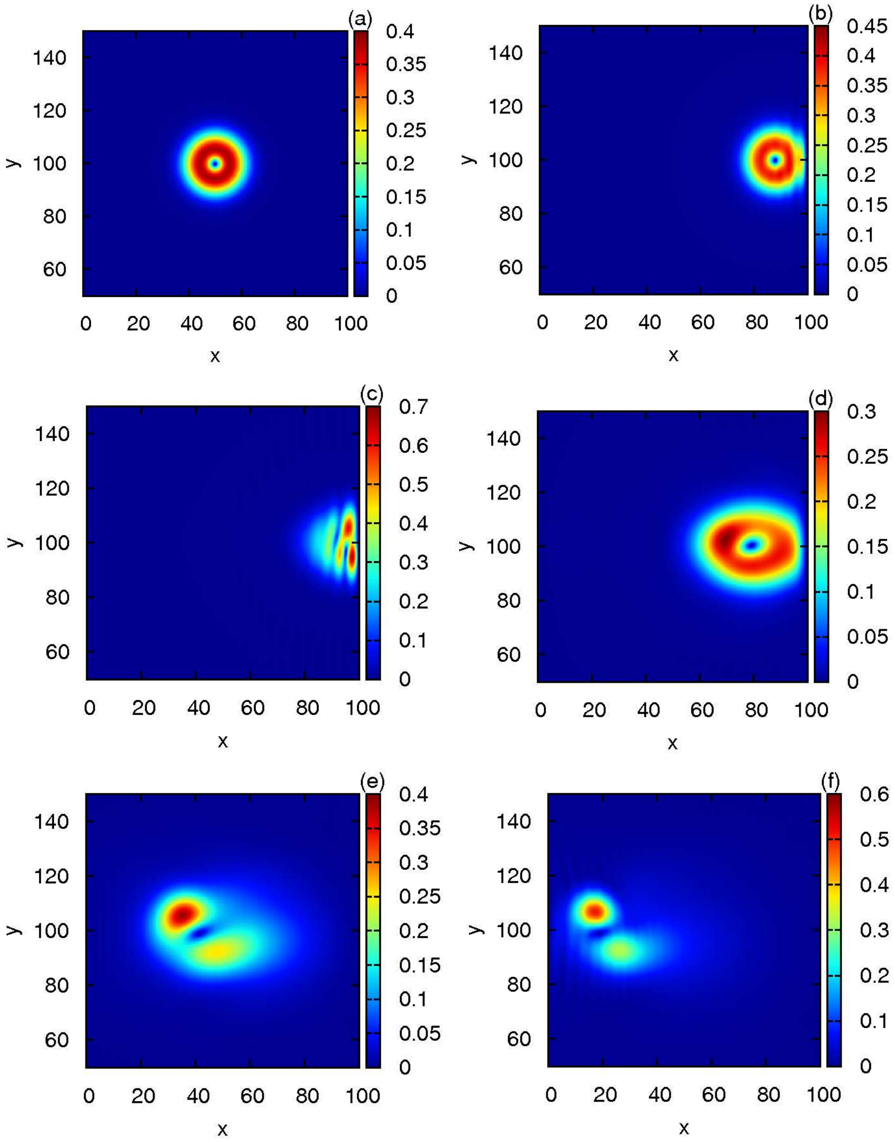

Figure 4.9: A sequence showing a vortex colliding with a cell wall, showing the instability of the vortex. (a) $z = 0$, (b) $z = 50$, (c) $z = 75$, (d) $z = 100$, (e) $z = 150$, (f) $z = 180$. The initial vortex parameters are $w = 8$,with a given by equation (4.73), $\xi = 50$, $\eta = 100$, $V_x = 0.8$ and $V_y = 0$, with $\nu = 200$, $L_x = 100$, and $L_y = 200$.

Chapter 5

Elliptic shaped nematicon in a nematic liquid crystal

5.1 Background

The stable propagation of an elliptic cross-sectional optical beam in local media has long been an experimental [109, 110] and theoretical [111, 112, 113] issue. The instability of an elliptical soliton is due to the existence of the different major and minor axes of the elliptically-shaped optical beam, or the two different widths, as the amount of nonlinearity required to support a radially symmetric soliton is dependent on the peak beam intensity [110]. Hence, the peak beam intensity also determines the diffraction angle that the medium can balance with the self-focusing of the optical beam to self-trap [25, 29] and form a soliton. For an optical beam to do this, radial symmetry is needed. However, an elliptic beam is asymmetric and, hence, difficulties arise in the support for the two competing diffraction angles [110, 113]. The term elliptic soliton will be used from here on to describe an elliptically-shaped cross-sectional soliton. To add to the difficulty of forming an elliptic soliton, it was shown both theoretically [111, 112, 113] and experimentally [109, 110, 114] that the widths of the elliptic beam periodically oscillate, as would be expected from the behaviour of beams for NLS-type equations.

Some suggested ways to form a soliton before the optical beam diffracts, resulting in a symmetric circular beam, are to use partially incoherent elliptic beams with an anisotropic mutual coherence function [109, 110], a medium with a nonlocal response [112, 115] or applying an orbital angular momentum to the elliptic-shaped optical beam [111].

Elliptic solitons were shown to exist in nonlocal NLC and found to have interesting behaviour [115]. To understand the behaviour of elliptic solitons, first, let us understand the self-focusing response of NLC. A nematic molecule tends to align itself with the polarisation direction of the optical beam. Depending on the intensity of the optical beam the molecule will rotate by a certain angle, thus altering the refractive index of the NLC and inducing a self-focusing response if and only if the optical beam conditions are right. Interestingly, a competing molecular reorientation was found to exist within the NLC. It was shown that the nematic molecules tend to align with the major axis of the elliptic beam [115].

In this chapter, an elliptically-shaped cross-sectional optical beam with orbital angular momentum propagating through a finite sized NLC cell is studied (figure 5.1(a)). The nonlocality of the NLC supports the propagation of an elliptic soliton, as the nonlocal nematic response to the elliptical optical beam smooths the response and makes the director response circular, rather than elliptic. Hence the director responds as for the propagation of a radially symmetric beam, as shown in figure 5.1(b). Therefore, the optical beam can form an elliptic soliton by balancing the diffractive spreading of the optical beam with the self-focusing induced by the nonlinear dependence of the refractive index of the NLC on the beam intensity [29, 36]. However, to induce the self-focusing response of the NLC, the optical beam intensity must be above the minimum to enable the nematic molecular rotation, known as the Freédericksz threshold [23, 24, 25, 104]. In previous chapters, the Freédericksz threshold was overcome by pre-tilting the nematic molecules by an angle $\theta_0 \sim \pi/4$, which eliminates the restriction of a minimum beam intensity to induce a change in the refractive index [33]. Experimentally, the pre-tilt is achieved by rubbing the cell walls, which creates a static charge at the boundary, which then induces in the nematic molecules closest to the boundary a molecular rotation. Finally, this rotation is transmitted on to the bulk NLC molecules due to the nonlocal elastic intermolecular forces between the molecules [25]. Rubbing the cell walls to pre-tilt the nematic

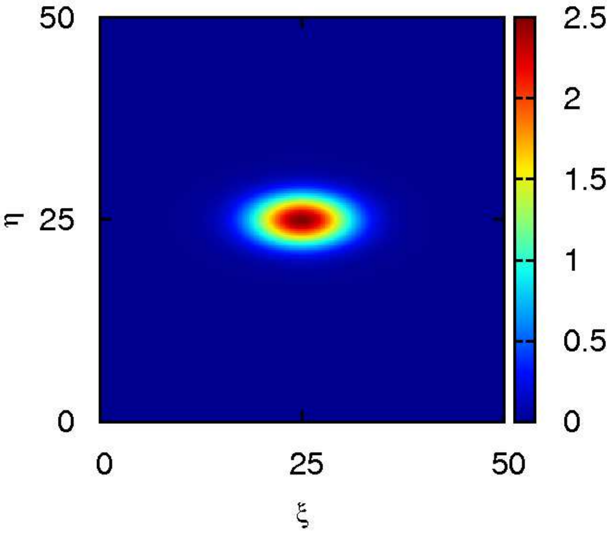

(a) Initial elliptic soliton profile

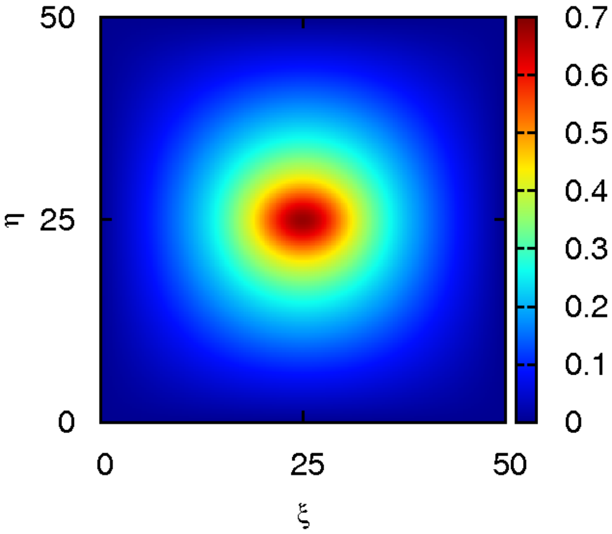

(b) Initial nematic response profile

Figure 5.1: The initial input elliptic soliton and the corresponding NLC distribution, where the initial values are $a = 2.5$, $w_x = 6$, $w_y = 3$, $\phi = 0$, $\Theta = 0.07593$, $(\xi, \eta) = (25, 25)$, and $(V_x, V_y) = (0, 0)$, with $\nu = 200$ and $(L_x, L_y) = (50, 50)$.

molecules results in different decay rates of the nematic response to the optical beam away from the centre of the optical beam. In 1D [30] a linear decay is experienced, while in 2D [45, 116] a logarithmic decay occurs. This implies that the nematic response to the beam extends to the boundaries of the NLC cell and as a result, the inclusion of proper boundary conditions is vital to model an elliptic soliton accurately.

This chapter will focus on the role radiation and orbital angular momentum loss play, as well as the effect the boundaries have, on the evolution of elliptic solitons. An averaged Lagrangian representation of the governing equations will be adopted to study the propagation of the elliptic soliton, using a combination of an exact solution and a trial function. Variational theory will also be applied [39, 59, 68] to develop the semi-analytical solution, as in Chapters 3 and 4.

Modulation theory has proved to be a successful technique in modelling the evolution of propagating nonlinear optical beams in NLC, giving excellent agreement with full numerical solutions of the governing equations [42, 53, 72, 84, 88, 102, 105] and experimental results [26, 106].

5.2 Analysis

5.2.1 Elliptically-shaped cross-sectional optical beam governing equations

Consider an elliptically-shaped cross-sectional beam input into a finite sized NLC cell with the z direction as the propagation direction. The nematic molecules are arranged in a planar configuration within the NLC cell. The optical beam is polarised in the x direction, which results in molecular rotation in the $x-z$ plane [25, 29, 34, 35, 36]. As in Chapters 3 and 4, the nematic molecules are pre-tilted by a angle $\theta_0 \sim \pi/4$ in the $x - z$ plane [33], enabling the use of milliwatt beam powers, as the Freédericksz threshold is then overcome [23, 24, 25, 104]. The pre-tilt of the nematic is achieved by rubbing the cell walls, as described in Chapters 3 and 4. The intermolecular elastic forces of the NLC pass the rotation through the bulk of the medium, thus obtaining a semi-uniform pre-tilt. The optical beam's electric field causes a further rotation of the director by an angle θ, so that the total director angle is given by $\phi = \theta_0 + \theta$, relative to the z axis. The perturbation of the director under the influence of the optical beam is small for milliwatt beam powers, $|\theta| \ll |\theta_0|$. The non-dimensional equations governing the propagation of an optical beam in this small extra rotation limit, in the paraxial approximation are a strongly coupled pair of PDEs, the first of which is a

NLS-like equation and the second is Poisson's equation [30, 43, 44, 45]

$$iE_z + \frac{1}{2}\nabla^2 E + 2\theta E = 0, \tag{5.1}$$

$$\nu\nabla^2\theta + 2|E|^2 = 0. \tag{5.2}$$

The Laplacian ∇^2 is in the $x - y$ plane. E is the complex valued envelope of the electric field. The elastic response of the NLC is related to the nonlocality parameter ν, which is experimentally of the order of $O(100)$ [26]. In experiments, the optical beam experiences a phenomenon know as walk-off, whereby the optical beam deviates from the input wavevector along the z direction, following the beam's Poynting vector instead. The walk-off has been removed from the governing equations (5.1) and (5.2) by using a phase factor [40, 42]. The NLC cell is a finite sized rectangle, with dimensions $0 \leq x \leq L_x$ and $0 \leq y \leq L_y$ and is depicted in figure 2.1.

The governing equations (5.1) and (5.2) have the Lagrangian representation

$$L = i(E^* E_z - E E_z^*) - |\nabla E|^2 + 4\theta|E|^2 - \nu|\nabla\theta|^2, \tag{5.3}$$

where the $*$ superscript denotes the complex conjugate. As in Chapters 3 and 4, a trial function, E, will be used to derive modulation equations for the elliptical beam evolution, based on this Lagrangian [60]. However, an alternative variational method, known as the chirp method [59, 68], will also be used. This adds a quadratic phase term to the trial function, E_c, for the envelope of the optical beam's electric field. Further, the governing equation (5.2) for the director perturbation is solved using a Fourier series expansion, which gives the solution in terms of an infinite series. The director equation (5.2) was not solved via the MoI as the asymmetry of the beam introduced additional complexities, rendering the MoI unusable.

This chapter will focus on the propagation of an elliptic soliton as it evolves within a finite sized NLC cell.

5.2.2 Chirp method

As mentioned in previous chapters, the governing equations (5.1) and (5.2) have no known exact solitary wave solution [72]. Techniques involving modulation theory, including the averaged Lagrangian technique [39, 59] have been developed to model the evolution of the optical beam as it propagates through a NLC cell.

A trial function is used to model the envelope of the optical beam's electric field. A Gaussian shaped profile is chosen as the trial function, as in Chapters 3 and 4

$$E = ae^{-(x-\xi)^2/w_x^2-(y-\eta)^2/w_y^2}e^{i\sigma}, \tag{5.4}$$

where a is the amplitude, w_x is the major axis and w_y is the minor axis of the ellipse, (ξ, η) is its position and σ is its phase. All the parameters are functions of z the propagation variable. The chirp form of the trial function alters the phase term of equation (5.4) by perturbing the phase by adding quadratic corrections [59, 68]. What differentiates this study from the nematicon of Chapter 3, is the addition of an orbital angular momentum term in the phase [111]. This additional phase term was shown to stop the collapse experienced by elliptic solitons in Kerr media [111, 113]. The angle the major axis of the elliptical beam makes with the x axis will be denoted by ϕ. Then coordinates (X, Y) centred on the beam and along its axes are

$$X = (x-\xi)\cos\phi + (y-\eta)\sin\phi, \quad Y = -(x-\xi)\sin\phi + (y-\eta)\cos\phi. \tag{5.5}$$

Hence, the chirp trial function representing an elliptic soliton propagating through a NLC cell with angular momentum in this rotated coordinate frame is given by

$$E_c = ae^{-(X^2/w_x^2+Y^2/w_y^2)}e^{i(\zeta+\zeta_c)}, \tag{5.6}$$

where $\zeta = \sigma + V_x(x-\xi) + V_y(y-\eta)$ and $\zeta_c = BX^2 + XY\Theta + CY^2$. Θ gives the asymmetric phase factor related to the orbital angular momentum of the beam, (V_x, V_y) is the velocity and B and C are related to the chirping of the phase.

The solution of the director equation (Poisson's equation) (5.2) for the director angle perturbation can be calculated in the form of an eigenfunction expansion, with $|E|^2$ given by (5.6). As in Chapters 3 and 4, the solution is

$$\theta = -\sum_{n,m=1}^{\infty} \frac{C_{nm}}{\pi^2 Q_1} \sin\frac{n\pi x}{L_x} \sin\frac{m\pi y}{L_y}. \tag{5.7}$$

Using the orthogonality condition for the trigonometric functions, the Fourier coefficients are

$$\begin{aligned} C_{nm} &= -\frac{8}{\nu L_x L_y}\int_0^{L_y}\int_0^{L_x}|E|^2\sin\frac{n\pi x}{L_x}\sin\frac{m\pi y}{L_y}\,dx\,dy \\ &= -\frac{2\pi a^2 w_x w_y}{\nu L_x L_y}\alpha e^{-\gamma_1}, \end{aligned} \tag{5.8}$$

where

$$\gamma_1 = \frac{n^2\pi^2}{8\rho_1 L_x^2}, \quad U_\pm = \frac{\pi^2 w_x^2 w_y^2}{8\rho_1}\psi_\pm^2, \quad \vartheta_\pm = \frac{n\pi\xi}{L_x} \pm \frac{m\pi\eta}{L_y}$$
$$Q_1 = \frac{n^2}{L_x^2} + \frac{m^2}{L_y^2}, \quad \rho_1 = \frac{\cos^2\phi}{w_x^2} + \frac{\sin^2\phi}{w_y^2}, \quad \rho_3 = \cos\phi\sin\phi\left(\frac{1}{w_x^2} - \frac{1}{w_y^2}\right)$$
$$\alpha = \left(e^{-U_+}\cos\vartheta_- - e^{-U_-}\cos\vartheta_+\right), \quad \text{and} \quad \psi_\pm = \left(\frac{\rho_3 n}{L_x} \pm \frac{\rho_1 m}{L_y}\right).$$

Substituting the trial function (5.6) for the electric field and the director solution (5.7) into the Lagrangian (5.3), gives the averaged Lagrangian

$$\begin{aligned} \mathcal{L} &= \int_0^{L_y}\int_0^{L_x} L\,dx\,dy, \\ &= -\pi a^2 w_x w_y\left(\sigma' - V_x\xi' - V_y\eta' + \frac{V_x^2}{2} + \frac{V_y^2}{2} + \frac{w_x^2 B'}{4} - \frac{w_y^2 C'}{4} - \frac{(w_x^2 - w_y^2)\Theta\phi'}{4}\right) \\ &\quad - \frac{\pi a^2(w_x^2 + w_y^2)}{2w_x w_y}\left[1 + \frac{w_x^2 w_y^2\Theta^2}{4}\right] - \frac{1}{2}\pi a^2 w_x w_y(w_x^2 B^2 + w_y^2 C^2) \\ &\quad + \sum_{n,m=1}^{\infty}\frac{\nu L_x L_y C_{nm}^2}{4\pi^2 Q_1} \end{aligned} \tag{5.9}$$

Taking variations of this averaged Lagrangian (5.9) with respect to the optical beam parameters and using the Euler–Lagrange equation (2.18), results in variational equations

$$\frac{d}{dz}\left[a^2 w_x w_y\right] = 0, \tag{5.10}$$

$$\frac{d\xi}{dz} = V_x, \qquad \frac{d\eta}{dz} = V_y, \tag{5.11}$$

$$\frac{d}{dz}\left[a^2 w_x w_y V_x\right] = -\sum_{n,m=1}^{\infty} \frac{2na^4 w_x^2 w_y^2}{\nu L_x^2 L_y Q_1}\alpha\Phi e^{-2\gamma_1}, \tag{5.12}$$

$$\frac{d}{dz}\left[a^2 w_x w_y V_y\right] = \sum_{n,m=1}^{\infty} \frac{2ma^4 w_x^2 w_y^2}{\nu L_x L_y^2 Q_1}\alpha\Phi e^{-2\gamma_1}, \tag{5.13}$$

$$\frac{d}{dz}\left[a^2 w_x^3 w_y\right] = 4a^2 w_x^3 w_y B, \tag{5.14}$$

$$\frac{d}{dz}\left[a^2 w_x w_y^3\right] = 4a^2 w_x w_y^3 C, \tag{5.15}$$

$$\frac{d\phi}{dz} = \frac{(w_x^2 + w_y^2)\Theta}{(w_x^2 - w_y^2)}, \tag{5.16}$$

$$\frac{d}{dz}\left[a^2 w_x w_y (w_x^2 - w_y^2)\Theta\right] = \sum_{n,m=1}^{\infty} \frac{2\pi a^4 w_x^2 w_y^2 \alpha e^{-2\gamma_1}}{\nu L_x L_y \rho_1 Q_1}\left[\chi - \frac{\alpha M \rho_3}{\rho_1}\right] \tag{5.17}$$

$$\begin{aligned}
\sigma' + \frac{1}{4}\left[w_x^2 B' + w_y^2 C' - (w_x^2 - w_y^2)\Theta\phi'\right] = \\
\frac{1}{2}\left(V_x^2 + V_y^2\right) - \frac{(w_x^2 + w_y^2)}{2w_x^2 w_y^2}\left(1 + \frac{w_x^2 w_y^2 \Theta^2}{4}\right) \\
-\frac{1}{2}\left(w_x^2 B^2 + w_y^2 C^2\right) + \sum_{n,m=1}^{\infty} \frac{2a^2 w_x w_y \alpha^2 e^{-2\gamma_1}}{\pi\nu L_x L_y Q_1},
\end{aligned} \tag{5.18}$$

$$\begin{aligned}
\sigma' + \frac{1}{4}\left(3w_x^2 B' + w_y^2 C' - (3w_x^2 + w_y^2)\Theta\phi'\right) = \\
\frac{1}{2}\left(V_x^2 + V_y^2\right) - \frac{1}{2}\left(3w_x^2 B^2 + w_y^2 C^2 - \frac{1}{w_x^2} + \frac{1}{w_y^2} + \frac{(3w_x^2 + w_y^2)\Theta^2}{4}\right) \\
+ \sum_{n,m=1}^{\infty} \frac{a^2 w_x w_y \alpha e^{-2\gamma_1}}{2\pi\nu L_x L_y Q_1}\left[\alpha\left(4 - \frac{\pi^2 \cos^2\phi M}{w_x^2 \rho_1^2}\right)\right. \\
\left. - \frac{\pi^2 w_y^2}{\rho_1}\left(w_x^2 G_2 - \frac{n\sin(2\phi)G}{L_x}\right)\right],
\end{aligned} \tag{5.19}$$

$$\begin{aligned}\sigma' + \frac{1}{4}\left(w_x^2 B' + 3w_y^2 C' - (w_x^2 - 3w_y^2)\Theta\phi'\right) = & \qquad (5.20)\\ \frac{1}{2}\left(V_x^2 + V_y^2\right) - \frac{1}{2}\left(w_x^2 B^2 + 3w_y^2 C^2 + \frac{1}{w_x^2} - \frac{1}{w_y^2} + \frac{(w_x^2 + 3w_y^2)\Theta^2}{4}\right) & \\ + \sum_{n,m=1}^{\infty} \frac{a^2 w_x w_y \alpha e^{-2\gamma_1}}{2\pi\nu L_x L_y Q_1}\left[\alpha\left(4 - \frac{\pi^2 \sin^2\phi M}{w_y^2 \rho_1^2}\right)\right. & \\ \left. - \frac{\pi^2 w_x^2}{\rho_1}\left(w_y^2 G_2 + \frac{n\sin(2\phi)G}{L_x}\right)\right]. &\end{aligned}$$

for the elliptical beam evolution. Here

$$\Phi = e^{-U_+}\sin\vartheta_- - e^{-U_-}\sin\vartheta_+, \tag{5.21}$$

$$M = \frac{n^2}{L_x^2} + w_x^2 w_y^2 \psi_+\psi_-, \tag{5.22}$$

$$\chi = \frac{n\cos(2\phi)(w_x^2 - w_y^2)G}{L_x}, \tag{5.23}$$

$$G = \psi_+ e^{-U_+}\cos\vartheta_- - \psi_- e^{-U_-}\cos\vartheta_+, \tag{5.24}$$

$$G_2 = \psi_+^2 e^{-U_+}\cos\vartheta_- - \psi_-^2 e^{-U_-}\cos\vartheta_+. \tag{5.25}$$

The chirp method cannot be altered in any way to account for diffractive radiation loss [60]. Therefore, the chirp solution will oscillate around the steady state solution of the initial optical beam with a constant amplitude oscillation. However, the chirp method still supplies valuable information about the dynamics of the solitary wave over short propagation distances, such as its trajectory.

5.2.3 Modulation theory

Following on from the method originally described by Kath and Smyth [60], the trial function can be modified to include the loss to radiation shed by the evolving solitary wave and, thus allow the solution to settle to its steady state as $z \to \infty$. As in Chapters 3 and 4, the trial function is given by a Gaussian profile

$$E_e = \left(ae^{-(X^2/w_x^2 + Y^2/w_y^2)} + ig \right) e^{i(\zeta + \zeta_e)}, \tag{5.26}$$

where a, w_x, w_y, X, Y and ζ have the same meaning as in section 5.2.2 for the chirp trial function. In this case, $\zeta_e = XY\Theta$, with Θ related to the orbital angular momentum of the optical beam. This method differs from the chirp method as the trial function includes the shelf height g, which is linked to the low wavenumber diffractive radiation that accumulates under the evolving solitary wave [60]. This term also allows matching to the diffractive radiation shed by the beam, which allows the modulation solution to evolve to a steady state. Perturbative analysis of linearised governing equations of NLS-type have shown the existence of the shelf and determined it to be $\pi/2$ out of the phase with the solitary wave [60, 73]. A simple physical argument for the existence of the shelf was given in Section 3.2.2. The shelf of radiation that forms under the solitary wave cannot remain flat forever. Hence, g is taken to be non-zero in the elliptically shaped region $w_y^2 X^2 + w_x^2 Y^2 \leq w_x^2 w_y^2$.

The trial function (5.26) and the Fourier series solution for the director angle (5.7), which is the same as for the chirp trial function as $|E|$ is the same, are substituted into the Lagrangian (5.3), which is then averaged over the cell lengths in the $x - y$ plane, resulting in the averaged Lagrangian

$$\begin{aligned}\mathcal{L} =& -2\pi a g' w_x w_y - 4\pi\left(\frac{a^2 w_x w_y}{4} + g^2\Lambda\right)\left(\sigma' - V_x\xi' - V_y\eta' + \frac{V_x^2}{2} + \frac{V_y^2}{2}\right)\\ &+ \frac{1}{4}\pi a^2 w_x w_y\left(w_x^2 - w_y^2\right)\Theta\phi' + 2\pi a' g w_x w_y + 2\pi a g w_x' w_y + 2\pi a g w_x w_y'\\ &- \frac{\pi a^2 w_y}{2w_x} - \frac{\pi a^2 w_x}{2w_y} - \frac{1}{8}\pi a^2 w_x w_y\left(w_x^2 + w_y^2\right)\Theta^2 + \sum_{n,m=1}^{\infty}\frac{\nu L_x L_y C_{nm}^2}{4\pi^2 Q_1}.\end{aligned} \tag{5.27}$$

Here, $\Lambda = \beta w_x w_y$, and β is to be determined. Using the Euler–Lagrange equation (2.18) to take variations of the averaged Lagrangian (5.27) with respect to the beam parameters yields a system of first-order ODEs, known as modulation equations, whose solution gives the evolution of the propagating elliptic soliton. Diffractive radiation loss can then be included in the modulation equations as in Chapters 3 and 4. The modulation equations, including the loss to shed radiation, are then

$$\frac{d}{dz}\left[\frac{a^2 w_x w_y}{4} + g^2\Lambda\right] = -2\delta\Lambda\kappa^2, \tag{5.28}$$

$$a' w_x w_y + a w_x' w_y + a w_x w_y' - 2g\Lambda\sigma' = -g\Lambda\left(V_x^2 + V_y^2\right), \tag{5.29}$$

$$\xi' = V_x, \quad \eta' = V_y, \tag{5.30}$$

$$\frac{d}{dz}\left[\left(\frac{a^2 w_x w_y}{4} + g^2\Lambda\right)V_x\right] = -\sum_{n,m=1}^{\infty}\frac{n a^4 w_x^2 w_y^2 \alpha\Phi e^{-\gamma_1}}{2\nu L_x^2 L_y Q_1}, \tag{5.31}$$

$$\frac{d}{dz}\left[\left(\frac{a^2 w_x w_y}{4} + g^2\Lambda\right)V_y\right] = \sum_{n,m=1}^{\infty}\frac{m a^4 w_x^2 w_y^2 \alpha\Phi e^{-\gamma_1}}{2\nu L_x L_y^2 Q_1}, \tag{5.32}$$

$$\phi' = \frac{\left(w_x^2 + w_y^2\right)}{\left(w_x^2 - w_y^2\right)}\Theta, \tag{5.33}$$

$$\begin{aligned}\frac{d}{dz}\left[\left(a^2 w_x w_y \left(w_x^2 - w_y^2\right)\right)\Theta\right] = &\sum_{n,m=1}^{\infty} \frac{2\pi a^4 w_x^2 w_y^2 \alpha e^{-\gamma_1}}{\nu L_x L_y Q_1 \rho_1} \\ &\times \left[\frac{n\cos\left(2\phi\right)\left(w_x^2 - w_y^2\right)G}{L_x} - \frac{\alpha M \rho_3}{\rho_1}\right],\end{aligned} \tag{5.34}$$

$$\begin{aligned}\frac{dg}{dz} =& \frac{a\left(w_x^2 + w_y^2\right)\Theta^2}{16} + \frac{a}{4w_x^2} + \frac{a}{4w_y^2} - \sum_{n,m=1}^{\infty} \frac{a^3 w_x w_y \alpha e^{-\gamma_1}}{8\pi\nu L_x L_y Q_1 \rho_1} \\ &\times \left[\pi^2 \alpha M + 2\pi^2 w_x^2 w_y^2 G_2 + \frac{\pi^2 n \sin\left(2\phi\right)\left(w_x^2 - w_y^2\right)G}{L_x}\right] - 2\delta g,\end{aligned} \tag{5.35}$$

$$\begin{aligned}\frac{d\sigma}{dz} =& \frac{1}{2}\left(V_x^2 + V_y^2\right) - \frac{1}{w_x^2} - \frac{1}{w_y^2} + \sum_{n,m=1}^{\infty} \frac{a^2 w_x w_y \alpha e^{-\gamma}}{4\pi\nu L_x L_y Q_1} \\ &\times \left[\alpha\left(8 + \frac{\pi^2 M}{\rho_1}\right) + \frac{2\pi^2 w_x^2 w_y^2 G_2}{\rho_1} + \frac{\pi^2 n \sin\left(2\phi\right)\left(w_x^2 - w_y^2\right)G}{L_x}\right].\end{aligned} \tag{5.36}$$

The algebraic equation for Θ is given by

$$\Theta^2 = \frac{\left(w_x^2 - w_y^2\right)}{D}\left[-\frac{4}{w_x^2} + \frac{4}{w_y^2} - \sum_{n,m=1}^{\infty} \frac{2\pi a^2 w_x w_y \alpha e^{-\gamma_1}\left(W - F\right)}{\nu L_x L_y Q_1 \rho_1}\right], \tag{5.37}$$

where

$$D = w_x^4 + 6w_x^2 w_y^2 + w_y^4, \tag{5.38}$$

$$F = \frac{\alpha M}{\rho_1}\left(\frac{\cos^2\phi}{w_x^2} - \frac{\sin^2\phi}{w_y^2}\right), \tag{5.39}$$

$$W = \frac{n\sin\left(2\phi\right)\left(w_x^2 + w_y^2\right)G}{L_x}. \tag{5.40}$$

As in Chapters 3 and 4, the loss coefficient δ is

$$\delta = -\frac{\sqrt{2\pi}}{32e\kappa\tilde{\Lambda}}\int_0^z \pi\kappa(z')\ln[(z-z')/\tilde{\Lambda}]\times \tag{5.41}$$
$$\left[\left(\left\{\frac{1}{2}\ln[(z-z')/\tilde{\Lambda}]\right\}^2+\frac{3\pi^2}{4}\right)^2+\pi^2\left\{\ln[(z-z')/\tilde{\Lambda}]\right\}^2\right]^{-1}\frac{dz'}{(z-z')},$$

where

$$\kappa^2 = \frac{1}{\tilde{\Lambda}}\left[\frac{1}{4}a^2w_xw_y - \frac{1}{4}\hat{a}^2\hat{w}^2 + \tilde{\Lambda}g^2\right]. \tag{5.42}$$

The nonlocality of the NLC shifts the point at which the solitary wave sheds diffractive radiation from the edge of the shelf $\sqrt{w_y^2X^2+w_x^2Y^2} = w_xw_y$ to a new radius $\tilde{\ell}$ from the solitary wave position (ξ,η), which is the edge of the director response [72]. This radius for the radiation response was termed the outer shelf radius [72]. In the present case of a finite cell, the director response extends to the cell walls. Hence,

$$\tilde{\Lambda} = \tilde{\ell}^2/2 \tag{5.43}$$

where

$$\tilde{\ell} = \min\left(\frac{L_x}{2},\frac{L_y}{2}\right), \tag{5.44}$$

as in Chapters 3 and 4. In the case of a finite cell, the diffractive radiation is then shed in a boundary layer at the cell walls, as for the nematicon and vortex of Chapters 3 and 4

The final parameter to be determined is the area of the radiation shelf, $\Lambda = \beta w_xw_y$. As in Chapters 3 and 4 $\beta = 0.3$ was found to be a robust choice to give good comparison with full numerical solutions for different input beams.

The steady state for the elliptic soliton can be found using total energy conservation for the system. As in Chapters 3 and 4, Nöther's theorem is used to find the energy conservation equation based on the invariance of the Lagrangian (5.3) with respect to shifts in z (as shown in Section 3.2.2). The averaged energy conservation is then

$$\begin{aligned}\frac{dH}{dz} &= \frac{d}{dz}\int_0^{L_y}\int_0^{L_x}\left[|\nabla E|^2 - 4\theta|E|^2 + \nu|\nabla\theta|^2\right]dx\,dy \\ &= \frac{d}{dz}\left\{\frac{\pi a^2 w_y}{2w_x} + \frac{\pi a^2 w_x}{2w_y} - \sum_{n,m=1}^{\infty}\frac{\nu L_x L_y C_{nm}^2}{4\pi^2 Q_1}\right\} = 0. \qquad (5.45)\end{aligned}$$

The details for deriving this are as in Chapter 2, and so are not given here. The cell boundaries are again found to be repulsive towards the solitary wave, in accord with the results found in Chapters 3 and 4 [30, 45, 116]. The elliptic soliton as a result of this repulsion takes a helical trajectory towards the centre of the NLC cell, the final steady state position. At the centre all four boundaries exert an equal amount of force on the solitary wave, pinning it in place. Again, the carat ˆ will denote the steady state values of quantities. We then have $\hat{\xi} = L_x/2$, $\hat{\eta} = L_y/2$, $\hat{V}_x = 0$, $\hat{V}_y = 0$. At the steady state the elliptic soliton will reshape into a circular cross-section due to symmetry. Hence, it will no longer be rotating with an orbital angular momentum and will have no discernible orientation angle due to the radial symmetry of the optical beam, that is $\hat{\Theta} = 0$ and $\hat{\phi} = 0$. Also, the elliptic soliton will have stopped shedding radiation at the steady state, and hence the shelf height $\hat{g}$ will be zero. Thus, the modulation equation (5.35) can be used to find the steady state relationship between the amplitude $\hat{a}$ and width $\hat{w}$ (here $\hat{w} = \hat{w_x} = \hat{w_y}$ for the symmetry reasons stated above) of the elliptic soliton, which yields

$$\hat{a}^2 = \frac{4\nu L_x L_y}{\pi \hat{w}^6 \Omega}, \tag{5.46}$$

where

$$\Omega = \sum_{n,m=1}^{\infty} e^{-\hat{\gamma_1}} \sin\left(\frac{n\pi\xi}{L_x}\right) \sin\left(\frac{m\pi\eta}{L_y}\right), \tag{5.47}$$

$$\hat{\gamma_1} = \frac{\pi^2 \hat{w}^2 Q_1}{4}. \tag{5.48}$$

The combination of the energy conservation equation (5.45) and the steady state relation (5.46) is used to find the final steady state values for the amplitude and width of the elliptic soliton for given initial beam parameters.

5.2.4 Inclusion of angular momentum loss

As the elliptic soliton evolves the beam reshapes into a circle over large z distances. This reshaping is a consequence of the symmetry of the medium [110, 113]. In addition, the reshaping is driven by loss of angular momentum to shed diffractive radiation. By overall conservation of angular momentum as the elliptic soliton loses angular momentum, the speed at which it spins also slows. The net result is that the elliptic nematicon becomes circular, so that $w_y \to w_x$.

It is then vital to determine the angular momentum shed as diffractive radiation as the elliptic nematicon evolves. Due to the spinning of the beam, these shed waves have a spiral pattern. As the spiral waves [117] have small amplitude relative to the beam they satisfy the linearised NLS equation

$$iE_z + \frac{1}{2}\nabla^2 E = 0. \tag{5.49}$$

The boundary condition for these spiral waves at the elliptic soliton is a signaling boundary condition as the elliptic beam sheds the waves. To determine this boundary condition, recall that the trial function of the elliptic soliton is (5.26), which is in the rotating frame of reference with coordinates and angular velocity given by (5.33). We are only interested in the radiation that is shed from the accumulated shelf under the elliptic solitary wave. As the radiation matches to the edge of the shelf, for the matching the trial function (5.26) is given by the shelf only, yielding

$$E \sim g e^{i(\sigma + \Theta XY)} \tag{5.50}$$

For ease in notation and calculation, the rotating coordinates X and Y can be written in terms of matrices

$$\begin{pmatrix} X \\ Y \end{pmatrix} = A(\phi) \begin{pmatrix} x \\ y \end{pmatrix}, \tag{5.51}$$

where the rotation matrix is

$$A(\phi) = \begin{pmatrix} \cos\phi & \sin\phi \\ -\sin\phi & \cos\phi \end{pmatrix}. \tag{5.52}$$

The level lines of the trial function (5.26) are ellipses parameterised in the form

$$X(\mu) = pw_x \cos\mu \quad \text{and} \quad Y(\mu) = pw_y \sin\mu, \quad 0 \le \mu \le 2\pi, \tag{5.53}$$

where p is to be chosen later.

Thus, (5.51) can be rearranged to give

$$\underline{X} = \begin{pmatrix} x \\ y \end{pmatrix} = A^{-1}(\phi) \begin{pmatrix} pw_x \cos\mu \\ pw_y \sin\mu \end{pmatrix}, \tag{5.54}$$

where

$$A^{-1}(\phi) = \begin{pmatrix} \cos\phi & -\sin\phi \\ \sin\phi & \cos\phi \end{pmatrix}. \tag{5.55}$$

Now, the spiral radiation boundary condition has the form

$$E = g\exp[i(\Theta(z)p^2 w_x w_y \cos\mu \sin\mu + \sigma(z))] \tag{5.56}$$

as it is found by the signalling boundary condition on the curve p as given by equation (5.50).

The radiation equation (5.49) will be solved using a geometric optics solution [39]

$$E = ue^{iS(x,y,z)}. \tag{5.57}$$

Substitution of this from the radiation equation (5.49) yields the eikonal equation

$$S_z + \frac{1}{2}|\nabla S|^2 = 0. \tag{5.58}$$

Comparing the geometric optics solution (5.57) with the boundary condition (5.56) we see that

$$S(x,y,z) = \Theta(z)p^2 w_x w_y \cos\mu \sin\mu + \sigma(z) \quad \text{and} \quad u = g. \tag{5.59}$$

To find the angular momentum radiated by the elliptic soliton, we need to determine the derivative S normal to the boundary curve at the beam. To obtain the desired derivative, the eikonal equation (5.58) is rewritten using the tangential coordinate μ and the normal coordinate λ of the elliptical boundary (5.54) in the form

$$\underline{X} = \begin{pmatrix} x \\ y \end{pmatrix} + \lambda \underline{n}(z,\mu), \tag{5.60}$$

where

$$\underline{n} = \frac{\underline{X}_\mu^\perp}{|\underline{X}_\mu|} = \frac{1}{|\underline{X}_\mu|}\begin{pmatrix} -y_\mu \\ x_\mu \end{pmatrix}. \tag{5.61}$$

Here, X_μ and Y_μ are the derivatives of equation (5.54) with respect to μ and are given by

$$\begin{pmatrix} -Y_\mu \\ X_\mu \end{pmatrix} = A^{-1}(\phi)\begin{pmatrix} -pw_x \cos\mu \\ pw_y \sin\mu \end{pmatrix}. \tag{5.62}$$

The norm of $\underline{X}_\mu^\perp$ is equal to the norm of $\underline{X}_\mu$ and is $|\underline{X}_\mu| = p\sqrt{w_x^2 \sin^2\mu + w_y^2 \cos^2\mu}$.

In these coordinates, the eikonal equation (5.58) becomes

$$S_z + \frac{1}{2}\left\{\left(\frac{S_\mu}{|\underline{X}_\mu|}\right)^2 + S_\lambda^2\right\} = 0, \tag{5.63}$$

where S_μ and S_λ are the derivatives of S with respect to μ and λ respectively. Now, let us take the derivative of S in equation (5.59) with respect to the time-like parameter z, to yield

$$S_z + \nabla S \cdot \underline{X}_z = \frac{1}{2}\Theta_z p^2 w_x w_y \sin{(2\mu)} + \sigma_z. \tag{5.64}$$

In the calculation the derivatives on the slowly varying axis w_x and w_y have been neglected. $\nabla S \cdot \underline{X}_z$, is not calculated in terms of the tangential and normal coordinates to obtain the outgoing wavenumber S_λ from equation (5.63). We have that

$$\nabla S \cdot \underline{X}_z = \frac{S_\mu}{\left|\underline{X}_\mu\right|^2}\left(\underline{X}_\mu \cdot \underline{X}_z\right) + \frac{S_\lambda}{\left|\underline{X}_\mu\right|}\left(\underline{X}_\mu^\perp \cdot \underline{X}_z\right) \tag{5.65}$$

$$= \phi_z p^2 \left[\frac{w_x w_y S_\mu}{\left|\underline{X}_\mu\right|^2} + \frac{(w_x^2 + w_y^2)\sin{(2\mu)}\, S_\lambda}{2\left|\underline{X}_\mu\right|}\right]. \tag{5.66}$$

The eikonal equation (5.64) can now be rearranged to give,

$$S_z = \frac{1}{2}\Theta_z p^2 w_x w_y \sin{(2\mu)} + \sigma_z - \phi_z p^2 \left[\frac{w_x w_y S_\mu}{\left|\underline{X}_\mu\right|^2} + \frac{(w_x^2 + w_y^2)\sin{(2\mu)}\, S_\lambda}{2\left|\underline{X}_\mu\right|}\right]. \tag{5.67}$$

Substitution of this expression into the eikonal equation (5.63) to give

$$\frac{1}{2}\Theta_z p^2 w_x w_y \sin{(2\mu)} + \sigma_z - \phi_z p^2 \left[\frac{w_x w_y S_\mu}{\left|\underline{X}_\mu\right|^2} + \frac{(w_x^2 + w_y^2)\sin{(2\mu)}\, S_\lambda}{2\left|\underline{X}_\mu\right|}\right]$$
$$+ \frac{1}{2}\left\{\left(\frac{S_\mu}{\left|\underline{X}_\mu\right|}\right)^2 + S_\lambda^2\right\} = 0. \tag{5.68}$$

Now ϕ_z can be replaced using the modulation equation (5.33) and S_μ is given by the derivative of equation (5.59) with respect to μ, to yield

$$S_\mu = \Theta p^2 w_x w_y \cos{(2\mu)}\,, \tag{5.69}$$

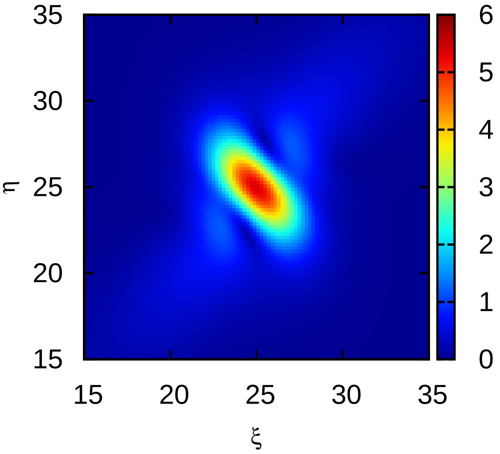

Figure 5.2: Profile of an elliptic nematicon with diffractive radiation shed along the major axis rotating counter-clockwise.

as σ is a function of z only.

Further, numerical simulations indicate that the radiation shed by the elliptic nematicon occurs along the major axis, as shown in figure 5.2. Thus, the angle at which radiation is shed is small, leading to the approximations $\cos(2\mu) \approx 1$ and $\sin(2\mu) \approx 0$. Now, equation (5.68) can be re-expressed as a quadratic equation for the derivative normal to the boundary curve, S_λ,

$$-\frac{\Theta^2 p^4 w_x^2 w_y^2 (w_x^2 + w_y^2)}{(w_x^2 - w_y^2)\left|\underline{X}_\mu\right|^2} + \frac{\Theta^2 p^4 w_x^2 w_y^2}{2\left|\underline{X}_\mu\right|^2} + \frac{S_\lambda^2}{2} = 0. \tag{5.70}$$

Solving equation (5.70) results in the derivative of the normal to the boundary curve as

$$S_\lambda = \frac{\Theta p w_x \sqrt{w_x^2 + 3w_y^2}}{(w_x^2 - w_y^2)^{1/2}}. \tag{5.71}$$

Let us now use this eikonal equation solution to calculate the flux of angular momentum in the shed radiation. The angular momentum flux is given by

$$\frac{\partial \Gamma}{\partial z} = 2\mathbf{Re}\,\frac{\partial}{\partial z}\int_0^{2\pi} \left(\nabla E \cdot \underline{n}\right)\left(\nabla E^* \times \underline{X}\right)\left|\underline{X}_\mu\right|\, d\mu. \tag{5.72}$$

Using the geometric optics solution for E given by equation (5.57), the angular momentum flux can be rewritten in terms of the tangential and normal coordinates as

$$\begin{aligned}\frac{\partial \Gamma}{\partial z} &= 2\mathbf{Re}\,\frac{\partial}{\partial z}\int_0^{2\pi} (iue^{iS}S_\lambda)\left[-iue^{-iS}\left(\frac{S_\mu}{\left|\underline{X}_\mu\right|^2}\left(\underline{X}_\mu \times \underline{X}\right) + \frac{S_\lambda}{\left|\underline{X}_\mu\right|}\left(\underline{X}_\mu^\perp \times \underline{X}\right)\right)\right] d\mu \\ &= 2\mathbf{Re}\,\frac{\partial}{\partial z}\int_0^{2\pi} \left[u^2 S_\lambda\left(\frac{S_\mu}{\left|\underline{X}_\mu\right|^2}\left(\underline{X}_\mu \times \underline{X}\right) + \frac{S_\lambda}{\left|\underline{X}_\mu\right|}\left(\underline{X}_\mu^\perp \times \underline{X}\right)\right)\right] d\mu.\end{aligned} \tag{5.73}$$

Here

$$\underline{X}_\mu \times \underline{X} = -p^2 w_x w_y \begin{pmatrix} \sin\mu \\ \cos\mu \end{pmatrix} \sim -p^2 w_x w_y, \tag{5.74}$$

$$\underline{X}_\mu^\perp \times \underline{X} = -\frac{1}{2}p^2 \begin{pmatrix} w_x^2 \sin(2\mu) \\ w_y^2 \sin(2\mu) \end{pmatrix} \sim 0, \tag{5.75}$$

using the small angle approximation for μ. The norm under the small angle approximation for μ is given by, $\left|\underline{X}_\mu\right|^2 = p^2(w_x^2 \sin^2\mu + w_y^2\cos^2\mu) \sim p^2 w_y^2$. The final contribution from the angular momentum flux, using the same small angle approximation for μ as before, results in

$$\begin{aligned}\frac{\partial \Gamma}{\partial z} &= -\,2\mathbf{Re}\,\frac{\partial}{\partial z}\int_0^{2\pi} \frac{u^2 p^2 w_x w_y S_\lambda S_\mu}{\left|\underline{X}_\mu\right|}\, d\mu \\ &= -\,2\mathbf{Re}\,\frac{\partial}{\partial z}\int_0^{2\pi} \frac{u^2\Theta^2 p^4 w_x^3 w_y\sqrt{w_x^2 + 3w_y}}{(w_x^2 - w_y^2)^{1/2}}\, d\mu.\end{aligned} \tag{5.76}$$

Here $u \sim \varphi\sqrt{\hat{\Lambda}}\kappa$, κ is given by (5.42) and $\varphi = 0.3$ was found to be a robust choice to give good comparison with full numerical solutions and the paramaterisation variable p is set to equal one.

The calculated angular momentum flux loss must be added to the modulation equation related to the angular momentum of the elliptic nematicon, equation (5.34). Doing this yields

$$\begin{aligned}\frac{d}{dz}\left[a^2 w_x w_y \left(w_x^2 - w_y^2\right) \Theta\right] = \\ \sum_{n,m=1}^{\infty} \frac{2\pi a^4 w_x^2 w_y^2 \alpha e^{-\gamma_1}}{\nu L_x L_y Q_1 \rho_1} \left[\frac{n\cos\left(2\phi\right)\left(w_x^2 - w_y^2\right) G}{L_x} - \frac{\alpha M \rho_3}{\rho_1}\right] \\ - \frac{u^2 \Theta^2 p^4 w_x^3 w_y \sqrt{w_x^2 + 3w_y}}{(w_x^2 - w_y^2)^{1/2}}. \qquad (5.77)\end{aligned}$$

The modulation equations (5.28) to (5.33), (5.35), (5.36), plus equation (5.77), as well as the algebraic equation (5.37) form a system of first-order ODEs for the evolution of the elliptic nematicon that include both mass and angular momentum losses to dispersive radiation. It will be shown that the inclusion of angular momentum loss is vital to obtain good comparisons of solutions of the modulation equations with full numerical solutions.

5.3 Results

In this section, we will compare full numerical solutions of the equations (5.1) and (5.2) that govern the propagation of an elliptic soliton through a finite sized NLC cell with solutions derived using variational approximations [39, 60, 68], that is, derived using the chirp method, modulation theory including radiation loss, and finally modulation theory including both radiation and angular momentum loss, the details of which can be found in sections 5.2.2, 5.2.3 and 5.2.4, respectively.

The variational equations were solved using the standard RK4, as outlined in Section 2.3.5. The full numerical solution of the governing equations (5.1) and (5.2) was obtained using the scheme described in Section 2.4. The initial condition for the envelope of the electric field in the numerical simulations was the trial function for the chirp method, equation (5.6), which is the same as the trial function for the modulation theory, equation (5.26), at $z = 0$ as initially $B = C = 0$ and $g = 0$. Hence the initial condition for the optical beam is

$$E = ae^{-(X^2/w_x^2+Y^2/w_y^2)}e^{i(\zeta+\Theta XY)}. \tag{5.78}$$

To maintain the accuracy and stability of the full numerical scheme, the step sizes used were $\Delta x = \Delta y = 0.2$ and $\Delta z = 0.001$. The propagation length was taken to be $z = 500$, a typical non-dimensional cell length [26]. The numerical investigation was conducted using several different cell sizes with various non-dimensional widths, $50 \leq L_x \leq 100$ and $50 \leq L_y \leq 100$.

Let us first consider a propagating elliptic soliton initially positioned in the centre of a square NLC cell, with a non-dimensional width and breadth of $(L_x, L_y) = (50, 50)$, as shown by the contour plot in figure 5.1(a). We are interested in comparisons of the chirp and modulation theory solutions with each other, as well as with full numerical solutions. An amplitude com-

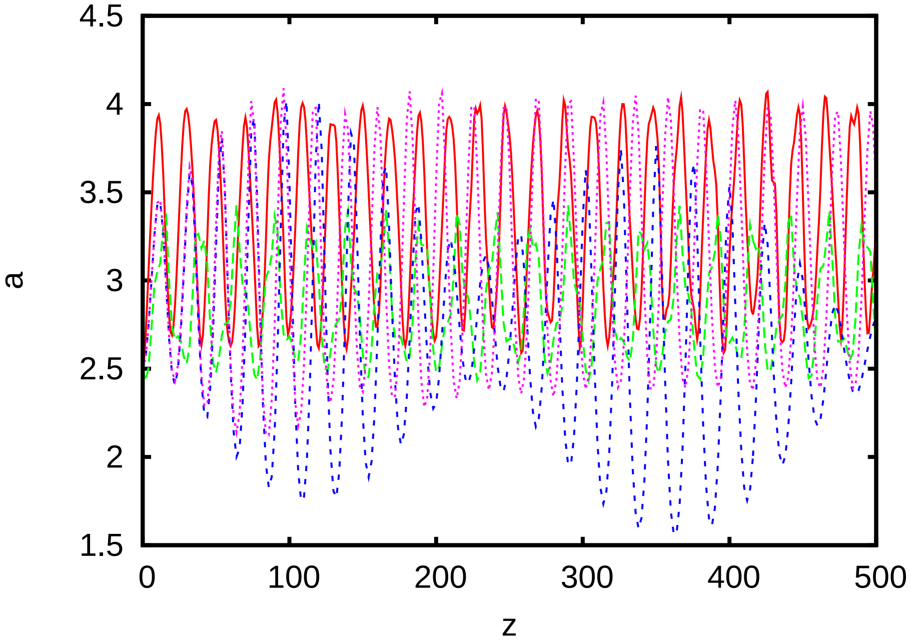

Figure 5.3: Comparison between the full numerical solution (red solid line), chirp method solution (green dashed line), modulation theory solution including radiation mass loss (blue dot-dashed line), and modulation theory solution including radiation mass loss and angular momentum loss (magenta dotted line) for the amplitude. The initial values are $a = 2.5$, $w_x = 6$, $w_y = 3$, $\phi = 0$, $\Theta = 0.07593$, $(\xi, \eta) = (25, 25)$, and $(V_x, V_y) = (0, 0)$, with $\nu = 200$ and $(L_x, L_y) = (50, 50)$.

parison is shown in figure 5.3 for a typical input beam. Due to the optical beam's initial position in the centre of the cell, the position of the elliptic soliton does not change during propagation Hence, there is no non-trivial positional information to compare. From figure 5.3, we can see that both the chirp solution and the modulation theory solution including radiation mass loss give amplitudes that oscillate around a different steady state to that of the full numerical solution. However, the modulation theory solution including radiation mass loss, matches the period of the full numerical solutions oscillations, and shows signs of damping. Including both radiation mass loss and angular momentum loss to the modulation equations causes the modulation solution to oscillate about the same steady state (mean) as the full numerical solution. This indicates that the inclusion of angular momentum loss in the modulation equations is vitally important to gain good agreement with the full numerical solution. Further, the modulation theory solution including radiation mass loss, displays signs of beating or competing modes, which is no longer present when angular momentum loss is added to the equations. Lastly, it can be seen that the chirp method does not provide an adequate approximation as loss, both mass and angular momentum, cannot be incorporated using this method. Angular momentum loss is the essential feature driving the evolution of the elliptical nematicon.

Figure 5.4(a) shows an amplitude comparison for a different input beam

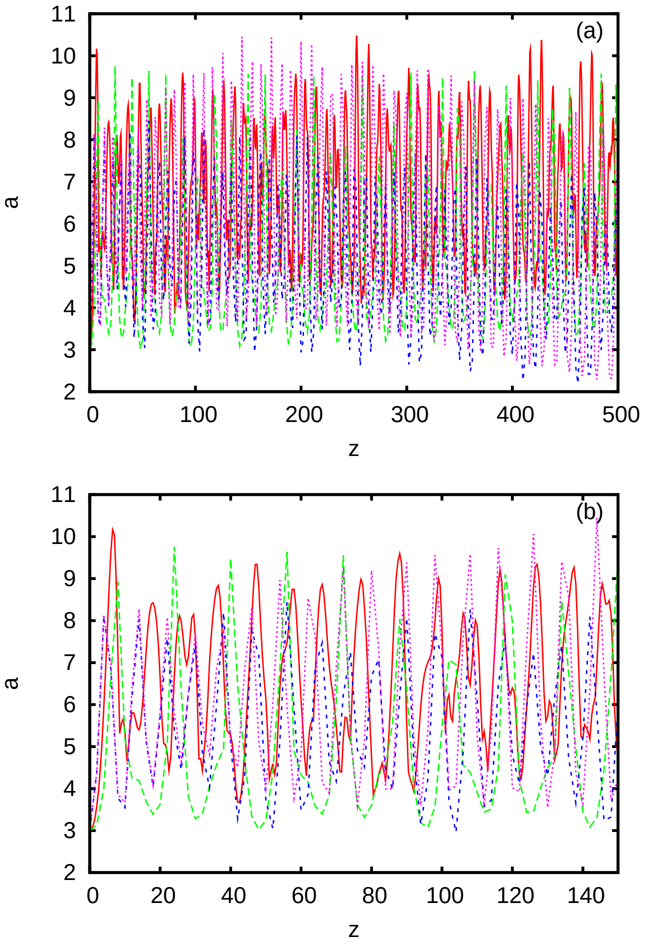

Figure 5.4: Comparison between the full numerical solution (red solid line), chirp method solution (green dashed line), modulation theory solution including radiation mass loss (blue dot-dashed line), and modulation theory solution including radiation mass loss and angular momentum loss (magenta dotted line) for (a) the amplitude and (b) the amplitude for a reduced space segment. The initial values are $a = 3$, $w_x = 7$, $w_y = 4$, $\phi = 0$, $\Theta = 0.06194$, $(\xi, \eta) = (25, 25)$, and $(V_x, V_y) = (0, 0)$, with $\nu = 200$ and $(L_x, L_y) = (50, 50)$.

positioned in the centre of the NLC cell. The amplitude oscillation of figure 5.4(a) has a short period and it is difficult to see details of the comparison for the different variational approximations. However, we can see from the peaks and troughs of the solutions that the chirp method does not match the period of the full numerical solution, but both modulation solutions do. This is due to the addition of the shelf height g in the trial function (5.26), which introduces the shelf area Λ into the averaged Lagrangian, enabling the period of the amplitude oscillation to be matched with the full numerical solution. In figure 5.4(b) only a portion of the full propagation evolution is shown, $0 \leq z \leq 150$, enabling a proper examination of how the variational solutions compare with the full numerical solution. The chirp solution's oscillation does not compare favourably with the full numerical solution, although the amplitude evolution is within the correct envelope. Radiation mass loss added to the modulation theory equations causes the amplitude oscillation to pick up extra frequencies so that the amplitude decreases and then increases. However, the period is initially well matched. The modulation theory solution including both radiation mass loss and angular momentum loss maintains nearly a steady amplitude throughout the propagation, with a period in good agreement with the numerical one. There is a good overall comparison with the full numerical solution. It should be noted that the numerical solution shows evidence of a second period due, most likely, to the independent oscillations of the two axes of the ellipse

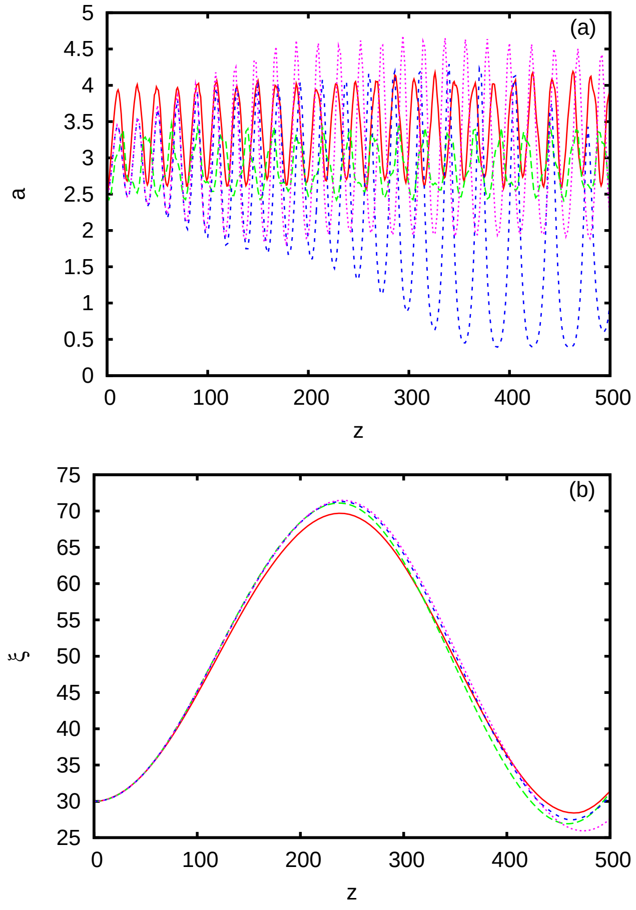

Figure 5.5: Comparison between the full numerical solution (red solid line), chirp method solution (green dashed line), modulation theory solution including radiation mass loss (blue dot-dashed line), and modulation theory solution including radiation mass loss and angular momentum loss (magenta dotted line) for (a) amplitude a and (b) x position. The initial values are $a = 2.5$, $w_x = 6$, $w_y = 3$, $\phi = 0$, $\Theta = 0.06194$, $(\xi, \eta) = (30, 25)$, and $(V_x, V_y) = (0, 0)$, with $\nu = 200$ and $(L_x, L_y) = (100, 100)$.

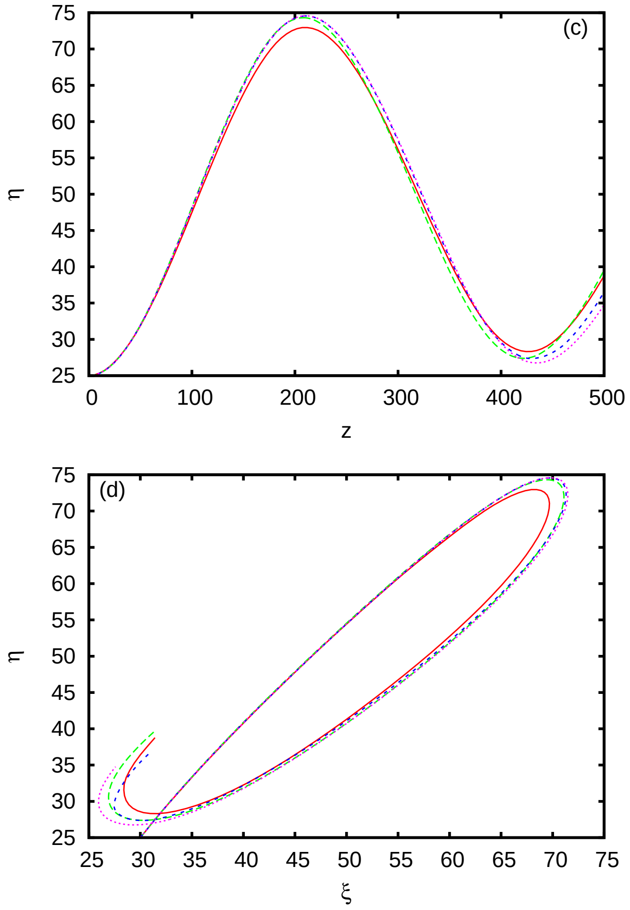

Figure 5.5: Comparison between the full numerical solution (red solid line), chirp method solution (green dashed line), modulation theory solution including radiation mass loss (blue dot-dashed line), and modulation theory solution including radiation mass loss and angular momentum loss (magenta dotted line) for (c) y position, and (d) (x, y) position for a square cell. The initial values are $a = 2.5$, $w_x = 6$, $w_y = 3$, $\phi = 0$, $\Theta = 0.06194$, $(\xi, \eta) = (30, 25)$, and $(V_x, V_y) = (0, 0)$, with $\nu = 200$ and $(L_x, L_y) = (100, 100)$.

Figure 5.5 depicts a comparison between the full numerical solution (red solid line) and the chirp (green dashed line), modulation theory solution including radiation mass loss (blue dot-dashed line), and modulation theory solution including radiation mass loss and angular momentum loss (magenta dotted line) for an off-centre input beam in a large, square NLC cell. The trajectory of the elliptic soliton is in accord with the repulsive nature of the cell walls found in Chapters 3 and 4 [43, 44, 45, 116]. The amplitude comparison is similar to that shown in figures 5.3 and 5.4, with the modulation theory solution including both radiation mass and angular momentum loss comparing well with the full numerical solution. This shows that angular momentum loss is vital to obtain good agreement with numerical solutions and is driving the evolution. Figure 5.5(a) shows that the numerical solution has a slightly greater rate of mass loss than that calculated in Chapter 2. Figures 5.5(b) and (c) show excellent trajectory comparisons for the elliptic soliton's path, with little difference between all the various variational solutions. As noted in Chapter 4, the amplitude and width decouple from the position and velocity oscillations of nonlinear beams in NLC [42, 85, 86, 105], explaining why the different variational (chirp and extended) methods can have different amplitude evolutions and yet agree in position. Figure 5.5(d) shows the helical trajectory of the beam in the z direction, which is into the page, in agreement with the trajectories found for nematicons and optical vortices in Chapters 3 and 4, respectively [45, 116].

5.4 Discussion

Elliptic solitons in finite sized nonlocal NLC cells have been studied. This work confirms the vital introduction of angular momentum loss on the elliptical beam evolution, a factor which was not considered in previous work [111].

A method based on averaging a Lagrangian representation of the governing equations (5.1) and (5.2) laid the foundations for the semi-analytical approach used to study the elliptic nematicon's evolution. To achieve this averaging, a combination of an exact solution and a trial function was used. The exact solution of Poisson's equation (5.2) describes the director perturbation and was found in the form of a Fourier series. This solution, equation (5.7), proved to be suitable for both the chirp and modulation theory methods as the optical beam's electric field envelope is the same for both approximations.

The introduction of orbital angular momentum by way of an asymmetric phase term related to the rotation of the elliptic soliton introduced additional, previously unsolved effects. The main new effect is the angular momentum evolution of the beam as it slows down to a stationary circular beam.

The chirp method is the traditional variational method used to analyse optical phenomena [68, 111]. Quadratic corrections are added to the phase for the electric field envelope, thus "chirping" the solution. However, there is no known way to extend the chirp method to include the effect of shed diffractive radiation. An alternative variational method, termed modulation theory, can be extended to include the effects of this radiation [60].

Further, in this chapter it was found that accounting for angular momentum loss in the modulation equations derived using the trial function (5.26) increased the accuracy of the solution when compared with the full numerical solution. The angular momentum loss was derived in section 5.2.4 examining the spiral waves emitted by the spinning elliptic soliton. Including both radiation mass and angular momentum loss in the modulation equations using the modulation theory trial function, dramatically improved the amplitude comparison with the full numerical solution. This demonstrates the critical role of angular momentum loss in elliptical beam evolution, the effect of which cannot be incorporated in the chirp method, leading to its poor agreement with numerical solutions.

Chapter 6

Conclusions

6.1 Summary of research

The study of the propagation of optical beams in nonlocal, nonlinear soft matter, specifically nematic liquid crystals, formed the basis of the primary research presented in this thesis. NLCs exhibit a highly nonlocal response, whereby the medium response extends far beyond the beam, due to elastic forces. The optically induced rotation of the NLC molecules alters the refractive index of the medium. This nonlocal, nonlinear response is highly tunable. Under the correct beam conditions (above the Freédericksz threshold) a nematicon can be created due to the NLC's ability to balance linear diffraction and nonlinear self-focusing, to form a self-trapped beam. Due to the robust nature of solitary waves, and the waveguide induced by them, nematicons can support the transmission of probe beams. This has lead to their proposed use in data transmission. Further, a nematicon can be steered within the NLC by exploiting both the properties of the nematic and the optical beam, leading to the possibility of switching and logic gates in all-optical devices [29].

The numerous experimental advancements within the field of nematicons has pushed the mathematical modelling forward to maintain pace, and to enable mathematicians to provide valuable assistance with future explorations in this field. These mathematical developments have lead to a greater understanding of the underlying physics that drive the evolution of a nematicon. To gain this understanding, new asymptotic approximation techniques are required, or existing methods extended to capture the new and varying mechanics presented by nonlinear optical beams in NLC. Much of this mathematical work would not have been achieved if it was not for the dedication of various scientists all of whom have aided accurate mathematical descriptions to experimental results.

Nematicons in finite sized NLC cells have been explored experimentally [44] and theoretically in (1+1)D [30]. Chapter 3 presented an extension of the (1+1)D study into (2+1)D, which is a physically more realistic mathematical model. In this case the nematic has a logarithmic response to the presence of the optical beam [45]. The NLC cell boundaries act repulsively towards the nematicon during propagation, and asymptotically a nematicon was found to spiral into the centre of the cell for large propagation distances, matching the experimental predictions [44].

Continuing with the effect the boundaries of the NLC cell have on optical beam propagation, Chapter 4 examined at optical beams with a central phase singularity, known as optical vortex solitary waves, which are experimentally generated using a holographic film containing a phase ramp which winds the optical beam around the phase singularity. Optical vortices are stable in NLC. However, if the phase singularity is disturbed by an interaction with a boundary, this was shown to destroy the optical vortex and result in the formation and propagation of two nematicons. The instability break-up of the optical vortex has been noted in previous experimental results [50, 99] and theoretical results [102].

Chapter 5 examined the propagation of an elliptically-shaped cross-section optical beam and the formation of an elliptic soliton in a finite sized NLC cell. Elliptic solitons are unstable due to the major and minor axis which undergo periodic oscillations and evolve to equal lengths and so a circular nematicon. These different axis lengths result in the immediate diffraction of the optical beam. However, it was found that the nonlocality of the NLC helped to stabilise the elliptic soliton as the nonlocal nematic response to the optical beam resulted in a symmetric medium response. It was shown that the shedding of angular momentum in diffractive radiation was the main driving force for the evolution of the elliptic nematicon.

To explore each of the problems presented in Chapters 3, 4 and 5, equations (2.14) and (2.16) govern the propagation of each of the different optical beam types needed to be derived. In each of the three cases, the same governing equations and boundary conditions could be used to determine the evolution of the solitary waves. Full numerical simulations of the governing equations were run and used to validate the approximations made during the semi-analytical solution process. The important point to note here is that different initial optical beam profiles for the electric field envelope were approximated and used for each of the optical beam types. This was the key to obtaining good comparisons with the full numerical solutions.

The semi-analytical approach was based on an extended variational method first introduced by Kath and Smyth [60] which included a shelf of diffractive radiation that accumulated under an evolving solitary wave. The existence of the radiation shelf was shown using perturbed inverse scattering [60, 73]. This extension required an additional term to be added to the trial function to account for the radiation shelf. A system of modulation equations was derived from an averaged Lagrangian representation of the governing equations, which were then solved using the standard RK4, with radiation loss numerically calculated at each z step. The result was an approximation to the dynamical behaviour of the optical beam.

The governing equations (2.14) and (2.16) were numerically solved using standard second order centred differences for the Laplacian and Jacobi iteration was used to solve the resulting beam system for the director angle. A predictor-corrector method based on second order Runge–Kutta was used to obtain the solution for the electric field envelope of the optical beams. The results found from the approximate equations in each chapter were compared with full numerical solutions. A combination of semi-analytical and full numerical solutions was able to give deep insights into the mechanisms that drove the beam dynamics and evolution. Good agreement was generally found between the approximate solutions and the full numerical solutions. However, the best agreement was achieved by the nematicon solution presented in Chapter 3, as the beam contained features that could be effectively captured by a simple trial function unlike the optical beams in Chapters 4 and 5. Further, when the solutions of the approximate equations did not agree with full numerical solutions, this provided additional insights into the mechanisms that were missing from the model, such as optical beam deformation (Chapter 4) and losses due to angular momentum (Chapter 5).

6.2 Review of methodology

The methodology used throughout this thesis was based on the extended variational method of Kath and Smyth [60], which provides a distinct advantage over the standard variational method [59, 68], as evidenced in Chapter 5. The extended variational method is able to provide a deeper insight into the optical beam dynamics as it included loss to shed radiation. To use the variational method, the full coupled PDE governing equations are required to be approximated, taking limits for the nonlocality and optical beam profile. Within this method, the assumption that the shelf of radiation remains flat within the vicinity of the evolving nematicon is not necessarily true, as can be seen in the tails of the electric field profile in figure 3.1(a). However, if the shelf was able to vary it would over complicate the mathematics, and one would be lost in the mathematical details, rather than investigating the overarching role the shelf plays in the evolution of the optical beam. Also, the approximation of the shelf as it stands works well.

Two equivalent methods were used to solve the director equation (2.16) for the optical beam profiles. These methods were an eigenfunction expansion (Fourier series) and the method of images (MoI). The MoI contained integrals which could not be evaluated exactly, which required an approximation to be made in order to evaluate them. A Dirac delta function approximation of the optical beam's electric field envelope was used and proved a success. Both solutions for the director perturbation were given in terms of an infinite series. However, in the numerical evaluation these series were truncated at the 10200th term. The series solutions were also truncated at the fundamental and first harmonic of the Fourier series, and the eight nearest neighbour images surrounding the point source in the MoI. These approximations of the series illuminated the MoI as an accurate and computationally quick method with little discernible difference between the solution with eight neighbouring images and the 10200 images. Additionally, it compared well with the full numerical solution. In contrast, the fundamental and first harmonic truncation of the Fourier series, resulted in reasonable trajectory comparisons with the full numerical solution, but poor amplitude comparisons.

The chosen trial functions were required to capture the main features of the optical beams, while maintaining simplicity as they propagated within the NLC cell [59], in addition to returning meaningful results for the optical beam's dynamics. The director solutions were dependent upon the accuracy of the trial function as well. The results presented in Chapters 3, 4 and 5, indicated that the trial functions chosen to represent a nematicon, an optical vortex and an elliptic soliton were good choices.

The extended variational method [60] allowed fundamental conclusions to be drawn about the dynamical behaviour of the optical beams during propagation. This is because it allows losses to radiation to be included, allowing the solitary wave to approach the steady state solution. The amplitude oscillations can thus dampen and accurately match those of the full numerical solution [72]. However, for complicated dynamics, such as those presented by the elliptic soliton, mass losses due to radiation alone were not sufficient and another mechanism was sort to improve comparisons with numerical solutions. The elliptic soliton carried an orbital angular momentum, and simulations and experiments [109, 110] highlighted a reshaping of the optical beam due to loss of angular momentum. A term due to angular momentum loss was included in the analysis and shown to be the vital step towards obtaining good comparisons with full numerical solutions. The flexibility of the extended variational method has allowed for losses such as radiation and angular momentum to be incorporated into the solution with ease, while still maintaining the overall simplicity of the original approximate method, in contrast to other variational methods, such as the chirp method.

To summarise, the extended variational method involves two key factors which enable good agreement with full numerical solutions to be obtained. Firstly, the trial function chosen to model the profile of the optical beam's electric field envelope portrays the optical beam parameters, so that good agreement of the parameter oscillations with full numerical solutions can result. The inclusion of the radiation shelf in the trial functions is also important as the shelf evolves with the optical beam, aiding in the agreement with full numerical solutions. Secondly, the inclusion of radiation loss in the modulation solution is vital to allow the solution to evolve to the steady state solution. The effect radiation loss has on the optical beam's propagation is only noticeable at large propagation distances $z \sim O(100)$.

If these two main criteria are met, the extended variational method can be applied to optical beam problems in NLC. Further, this method is applicable to many other optical scenarios where governing equations model a slowly varying electric field with a nonlinear response, such as optical beam propagation in thermal media [118, 119, 120].

6.3 Future research

Throughout this thesis the propagation of different optical beam types (circular, doughnut shaped and elliptical) in finite NLC cells have been analysed. A natural extension of this work is to investigate the behaviour and evolution of two or more interacting beams propagating within a finite NLC cell. Examples of these are optical vortex - optical vortex propagation and nematicon - optical vortex propagation, but this is not an exhaustive list.

The interaction of an optical vortex - optical vortex would have stability complications. An additional complication is that each optical vortex could have a different charge, thus creating new solution scenarios.

Continuing with multiple beam propagation in NLC, the formation of two nematicon waveguides could be used to propagate probing linear optical beams. The problem of interest is the switching of the probe beams between waveguides. To achieve this, a separation distance of the nematicons is required so that attraction and repulsion of the beams is negligible.

The governing equations (2.14) and (2.16) for optical beam propagation in NLC are applicable to other media, such as thermal media [120]. However, the nonlinearity in thermal media is temperature dependent and not a molecular rotation. Therefore, applying different thermal boundary conditions to the medium will allow for the control of the optical beam [120]. The extended variational method has had very little use within thermal media and is an attractive and relatively novel area of research with a large body of unexplored problems.

In summary, the extended variational method used in this thesis has potential application to many other optical beam phenomena and shows promise to make significant contributions to many fields of optics to which it is applied.

Appendix A

List of integrals and alegbraic equations Chapter 2

This appendix contains the list of integrals and alegbraic equations refered to in Chapter 2 [72].

$$A = 2I_2/\sqrt{I_{x32}}, \qquad B = \sqrt{2I_2},$$

where

$$\begin{aligned}
I_2 &= \int_0^\infty x \operatorname{sech}^2 x \, dx = \ln 2, \\
I_{x32} &= \int_0^\infty x^3 \operatorname{sech}^2 x \, dx = 1.352301002\ldots, \\
I_{22} &= \int_0^\infty x \operatorname{sech}^2 x \tanh^2 x \, dx = \frac{1}{3}\ln 2 + \frac{1}{6}, \\
I_1 &= \int_0^\infty x \operatorname{sech} x \, dx = 2C, \\
I_{42} &= \int_0^\infty x \operatorname{sech}^4 x \tanh^2 x \, dx = \frac{2}{15}\ln 2 + \frac{1}{60}, \\
I_4 &= \int_0^\infty x \operatorname{sech}^4 x \, dx = \frac{2}{3}\ln 2 - \frac{1}{6},
\end{aligned}$$

where C is the Catalan constant $C = 0.915965594\ldots$ [75].

The algebraic equations that appear in the shelf radius calculation are given by

$$\begin{aligned}
&\Theta = \frac{2I_{22}D^2\hat{a} - A^2B^2D\hat{\beta}^2\hat{w}^2\hat{a}(2\hat{\alpha} + \Gamma_1\hat{a})}{A^2B^2\hat{\beta}\hat{w}\hat{a}^2(2A^2\hat{\alpha}\hat{\beta}^3 + \Gamma_2 D\hat{\beta}\hat{w} + 2B^2\Gamma_3\hat{\alpha}\hat{w}^3)}, \\
&Q = Q_1 - \frac{I_{22}}{2A^2B^4\hat{\alpha}\hat{\beta}^2\hat{w}^4}[Q_2 + \Theta Q_3], \\
&Q_1 = \frac{I_{22}}{2\hat{w}^2}\left(1 - \frac{2\hat{a}}{\hat{w}}\Theta\right), \qquad Q_2 = \hat{\alpha}^2\hat{\beta}^2\hat{w}^2 + \Gamma_1\hat{\beta}^2\hat{w}^2\hat{a}, \\
&Q_3 = 2\hat{\alpha}\hat{\beta}^2\hat{w}\hat{a} + \Gamma_2\hat{\beta}^2\hat{w}^2\hat{a} + 2\Gamma_3\hat{\alpha}\hat{\beta}\hat{w}^2\hat{a} - 4D^{-1}\hat{\alpha}\hat{\beta}^2\hat{w}^2\hat{a}(A^2\Gamma_3\hat{\beta} + B^2\hat{w}), \\
&\Gamma_1 = \frac{2A^2B^4\hat{w}^4\hat{a}}{qI_4D^2}, \qquad \Gamma_2 = \frac{4A^4B^4\hat{\beta}\hat{w}^3\hat{a}^2(\hat{\beta} - \Gamma_3\hat{w})}{qI_4D^3}, \\
&\Gamma_3 = \frac{B^2\hat{w}(qI_4\hat{\beta}^2 + 4\nu I_3)}{qI_4\hat{\beta}(2A^2\hat{\beta}^2 - B^2\hat{w}^2)}, \qquad D = A^2\hat{\beta}^2 + B^2\hat{w}^2.
\end{aligned}$$

Appendix B

Published papers

In addition to the presentation of research at numerous international conferences, the author of this thesis has also co-authored the following articles

- Minzoni, A.A., Sciberras, L.W., Smyth, N.F., and Worthy, A.L., "Propagation of optical spatial solitary waves in bias-free nematic liquid crystal cells," *Phys. Rev. A*, **84**, 043823 (2011)

  URL: `http://link.aps.org/doi/10.1103/PhysRevA.84.043823`

- Minzoni, A.A., Sciberras, L.W., Smyth, N.F., and Worthy, A.L., "Nonlinear optical beams in bounded nematic liquid crystal cells," *ANZIAM Journal*, **53**, C373–C386 (2011)

  URL: `http://journal.austms.org.au/ojs/index.php/ANZIAMJ/article/view/5076`

- Minzoni, A.A., Sciberras, L.W., Smyth, N.F., and Worthy, A.L., "Vortices in Nematic Liquid Crystals," Nematicons: Spatial Optical Solitons in Nematic Liquid Crystals, ed. G. Assanto, John Wiley and Sons (2012).

- Minzoni, A.A., Sciberras, L.W., Smyth, N.F., and Worthy, A.L., "Optical vortex solitary wave in a bounded nematic-liquid-crystal cell," *Phys. Rev. A*, **87**, 013810 (2013)

  URL: `http://link.aps.org/doi/10.1103/PhysRevA.87.013810`

Bibliography

[1] J. Scott Russell, "Report on waves," *Fourteenth meeting of the British Association for the Advancement of Science*, 1844.

[2] N. Zabusky and M. Kruskal, "Interaction of "solitons" in collisionless plasma and the recurrence of initial states," *Phys. Rev. Lett.*, vol. 15, pp. 240–243, 1965.

[3] L. Rayleigh, "On waves," *Phil. Mag. ser. 5*, vol. 1, pp. 257–279, 1876.

[4] D. Korteweg and G. de Vries, "On the change of form of long waves advancing in a rectangular canal and on a new type of long stationary waves," *Phil. Mag.*, vol. 39, pp. 422–443, 1895.

[5] E. Fermi, J. Pasta, and S. Ulam, "Studies of nonlinear problems: Document la-1940," *Los Alamos Scientific Laboratory*, 1955.

[6] C. Gardner, J. Greene, M. Kruskal, and R. Miura, "Method for solving the Korteweg-deVries equation," *Phys. Rev. Lett.*, vol. 19, pp. 1095–1097, 1967.

[7] A. Newell, *Solitons in mathematics and physics.* Society for Industrial and Applied Mathematics (SIAM), 1985.

[8] R. Miura, "Korteweg-de vries equation and generalisations. i. a remarkable explicit nonlinear transform," *J. Math. Phys.*, vol. 9, pp. 1202–1204, 1968.

[9] P. Franken, A. Hill, C. Peters, and G. Weinreich, "Generation of optical harmonics," *Phys. Rev. Lett.*, vol. 7, pp. 118–119, 1961.

[10] A. Hasegawa and F. Tappert, "Transmission of stationary nonlinear optical physics in dispersive dielectric fibers. I. anomalous dispersion," *Appl. Phys. Lett.*, vol. 23, pp. 142–144, 1973.

[11] A. Hasegawa and F. Tappert, "Transmission of stationary nonlinear optical physics in dispersive dielectric fibers. II. normal dispersion," *Appl. Phys. Lett.*, vol. 23, pp. 171–172, 1973.

[12] L. Mollenauer, R. Stolen, and J. Gordon, "Experimental observation of picosecond pulse narrowing and solitons in optical fibers," *Phys. Rev. Lett.*, vol. 45, pp. 1095–1098, 1980.

[13] M. Segev, "Optical spatial solitons," *Opt. & Quantum Electron.*, vol. 30, pp. 503–533, 1998.

[14] J. Beeckman, K. Neyts, X. Hutsebaut, C. Cambournac, and M. Haelterman, "Time dependence of soliton formation in planar cells of ne-

matic liquid crystals," *IEEE J. Quantum Electron.*, vol. 41, pp. 735–740, 2005.

[15] C. Rotschild, O. Cohen, O. Manela, M. Segev, and T. Carmon, "Solitons in nonlinear media with an infinite range of nonlocality: first observation of coherent elliptic solitons and of vortex-ring solitons," *Phys. Rev. Lett.*, vol. 95, p. 213904, 2005.

[16] C. Rotschild, B. Alfassi, O. Cohen, and M. Segev, "Long-range interactions between optical solitons," *Nat. Phys.*, vol. 2, pp. 769–774, 2006.

[17] A. Dreischuh, D. Neshev, D. Peterson, O. Bang, and W. Królikowski, "Observation of attraction between dark solitons," *Phys. Rev. Lett.*, vol. 96, p. 043901, 2006.

[18] D. Suter and T. Blasberg, "Stabilization of transverse solitary waves by a nonlocal response of the nonlinear medium," *Phys. Rev. A*, vol. 48, pp. 4583–4587, 1993.

[19] M. Segev, B. Crosignani, A. Yariv, and B. Fisher, "Spatial solitons in photorefractive media," *Phys. Rev. Lett.*, vol. 68, pp. 923–926, 1992.

[20] W. Królikowski, M. Saffman, B. Luther-Davies, and C. Denz, "Anomalous interaction of spatial solitons in photorefractive media," *Phys. Rev. Lett.*, vol. 80, pp. 3240–3243, 1998.

[21] A. Parola, L. Salasnich, and L. Reatto, "Structure and stability of bosonic clouds: Alkali-metal atoms with negative scattering length," *Phys. Rev. A*, vol. 57, pp. R3180–R3183, 1998.

[22] A. Griesmaier, J. Werner, S. Hensler, J. Stuhler, and T. Pfau, "Bose-einstein condensation of chromium," *Phys. Rev. Lett.*, vol. 94, p. 160401, 2005.

[23] I. Khoo, *Liquid Crystals: Physical Properties and Nonlinear Optical Phenomena*. Wiley, 2 ed., 1995.

[24] I. Khoo, "Nonlinear optics of liquid crystalline materials," *Phys. Rep.*, vol. 471, pp. 221–267, 2009.

[25] M. Peccianti and G. Assanto, "Nematicons," *Phys. Reports*, vol. 516, pp. 147–208, 2012.

[26] G. Assanto, A. Minzoni, M. Peccianti, and N. Smyth, "Optical solitary waves escaping a wide trapping potential in nematic liquid crystals: modulation theory," *Phys. Rev. A*, vol. 79, p. 033837, 2009.

[27] M. Karpierz, "Solitary waves in liquid crystalline waveguides," *Phys. Rev. E*, vol. 66, p. 0336603, 2002.

[28] D. McLaughlin, D. Muraki, and M. Shelley, "Self-focussed optical structures in a nematic liquid crystal," *Physica D*, vol. 97, no. 4, pp. 471–497, 1996.

[29] G. Assanto, M. Peccianti, and C. Conti, “Nematicons: Optical spatial solitons in nematic liquid crystals,” *Optics & Photonics News*, vol. 14, pp. 44–48, 2003.

[30] A. Alberucci, G. Assanto, D. Buccoliero, A. Desyatnikov, T. Marchant, and N. Smyth, “Modulation analysis of boundary-induced motion of optical solitary waves in a nematic liquid crystal,” *Phys. Rev. A*, vol. 79, p. 043816, 2009.

[31] E. Braun, L. Faucheux, and A. Libchaber, “Strong self-focusing in nematic liquid crystals,” *Phys. Rev. A*, vol. 48, pp. 611–622, 1993.

[32] M. Warenghem, J. Henninot, and G. Abbate, “Nonlinearly induced self waveguiding structure in dye doped nematic liquid crystals confined in capillaries,” *Opt. Express*, vol. 2, pp. 483–490, 1998.

[33] M. Peccianti, K. Brzdakiewicz, and G. Assanto, “Nonlocal spatial soliton interactions in nematic liquid crystals,” *Opt. Lett.*, vol. 27, pp. 1460–1462, 2002.

[34] M. Peccianti and G. Assanto, “Nemactic liquid crystal: A suitable medium for self-confinement of coherent and incoherent light,” *Phys. Rev. E*, vol. 65, p. 035603(R), 2002.

[35] M. Peccianti, A. De Rossi, G. Assanto, A. De Luca, C. Umeton, and I. Khoo, “Electrically assisted self-confinement and waveguiding in

planar nematic liquid crystal cells," *App. Phys. Lett.*, vol. 91, pp. 7–9, 2000.

[36] C. Conti, M. Peccianti, and G. Assanto, "Route to nonlocality and observation of accessible solitons," *Phys. Rev. Lett.*, vol. 91, p. 073901, 2003.

[37] M. Peccianti and G. Assanto, "Signal readdressing by steering of spatial solitons in bulk nematic liquid crystals," *Opt. Lett.*, vol. 26, pp. 1690–1692, 2001.

[38] G. Assanto, M. Peccianti, K. Brzdkiewicz, A. De Luca, and U. C., "Nonlinear wave propagation and spatial solitons in nematic liquid crystals," *J. Nonl. Opt. Phys. Mat.*, vol. 12, pp. 123–134, 2003.

[39] G. Whitham, *Linear and Nonlinear Waves.* J. Wiley and Sons, 2 ed., 1974.

[40] M. Peccianti, A. Fratalocchi, and G. Assanto, "Transverse dynamics of nematicons," *Opt. Express*, vol. 12, pp. 6524–6529, 2004.

[41] E. b. G. Assanto, *Nematicons; spatial optical solitons in nematic liquid crystals.* John Wiley and Sons, 1 ed., 2013.

[42] B. Skuse and N. Smyth, "Interaction of two-color solitary waves in a liquid crystal in the nonlocal regime," *Phys. Rev. A*, vol. 79, p. 063806, 2009.

[43] A. Alberucci, M. Peccianti, and G. Assanto, "Nonlinear bouncing of nonlocal spatial solitons at boundaries," *Opt. Lett.*, vol. 32, pp. 2795–2797, 2007.

[44] A. Alberucci and G. Assanto, "Propagation of optical spatial solitons in finite-size media: interplay between nonlocality and boundary conditions," *J. Opt. Soc. Amer. B*, vol. 24, pp. 2314–2320, 2007.

[45] A. Minzoni, L. Sciberras, N. Smyth, and A. Worthy, "Propagation of optical spatial solitary waves in bias-free nematic-liquid-crystal cells," *Phys. Rev. A*, vol. 84, p. 043823, 2011.

[46] A. Minzoni, L. Sciberras, S. N.F., W. A.L., and e. G. Assanto, "Vortices in nematic liquid crystals, appearing in nematicons: Spatial optical solitons in nematic liquid crystals," *John Wiley and Sons*, pp. 361–390, 2012.

[47] Y. Izdebskaya, A. Desyatnikov, G. Assanto, and Y. Kivshar, "Dipole azimuthons and vortex charge flipping in nematic liquid crystals," *Optics Express*, vol. 19, p. 21457, 2011.

[48] Y. Izdebskaya, J. Rebling, A. Desyatnikov, and K. Y.S., "Observation of vector solitons with hidden vorticity," *Opt. Lett.*, vol. 37, pp. 767–769, 2012.

[49] M. Shen, J. Zheng, Q. Kong, Y. Lin, C. Jeng, R. Lee, and W. Królikowski, "Stabilization of counter-rotating vortex pairs in nonlocal media," *Phys. Rev. A*, vol. 86, p. 013827, 2012.

[50] Y. Kivshar and G. Agrawal, *Optical Solitons: From Fibers to Photonic Crystals.* Academic Press, 1 ed., 2003.

[51] F. Lenzini, S. Residori, F. Arecchi, and U. Bortolozzo, "Optical vortex interaction and generation via nonlinear wave mixing," *Phys. Rev. A*, vol. 84, p. 061801(R), 2011.

[52] A. Yakimenko, Y. Zaliznyak, and Y. Kivshar, "Stable vortex solitons in nonlocal self-focusing nonlinear media," *Phys. Rev. E*, vol. 71, p. 065603(R), 2005.

[53] A. Minzoni, N. Smyth, A. Worthy, and Y. Kivshar, "Stabilization of vortex solitons in nonlocal nonlinear media," *Phys. Rev. A*, vol. 76, p. 063803, 2007.

[54] G. Capparrone, R. Hernandez, and C. Provenzano, "Magnus force effect in optical manipulation," *Phys. Rev. A*, vol. 84, p. 015802, 2011.

[55] B. Black and S. Mohanty, "Fiber-optic spanner," *Opt. Lett.*, vol. 37, pp. 5030–5032, 2012.

[56] D. Grier, "A revolution in optical manipulation," *Nature*, vol. 424, pp. 21–27, 2003.

[57] N. Tabyrian, A. Sukhov, and B. Zel'dovich, "Orientational optical nonlinearity of liquid crystals," *Mol. Cryst. & Liq. Cryst.*, vol. 136, pp. 1–139, 1986.

[58] C. Weilnau, M. Ahles, J. Petter, D. Träger, J. Schöder, and C. Denz, "Spatial optical $(2 + 1)$-dimensional scalar- and vector solitons in saturable nonlinear media," *Ann. Phys.*, vol. 11, pp. 573–629, 2002.

[59] B. Malomed, "Variational methods in nonlinear fiber optics and related fields," *Prog. Opt.*, vol. 43, pp. 71–193, 2002.

[60] W. Kath and N. Smyth, "Soliton evolution and radiation loss for the nonlinear schrödinger equation," *Phys. Rev. E*, vol. 51, pp. 1484–1492, 1995.

[61] M. Peccianti, C. Conti, G. Assanto, A. De Luca, and C. Umeton, "Routing of anisotropic spatial solitons and modulation instability in liquid crystals," *Nature*, vol. 432, pp. 733–737, 2004.

[62] C. Conti, M. Peccianti, and G. Assanto, "Observation of optical spatial solitons in a highly nonlocal medium," *Phys. Rev. Lett.*, vol. 92, p. 113902, 2004.

[63] Y. Karamzin and A. Sukhorukov, "Mutual focusing of high-power light beams in media with quadratic nonlinearity," *Sov Phys. JETP*, vol. 41, p. 414, 1975.

[64] E. Kuznetsov and A. Rubenchik, "Soliton stability in plasmas and hydrodynamics," *Physics Reports*, vol. 142, pp. 103–165, 1986.

[65] C. Rotschild, M. Segev, Z. Xu, Y. Kartashov, L. Torner, and O. Cohen, "Two-dimensional multipole solitons in nonlocal nonlinear media," *Opt. Lett.*, vol. 31, pp. 3312–3314, 2006.

[66] W. Wan, S. Jia, and J. Fleischer, "Dispersive superfluid-like shock waves in nonlinear optics," *Nature Physics*, vol. 3, no. 1, pp. 46–51, 2007.

[67] W. Wan, D. Dylov, C. Barsi, and J. Fleischer, "Dispersive shock waves with negative pressure," *OSA/CLEO/QELS*, vol. 1-5, pp. 2910–2911, 2009.

[68] D. Anderson, "Variational approach to nonlinear pulse propagation in optical fibers," *Phys. Rev. A*, vol. 27, pp. 3135–3145, 1983.

[69] V. Lashkin, A. Desyatnikov, E. Ostrovskaya, and Y. Kivshar, "Azimuthal vortex clusters in bose-einstein condensates," *Phys. Rev. A*, vol. 85, pp. 013620–6, 2012.

[70] I. Gelfand and S. Fomin, *Calculus of variations.* Prentice-Hall: Englewood Cliffs, N.J., rev. english ed ed., 1963.

[71] N. Smyth and W. Kath, “Radiative losses due to pulse interactions in birefringent nonlinear optical fibers,” *Phys. Rev. E*, vol. 63, p. 036614, 2001.

[72] A. Minzoni, N. Smyth, and A. Worthy, “Modulation solutions for nematicon propagation in nonlocal liquid crystals,” *J. Opt. Soc. Amer. B*, vol. 24, pp. 1549–1556, 2007.

[73] J. Yang, “Vector solitons and their internal oscillations in birefringent nonlinear optical fibers,” *Stud. Appl. Math.*, vol. 98, pp. 61–97, 1997.

[74] C. García Reimbert, A. Minzoni, and N. Smyth, “Spatial soliton evolution in nematic liquid crystals in the nonlinear local regime,” *J. Opt. Soc. Amer. B*, vol. 23, pp. 294–301, 2006.

[75] M. Abramowitz and I. Stegun, *Handbook of Mathematical Functions with Formulas, Graphs, and Mathematical Tables.* Dover, 10 ed., 1972.

[76] L. Atkinson, P. Harley, and J. Hudson, *Numerical methods with Fortran 77: A practical introduction.* Longman Group, 1 ed., 1989.

[77] M. Miksis and L. Ting, “A numerical method for long time solutions of integrodifferential systems in multiphase flow,” *Comput. Fluids*, vol. 16, pp. 327–340, 1988.

[78] B. Fornberg and G. Whitham, “A numerical and theoretical study of certain nonlinear wave phenomena,” *Phil. Trans. R. Soc. Lond. A*, vol. 289, pp. 373–403, 1978.

[79] G. Assanto, A. Fratalocchi, and M. Peccianti, “Spatial solitons in nematic liquid crystals: from bulk to discrete,” *Opt. Express*, vol. 15, pp. 5248–5259, 2007.

[80] M. Peccianti, A. Pasquazi, G. Assanto, and R. Morandotti, “Enhancement of third-harmonic generation in nonlocal spatial solitons,” *Opt. Lett.*, vol. 35, pp. 3342–3344, 2010.

[81] O. Bang, W. Królikowski, J. Wyller, and J. Rasmussen, “Collapse arrest and soliton stabilization in nonlocal nonlinear media,” *Phys. Rev. E*, vol. 66, p. 046619, 2002.

[82] P. Rasmussen, O. Bang, and W. Królikowski, “Theory of nonlocal soliton interaction in nematic liquid crystals,” *Phys. Rev. E*, vol. 72, p. 066611, 2005.

[83] C. García Reimbert, A. Minzoni, T. Marchant, N. Smyth, and A. Worthy, “Dipole soliton formation in a nematic liquid crystal in the nonlocal limit,” *Physica D*, vol. 237, pp. 1088–1102, 2008.

[84] B. Skuse and N. Smyth, “Two-colour vector soliton interactions in nematic liquid crystals in the local response regime,” *Phys. Rev. A*,

vol. 77, p. 013817, 2008.

[85] G. Assanto, B. Skuse, and N. Smyth, "Optical path control of spatial optical solitary waves in dye-doped nematic liquid crystals," *Photon. Lett. Poland*, vol. 1, pp. 154–156, 2009.

[86] G. Assanto, B. Skuse, and N. Smyth, "Solitary wave propagation and steering through light-induced refractive potentials," *Phys. Rev. A*, vol. 81, p. 063811, 2010.

[87] G. Assanto, A. Minzoni, N. Smyth, and A. Worthy, "Refraction of nonlinear beams by localised refractive index changes in nematic liquid crystals," *Phys. Rev. A*, vol. 82, p. 053843, 2010.

[88] A. Minzoni, N. Smyth, and Z. Xu, "Stability of an optical vortex in a circular nematic cell," *Phys. Rev. A*, vol. 81, p. 033816, 2010.

[89] A. Snyder and M. Mitchell, "Accessible solitons," *Science*, vol. 276, pp. 1538–1541, 1997.

[90] D. Pelinovsky and Y. Yang, "Internal oscillations and radiation damping of vector solitons," *Stud. Appl. Math.*, vol. 105, pp. 245–276, 2000.

[91] M. Ablowitz, S. Dixon, T. Horikis, and D. Frantzeskakis, "Perturbations of dark solitons," *Proc. R. Soc. Lond. A*, vol. 467, p. 2597, 2011.

[92] R. Courant and D. Hilbert, *Methods of Mathematical Physics*, vol. 1. Interscience Publishers, 1 ed., 1965.

[93] A. Alberucci, A. Piccardi, M. Peccianti, M. Kaczmarek, and G. Assanto, “Propagation of spatial optical solitons in a dielectric with adjustable nonlinearity,” *Phys. Rev. A*, vol. 82, p. 023806, 2010.

[94] N. Nikolov, D. Neshev, O. Bang, and W. Królikowski, “Quadratic solitons as nonlocal solitons,” *Phys. Rev. E*, vol. 68, p. 036614, 2003.

[95] B. Alfassi, C. Rotschild, O. Manela, M. Segev, and D. Christodoulides, “Boundary force effects extracted on solitons in nonlinear media with a very large range of nonlocality,” *Opt. Lett.*, vol. 32, pp. 154–156, 2007.

[96] J. Nye and M. Berry, “Dislocations in wave trains,” *Proc. R. Soc. Lond. A*, vol. 336, pp. 165–190, 1974.

[97] D. Neshev, T. Alexander, E. Ostrovskaya, Y. Kivshar, H. Martin, I. Makasyuk, and Z. Chen, “Observation of discrete vortex solitons in optically induced photonic lattices,” *Phys. Rev. Lett.*, vol. 92, p. 123903, 2004.

[98] J. Fleischer, G. Bartal, O. Cohen, O. Manela, M. Segev, J. Hudock, and D. Christodoulides, “Observation of vortex-ring ‘discrete’ solitons in 2d photonic lattices,” *Phys. Rev. Lett.*, vol. 92, p. 123904, 2004.

[99] V. Tikhonenko, J. Christou, and B. Luther-Daves, “Spiraling bright spatial solitons formed by the breakup of an optical vortex in a sat-

urable self-focusing medium," *J. Opt. Soc. Am. B*, vol. 12, pp. 2046–2052, 1995.

[100] I. Basistiy, V. Bazhenov, M. Soskin, and M. Vasnetsov, "Optics of light beams with screw dislocations," *Opt. Comm.*, vol. 103, pp. 422–428, 1993.

[101] T. Alexander, E. Ostrovskaya, Y. Kivshar, and P. Julienne, "Vortices in atomic-molecular bose-einstein condensates," *J. Opt. B: Quantum Semiclass. Opt.*, vol. 4, pp. S33–S38, 2002.

[102] N. Smyth and W. Xia, "Refraction and instability of optical vortices at an interface in a liquid crystal," *J. Phys. B: At. Mol. Opt. Phys.*, vol. 45, p. 165403, 2012.

[103] M. Padgett, J. Courtial, L. Allen, S. Franke-Arnold, and S. Barnett, "Entanglement of orbital angular momentum for the signal and idler beams in parametric down-conversion," *Journal of Modern Optics*, vol. 49, pp. 777–785, 2002.

[104] I. Khoo, "Theory of optically induced molecular reorientations and quantitative experiments on wave mixing and the self-focusing of light," *Phys. Rev. A*, vol. 25, pp. 1636–1644, 1982.

[105] G. Assanto, A. Minzoni, N. Smyth, and A. Worthy, "Refraction of nonlinear beams by localised refractive index changes in nematic liquid

crystals," *Phys. Rev. A*, vol. 82, p. 053843, 2010.

[106] G. Assanto, N. Smyth, and W. Xia, "Modulation analysis of nonlinear beam refraction at an interface in liquid crystals," *Phys. Rev. A*, vol. 84, p. 033818, 2011.

[107] J. Yang, "Stability of vortex solitons in a photorefractive optical lattice," *New J. Phys.*, vol. 6, p. 47, 2004.

[108] G. Assanto, C. García-Reimbert, A. Minzoni, N. Smyth, and A. Worthy, "Lagrange solution for three wavelength solitary wave clusters in nematic liquid crystals," *Physica D*, vol. 240, pp. 1213–1219, 2011.

[109] E. Eugenieva, D. Christodoulides, and M. Segev, "Elliptic incoherent solitons in saturable nonlinear media," *Opt. Lett.*, vol. 25, pp. 972–974, 2000.

[110] O. Katz, T. Cannon, T. Schwartz, M. Segev, and D. Christodoulides, "Observation of elliptic incoherent spatial solitons," *Opt. Lett.*, vol. 29, pp. 1248 – 1250, 2004.

[111] A. Desyatnikov, D. Buccoliero, M. Dennis, and Y. Kivshar, "Suppression of collapse for spiraling elliptic solitons," *Phys. Rev. Lett.*, vol. 104, p. 053902, 2010.

[112] O. Bang, W. Królikowski, J. Wyller, and J. Rasmussen, “Collapse arrest and soliton stabilization in nonlocal nonlinear media,” *Phys. Rev. E*, vol. 66, p. 046619, 2002.

[113] B. Crosignani and P. Di Porta, “Nonlinear propagation in kerr media of beams with unequal transverse widths,” *Opt. Lett.*, vol. 18, pp. 1394–1396, 1993.

[114] A. Barthelemy, C. Froehly, S. Maneuf, and E. Reynaud, “Experimental observation of beams’ self-deflection appearing with two-dimensional spatial soliton propagation in bulk kerr material,” *Opt. Lett.*, vol. 17, pp. 844–846, 1992.

[115] L. Marrucci, F. Vetrano, and E. Santamato, “Optical reorientation in nematic liquid crystals controlled by the laser beam shape,” *Opt. Comm.*, vol. 171, pp. 131–136, 1999.

[116] A. Minzoni, L. Sciberras, N. Smyth, and A. Worthy, “Optical vortex solitary wave in a bounded nematic-liquid-crystal cell,” *Phys. Rev. A*, vol. 87, p. 013810, 2013.

[117] A. Minzoni, N. Smyth, and A. Worthy, “Pulse evolution for a two dimensional sine-gordon equation,” *Physica D*, vol. 159, pp. 101–123, 2001.

[118] A. Litvak, "Self focusing of powerful light beams by thermal effects," *JETP Lett.*, vol. 4, pp. 230–233, 1966.

[119] F. Dabby and J. Whinnery, "Thermal self focusing of laser beams in lead glasses," *App. Phys. Lett.*, vol. 13, pp. 284–286, 1968.

[120] S. Louis, T. Marchant, and N. Smyth, "Optical solitary waves in thermal media with nonsymmetric boundary conditions," *J. Phys. A. Math. Ther.*, vol. 46, p. 055201, 2013.